Aalto University
School of Engineering

Joonas Forsman

Numerical Studies of Residual Stress Patterns and Their Effects on Circular Truss Members with Flattened Ends

Thesis submitted for examination for the degree of
Master of Science in Technology.

Espoo 29.05.2017
Thesis supervisor: Professor Jari Puttonen
Thesis instructors: Dr. Wei Lu, D.Sc. (Tech)
Mr. Mauro Nottegar, M.Sc. (Tech)

Aalto-yliopisto
Insinööritieteiden
korkeakoulu

Aalto-yliopisto, PL 11000, 00076 AALTO
www.aalto.fi
Diplomityön tiivistelmä

Tekijä Joonas Forsman

Työn nimi Numeerinen tutkimus jäännösjännitysjakaumista sekä niiden vaikutuksista pyöreisiin päistään litistettyihin ristikkosauvoihin

Koulutusohjelma Rakenne- ja rakennustuotantotekniikka

Pää-/sivuaine Rakennetekniikka **Koodi** RAK.thes

Työn valvoja Prof. Jari Puttonen

Työn ohjaaja(t) TkT Wei Lu, DI Mauro Nottegar

Päivämäärä 29.05.2017 **Sivumäärä** 114 **Kieli** englanti

Tiivistelmä

Eurokoodin mukaisessa terässauvojen nurjahdustarkastelussa valmistusprosessista aiheutuvat epätarkkuudet ja jäännösjännitykset huomioidaan asiaankuuluvalla epätarkkuustekijällä. Mitoitusohjeet ovat voimassa ainoastaan, kun sauvan poikkileikkaus säilyy muuttumattomana pituussuuntaisen akselin suhteen, joten päistään litistettyjen sauvojen tapauksessa eurokoodin mukainen nurjahdustarkastelu ei ole mahdollinen. Sauvan rakenteellinen kapasiteetti voidaan määrittää soveltamalla edistyneitä analyysimenetelmiä, jotka huomioivat valmistuksesta aiheutuvat jäännösjännitykset ja deformoituneen geometrian alkutilana analyysissä.

Tässä diplomityössä tutkitaan numeerisesti jäännösjännitysjakaumia sekä niiden vaikutusta päistään litistetyn sauvan rakenteelliseen kestävyyteen. Työssä esitellään soveltuvia laskennallisia menetelmiä rakenteen alkutilan mallintamiseen. Esitellyt menetelmät validoidaan kirjallisuudesta löytyvällä kokeellisella tutkimusaineistolla. Kolmiosainen numeerinen analyysi koostuu putken litistyssimulaatiosta, kimmoisen palauman ja puristuskestävyyden määrityksestä ja se tehdään Abaqus-elementtimenetelmäohjelmistolla. Lopuksi numeerisesta analyysistä saadut jännitysjakaumat esitetään sekä putken litistysvaiheessa että lopputilassa.

Esitetyillä analyysimenetelmillä saatu puristuskestävyyden arvo oli 1,85% pienempi kuin kokeellisesti määritetty arvo. Numeerinen malli kuvasi aksiaalisen jäykkyyden suurempana kuin koetilanteessa osoittautui olevan. Putken transitioalueen jäännösjännitykset paransivat rakenteen kuormankantokykyä 5,8%. Numeerisesti mallinnettuja jäännösjännitysjakaumia voidaan pitää hyvänä arviona rakenteen alkutilasta, mutta lisätarkasteluja dynaamisten analyysien suhteen tarvitaan. Työn tuloksena voidaan muodostaa parempi käsitys päistään litistetyn sauvan alkutilasta ja käyttäytymisestä.

Avainsanat Abaqus, eksplisiittinen, FEM, elementtimenetelmä, päistään litistetty sauva, kylmämuovaus, simulaatio, jäännösjännitykset

Aalto University
School of Engineering

Aalto University, P.O. BOX 11000, 00076 AALTO
www.aalto.fi

Abstract of master's thesis

Author Joonas Forsman

Title of thesis Numerical Studies of Residual Stress Patterns and Their Effects on Circular Truss Members with Flattened Ends

Degree programme Structural Engineering and Building Technology

Major/minor Structural Engineering **Code** RAK.thes

Thesis supervisor Prof. Jari Puttonen

Thesis advisor(s) Dr. Wei Lu, D.Sc. (Tech) and Mr. Mauro Nottegar, M.Sc. (Tech)

Date 29.05.2017 **Number of pages** 114 **Language** English

Abstract

When a steel member verification against buckling is carried out according to the Eurocode 3, the residual stresses and geometric tolerances resulting from the manufacturing process are taken into account with an imperfection factor. However, the application rules in Eurocode 3 may only be used when cross-sectional shape of the profile is not modified along the longitudinal axis. When the member end is flattened, Eurocode 3 provides no guidelines to estimate the initial conditions in the member and eventually no design equations for determining the connection resistance. In such cases, advanced analysis techniques based on non-conservative approaches are needed for evaluating the structural performance.

In this thesis, a numerical study of residual stress patterns and their effects on circular truss member with flattened ends is conducted. The thesis introduces suitable finite element techniques for modelling the initial stress patterns induced during manufacturing. The proposed techniques are validated with experimental results found in the literature. The three-part sequential analysis is made using Abaqus finite element software consisting of the forming simulation, the springback analysis and the analysis under compressive loading. Finally, stress patterns from the numerical analysis are derived both in the flattening and the final stage.

The proposed simulation techniques showed excellent correlation in maximum structural bearing capacity; the maximum compressive resistance being 1.85% lower compared to the experimental data. The results also indicated that the numerical model was stiffer in the axial direction than the structure tested. The tensile residuals stresses within the transition zone improved the compressive resistance by 5.8%. The obtained residual stress patterns can be considered a good estimation of the initial material state, but for dynamic analyses further considerations are needed. As result, a better understanding for structural behaviour of a member with flattened ends is formed.

Keywords Abaqus, explicit, FEM, finite element method, flattened end type member, metal forming simulation, residual stresses

Acknowledgements

This master's thesis was done in Sweco Structures Ltd to improve the knowledge on behavior of the flattened end connections and analysis techniques for advanced structural analyses. I am most grateful for the financial support provided and the great opportunity to improve and deepen my skills on advanced numerical analysis techniques.

First of all, I would like to than my thesis instructors Dr. Wei Lu and Mr. Mauro Nottegar for their patient guidance throughout the process. The valuable advice on steel structures and finite element analyses have been extremely helpful. Special thanks go to the thesis supervisor Professor Jari Puttonen for his understanding, patience and invaluable comments.

I would like to thank my family and my friends for their support and encouragement throughout my study. I would like to express my gratitude to the members of the WhatsApp-groups "LapinlahtiSpedet" and "Maanjäristys" for sparring and peer-support. Finally, and most importantly, I would like to thank my girlfriend Aino, whose support, understanding and irreplaceable heartiness were undeniably the main reasons making this thesis a reality.

Espoo 29.5.2017

Joonas Forsman

Table of Contents

Table of Contents ..... **i**

1 Introduction **1**

1.1 Background 1

1.2 Tube Flattening as a Manufacturing Method 3

1.3 Metallurgical Aspects 4

1.3.1 Residual Stresses 4

1.3.2 Strength Enhancements 5

1.4 Design Code Considerations 7

1.5 Research on Flattened End Members 8

1.6 Scope and Outlines of the Thesis 11

2 Considerations in Metal Forming Simulations **13**

2.1 Discretization of a Boundary Value Problem 13

2.1.1 Lagrangian Method 13

2.1.2 Eulerian Method 14

2.1.3 ALE-method 14

2.2 Element Formulation 15

2.2.1 Element Types 15

2.2.2 Element Instabilities 16

2.2.3 Element Type Selection 17

2.3 Material Modeling 18

2.3.1 Uniaxial Elasto-plastic Material 18

2.3.2 Hardening Laws 19

2.3.3 Material Modeling in Structural Applications 20

2.4 Time Integration Method 21

2.4.1 Iterative Implicit Time Integration 22

2.4.2 Direct Explicit Time Integration 22

2.4.3 Selection of the Time Integration Method 25

2.5 Quasi-Static Response 26

2.5.1 Loading Rates 27

2.5.2 Mass Scaling 27

2.5.3 Energy Balance 27

3 Numerical Analysis of Model Used for Validation 28
3.1 Analysis Path for Tube Flattening Simulation 30
3.2 Part I - Forming Simulation 32
3.2.1 Input Geometry 32
3.2.2 Material Model 33
3.2.3 FE-modelling 35
3.2.4 Time Integration 37
3.2.5 Contact Modeling 37
3.2.6 Analysis Conditions 37
3.2.7 Analysis Parameter Study 39
3.2.8 Time period study 39
3.2.9 Results of Part I 47
3.2.10 Remarks on Part I 54
3.3 Part II – Springback 55
3.3.1 Redefined Parameters for Part II 55
3.3.2 Results of Part II 56
3.3.3 Remarks on Part II 64
3.4 Part III – Compressive Loading 65
3.4.1 Redefined Parameters for Part III 65
3.4.2 Results of Part III 67
3.4.3 Remarks on Part III 77
4 Numerical Studies of Stress and Strain Patterns in the Vicinity of Flattened End in Various Stages 79
4.1 Flattening Stage 81
4.1.1 Forming Stresses in the Circumferential Direction 82
4.1.2 Total Strains in the Circumferential Direction 83
4.1.3 Forming Stresses in the Longitudinal Direction 85
4.1.4 Total Strains in the Longitudinal Direction 87
4.2 Springback Stage 88
4.2.1 Stress States and Plastic Strains in the Circumferential Direction 89
4.2.2 Stress States and Plastic Strains in the Longitudinal Direction 91
5 Residual Stress Distributions and Their Effects on the Behavior of a Compressed Member 94
5.1 Circumferential Direction 94

5.2 Longitudinal Direction 95
5.3 Further Evaluations on the Longitudinal Residual Stresses 97
5.3.1 Section O-O 97
5.3.2 Section A-A 98
5.3.3 Section B-B 99
5.3.4 Section C-C 101
5.3.5 Section D-D 103
5.4 Effects on the Behavior of a Compressed Member 106
6 Conclusions 111
References 113

1 Introduction

1.1 Background

Lattice and space frame systems made from structural hollow sections allow the use of long spans and complex roof shapes. However, especially in large space trusses where several truss members are connected to one node, the connections usually end up to be complicated systems leading to high manufacturing costs.

In welded assemblies, the ends of a circular bracing member require expensive and complex cutting including welding preparation bevels. In order to eliminate overlapping in the joint, large eccentricity is often needed at the end nodes of connection members. A typical multiplanar joint with overlapping bracing members is presented in Figure 1-1.

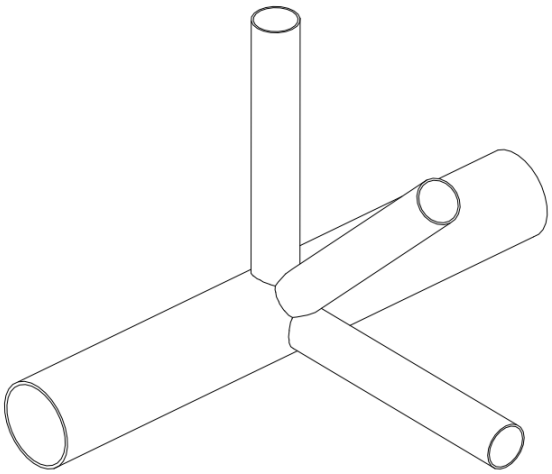

Figure 1-1 Typical multiplanar joint in a space truss.

Use of flattened end-type connection in the tubular steel trusses offers advantages such as improved static performance of the truss system and decreased costs due to a simpler manufacturing process. The flattened-end type connection is made by flattening the member end at the workshop resulting a section that does not need any complex cutting or preparation when welded to a truss chord. The principle of a multiplanar joint with flattened ends is presented in Figure 1-2.

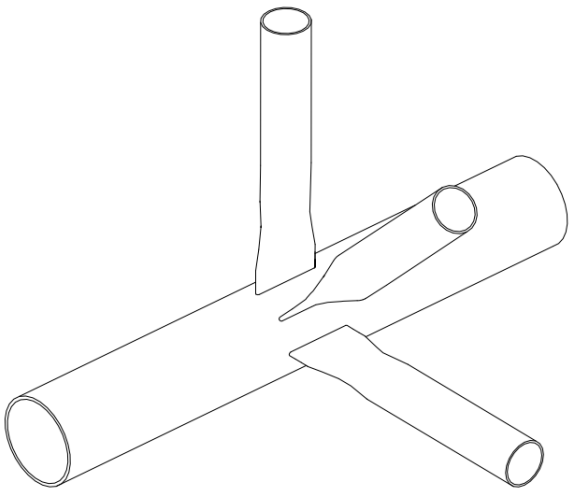

Figure 1-2 Space truss joint with flattened ends.

In case of bolted connections, the most common solution for bolting bracing members into chords is to use a gusset plate (Figure 1-3). The connection plates are first welded into the bracing members to enable the bolted connection. Next cover plates are welded to the ends to make the assembly waterproof. As the member is axially loaded, the force is transmitted to the chord via the welds of the connection plate, the connection plate, the bolts and the gusset plate and its welds.

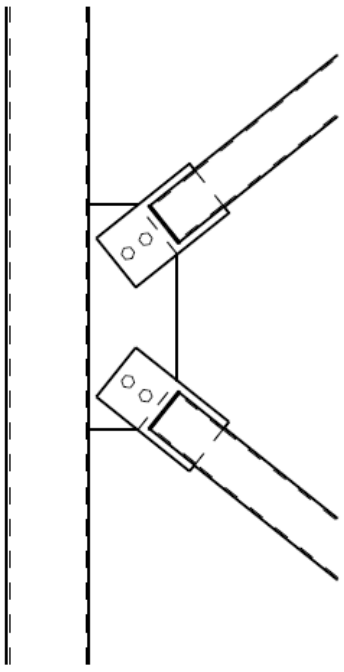

Figure 1-3 Typical bolted tubular joint with a gusset plate.

When designing a tube gusset connection, all the possible failure modes of the connection shall first be identified. Next the connection parameters have to be defined so that the weakest component in the connection is exhibiting ductile behavior. Even though the connection is reliable and rather easy to design to be ductile, plates and welds are needed in the manufacturing the connection of a bracing member. This increases material and manufacturing costs of the connection. Depending on the size of the structure the impact on the total structural costs can be significant.

Use of flattened tube in bolted connections offers advantages improving structural performance and decreasing costs due to a simpler manufacturing. The connection is made by flattening the member ends at the workshop resulting a plate-type section where the holes for the bolts can be drilled. The detail requires no welding and the member can directly be bolted to a gusset plate (Figure 1-4).

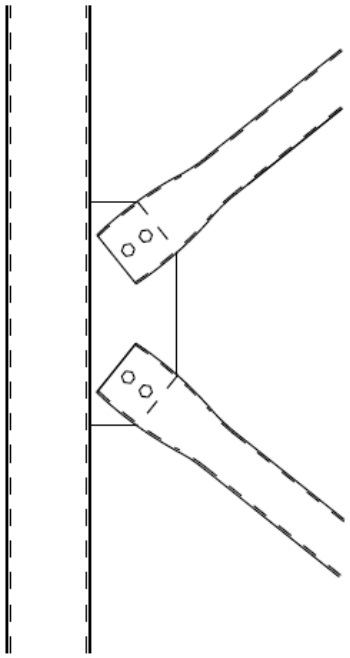

Figure 1-4 Bolted joint with flattened ends directly connected to a gusset plate.

1.2 Tube Flattening as a Manufacturing Method

The flattening of the tube can be done either in hot or cold conditions, however, cold flattening is often used as it is relatively simple, quick and cost-efficient. A proper choice for the ratio of the tube diameter to the tube wall thickness is indispensably affecting the flattening process. Generally, the flattening is always easier when the ratio between the tube diameter and the tube wall thickness increases. In the connections, various types of flattening are used based on the requirements for joint strength or the limits of the manufacturing. The general types of flattening are presented in Figure 1-5. [1]

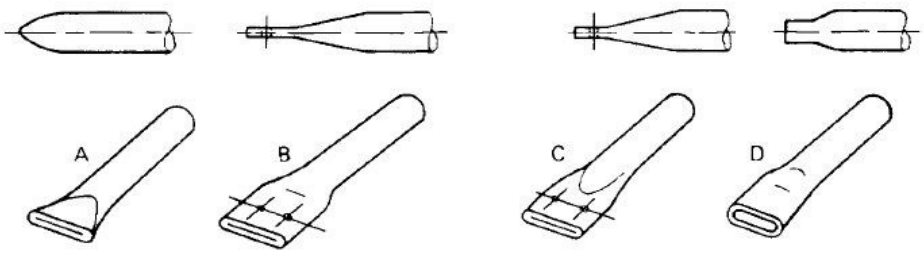

A. Cropping
B. Full flattening
C. Flattening with a recessed die
D. Partial flattening

Figure 1-5 Main types of flattening. [1]

1.3 Metallurgical Aspects

The manufacturing process induces residual stresses to the profile that can have a detrimental effect on the structural bearing capacity. The material stress-strain behavior may also be greatly altered due to large plastic deformations induced by the flattening process. The strain-hardening caused by cold forming increases the material yield strength but simultaneously decreases its elongation in fracture and thus ductility decreases.

1.3.1 Residual Stresses

Residual stress is the remaining stress in a body that is stationary and at equilibrium with its surroundings. Residual stresses can be divided in two categories; membrane and flexural residual stress (Figure 1-6) [2]. Residual stresses can be very detrimental to the performance of a material and can shorten service time of a component significantly. Alternatively, residual stresses can be beneficial as in cases of prestressing and toughening materials. [3]

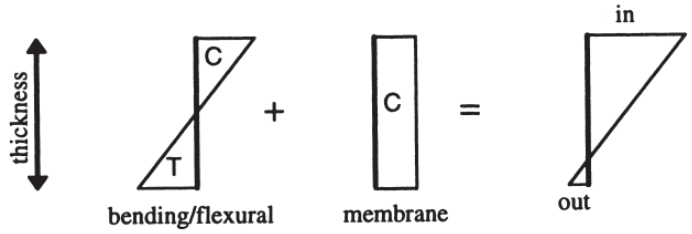

Figure 1-6 Two main residual stress types; flexural and membrane. [2]

The level of residual stress within a material is depending upon its location. Each tensile stress area must have a balancing compressive stress area to maintain equilibrium, in other words the sum of the forces acting across any arbitrary cut (see Figure 1-7) through the body must be zero. Across a cut perpendicular to x, this can be expressed mathematically as [4]:

$$\int \sigma_x w(z) dz = 0, \tag{1.1}$$

where $w(z)$ is the width in the y-direction as a function of z. Besides the force equilibrium the moments should also be in balance. This can be expressed mathematically about any axis in the y-direction as [4]:

$$\int \sigma_x w(z) z dz = 0\,. \tag{1.2}$$

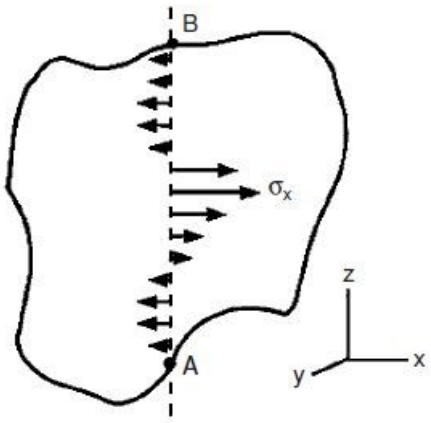

Figure 1-7 Imaginary cut of the material. [4]

When a metal is being subjected to a plastic deformation, internal stresses are primarily generated because of incompatibility [5]. On the other words, the different strains are occurring in different locations at the same time. Even though the manufacturing techniques have developed much over the last decades, it is highly unlikely that any manufactured component would be completely free from residual stresses induced during processing. [3]

1.3.2 Strength Enhancements

Cold forming or cold working is defined as a metal forming process or plastic deformation operation that is carried out at temperatures below the recrystallization temperature of the

material. The cold-formed section has sometimes significantly different mechanical properties when compared to the virgin material. The percentage increase in yield strength is more substantial than the increase in tensile strength. Since in cold worked areas the material shows considerably improved properties compared to the virgin material in the flat areas, the mechanical properties vary across the cross section as illustrated in Figure 1-8. Therefore, the yielding of the cross section always begins in the virgin parts of the material due to its lower yield strength. Once the virgin material has completely yielded, any additional loading will spread also to the corner areas. [6]

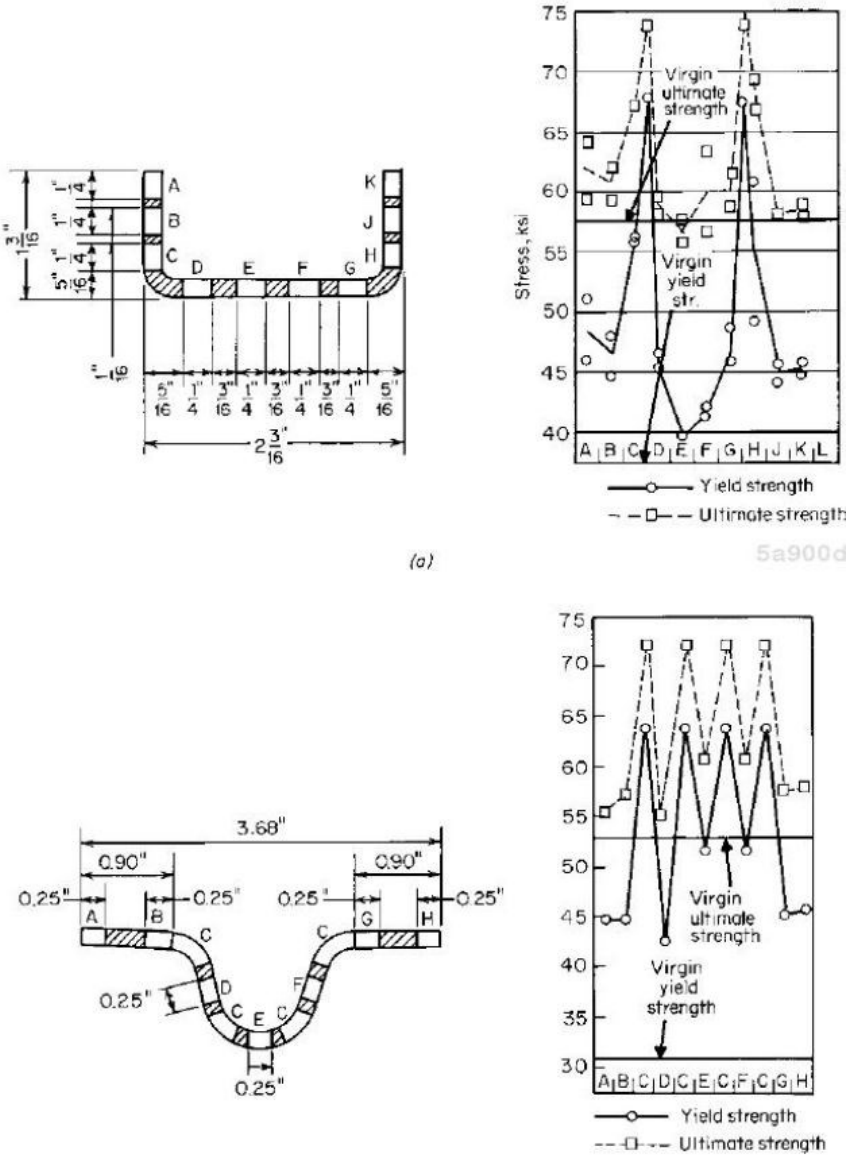

Figure 1-8 Strength enhancements due to cold work. [6]

In the mechanical properties, the changes are mainly caused by strain hardening and strain aging. In Figure 1-9, the curve A indicates the stress-strain relation of the virgin material. The curve B represents the unloading in the strain hardening range while the curve C

immediate reloading. The curve D is the stress-strain relation after reloading once the strain aging has occurred. Increase in yield strength can be observed on both curves C and D when compared to curve A. In addition, the ductility of the material decreases after strain hardening as the fracture strain decreases. [6]

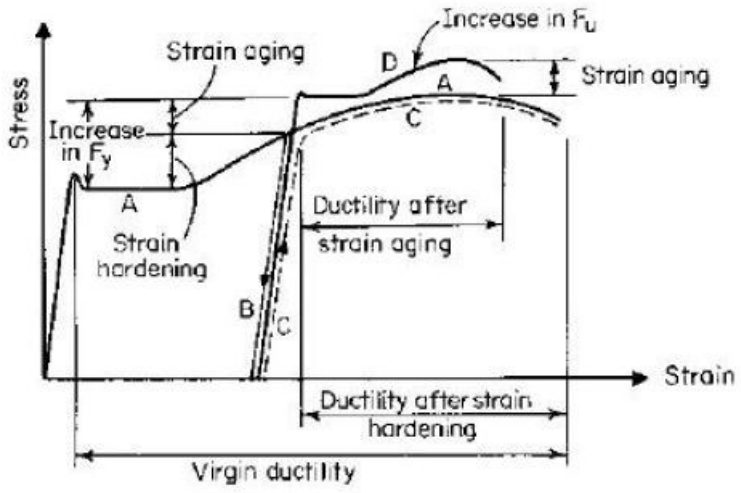

Figure 1-9 Effects of strain hardening and strain aging. [6]

1.4 Design Code Considerations

When the verification of a steel member verification against buckling is carried out according to the Eurocode 3, the residual stresses and geometric inaccuracies resulting from the manufacturing process are taken into account with an imperfection factor, which is depending on the shape of the geometry, the manufacturing method, the profile dimensions and the material strength [7]. As this approach is aimed to be conservative, the designer shall not go further into details with residual stresses and geometrical imperfections.

However, the application rules in Eurocode 3 may only be used when the cross-sectional shape of the profile is uniform [8]. Hence, when the member end is flattened, Eurocode 3 provides no guidelines to estimate initial conditions of the member and eventually no design equations for determining the resistance of the member or the connection.

The initial conditions of the flattened end member can be determined by simulating the manufacturing process. As a result, the initially deformed geometry and stress pattern are obtained. Since the end of the member is not prismatic but flattened, the geometric nonlinearities shall be automatically considered in the simulation. The structural imperfections in terms of residual stresses are represented by an initial stress pattern resulting from the manufacturing process as proposed in [9].

1.5 Research on Flattened End Members

The ease of manufacturing process has intrigued many researchers to study flattened end members. In 1996, El-Sheikh [10] investigated experimentally a new space truss system called Catrus (Figure 1-10) and found that the overall system was performing in a ductile manner nevertheless deformations were large in the top chord.

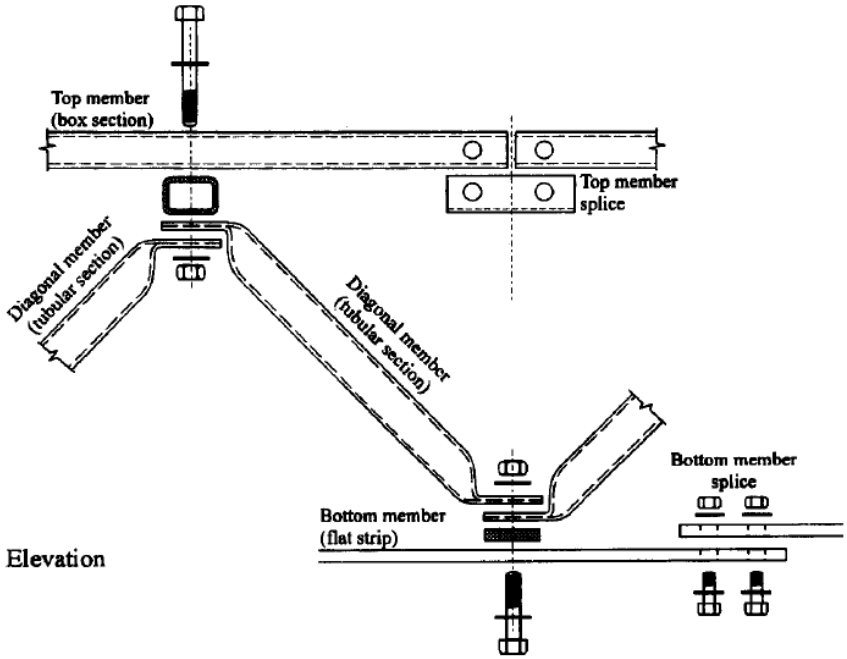

Figure 1-10 Catrus space frame system.[10]

In 2003, Mistakidis and Tsiogas investigated the failure modes of circular hollow sections with double flattened ends both in experimental and numerical ways. They found that the mode of failure is directly connected with the ratio of diameter to thickness of the tube. Higher t/D –ratios lead to a classical overall buckling failure while lower ratios promote the local buckling in the transition zone. The characteristic local failure mode of the transition zone is presented in Figure 1-11. [11]

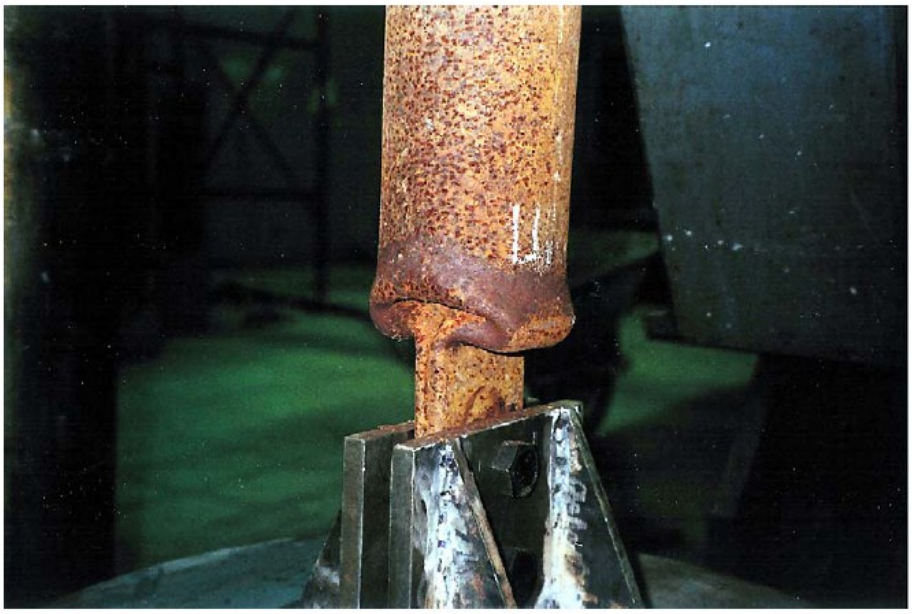

Figure 1-11 Characteristic failure mode in the transition zone. [11]

In 2005, a research group in State University of Rio de Janeiro investigated tubular space frame systems with end-flattened nodes experimentally (Figure 1-12). The experiments confirmed the use of excessive length for the flattened part has a detrimental effect on the structural carrying capacity and global stiffness. They also proved that the use of minimal length for flattened-ends improved the structural behavior. [12]

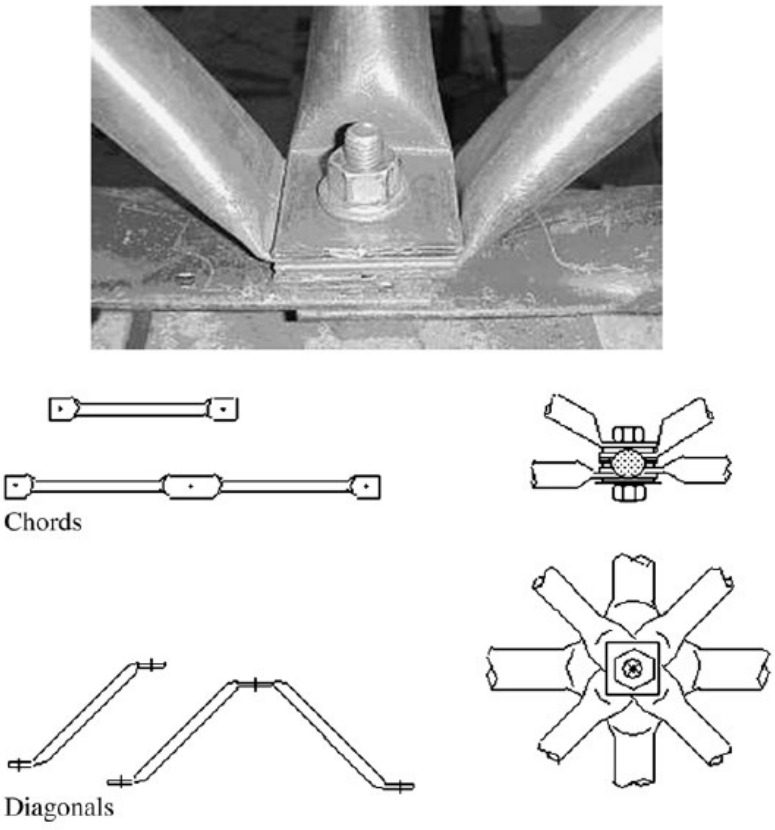

Figure 1-12 End-flattened node system. Collated from [12]

In 2014, Dundu conducted an experimental study of the circular hollow sections with flattened ends in compression. As a result, two different failure modes were observed. These are excessive deformation of the transition zone (Figure 1-13) and overall flexural buckling of the member (Figure 1-14). The excessive deformation of the transition zone results from the tendency of the flattened portion to penetrate into the circular region. As the flattened portion moves towards the circular region, it forces the transition zone to bulge outwards. [13]

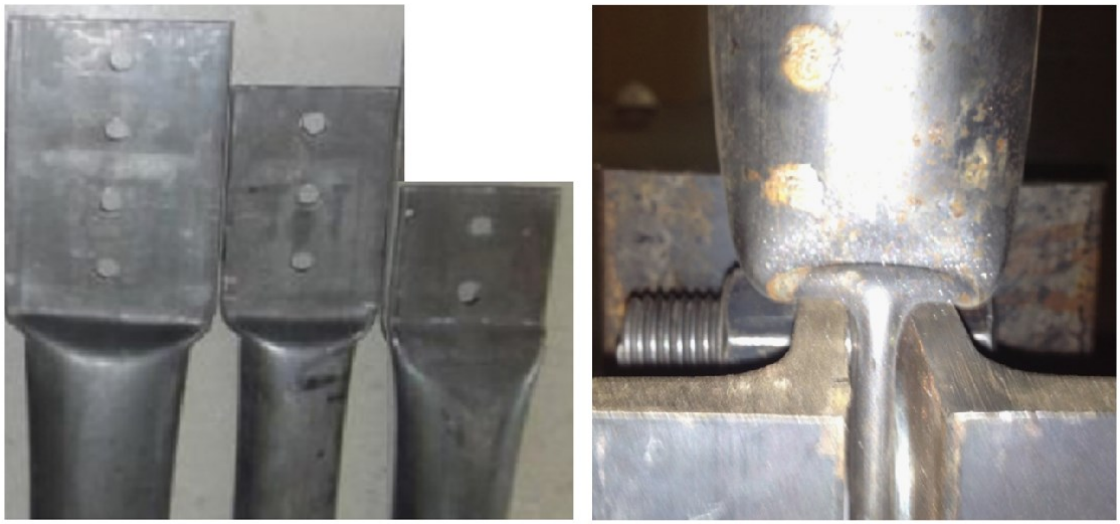

Figure 1-13 Punching effect of the flattened portion. Collated from [13]

Figure 1-14 Overall buckling of the member.

The excessive deformation of the transition zone is more common in sections with smaller slenderness ratios, larger diameter-to-thickness ratios and steels of lower strength. Experimental studies also show that the excessive deformation of the transition zone is not significally affected by either the length or the slenderness of the member. [13]

The overall flexural buckling of the member is typically occurring in sections with large slenderness ratios, small diameter-to-thickness ratios and steels of high strength. The length of the full flattened region should be as short as possible to avoid any local buckling effect that would prevent the utilization of full overall buckling resistance. [13]

1.6 Scope and Outlines of the Thesis

This thesis provides a numerical approach for estimating the residual stress patterns in circular truss members with flattened ends. The main target is to obtain a residual stress distribution resulting from the flattening numerically and to study its influence on the load bearing capacity against axial loading. The proposed analysis method will be validated with a reference models based on experimental data.

The validation will be done by conducting a numerical simulation for bolt-connected circular member with flattened ends in compression. The residual stress pattern and deformed tube geometry is obtained by accurately simulating the tube flattening and

performing a springback analysis. The simulation of bolt hole drilling and fracture mechanic aspects are not included in the thesis.

The theoretical part of the thesis describes nonlinear finite element analysis theory, material behavior and selections to be generally made when performing metal forming simulations. The numerical part consists of manufacturing simulation, springback evaluation and bearing resistance of the member under compressive axial loading. The last part introduces the proposed field variable distributions for stress and strain in the flattening stage and final stage after the springback. The effects of residual stress are evaluated on member behavior in compression.

2 Considerations in Metal Forming Simulations

The metal forming processes can usually be divided into massive forming and sheet metal forming. Based on the component geometry and resulting deformations states, it is common to use volume elements in massive forming and shell elements in sheet metal forming. The forming processes also evaluate the simulation results in a much different way. While in massive forming, the material flow, mould filling behavior, deformability and tool load are on focus, in sheet metal forming, deformability, thinning, crack probability, wrinkle formation and springback of the component are usually being investigated. [14]

In this thesis, the tube flattening simulation is considered as a massive forming simulation. The essential considerations in such finite element simulation are:

-Discretization method of the continuum

-Element formulation

-Material modeling

-Selection of the time integration method

-Evaluations on a quasi-static response

2.1 Discretization of a Boundary Value Problem

In metal forming simulations, the domain of the body can be discretized with different approaches. Two most commonly used approaches are Lagrangian and Eulerian methods although the recent ALE methods are increasingly being used [14]. This gives a short overview on each discretization method.

2.1.1 Lagrangian Method

In the Lagrangian method, the nodes follow the material particles. This means that throughout the forming process the state variables of particles change. Lagrangian approach is dominantly used with metal forming, but when conducting analyses with large-scale plastic deformations the mesh is easily distorted in the computational domain and remeshing is often required. However, the interpolation of the state variables between the distorted and the new mesh leads to more or less distinct smoothing of the state variables depending on the number of remeshing rounds. [14]

2.1.2 Eulerian Method

In the Eulerian approach the element mesh is fixed in space and movement of a continuum through the mesh is being observed. There is no mesh distortion for the material is flowing through the fixed mesh. The Eulerian methods are common in fluid dynamics. [14]

Figure 2-1 shows a comparison between the same model created with both Lagrangian and Eulerian approaches. In Lagrangian model, the two parts are modelled and both represent unique section with assigned material. In Eulerian model only one part is modelled. This Eulerian part defines the materials that can represent within the part. Next the materials are assigned to different regions within the part. Regions without material assignment are treated as a void. [15]

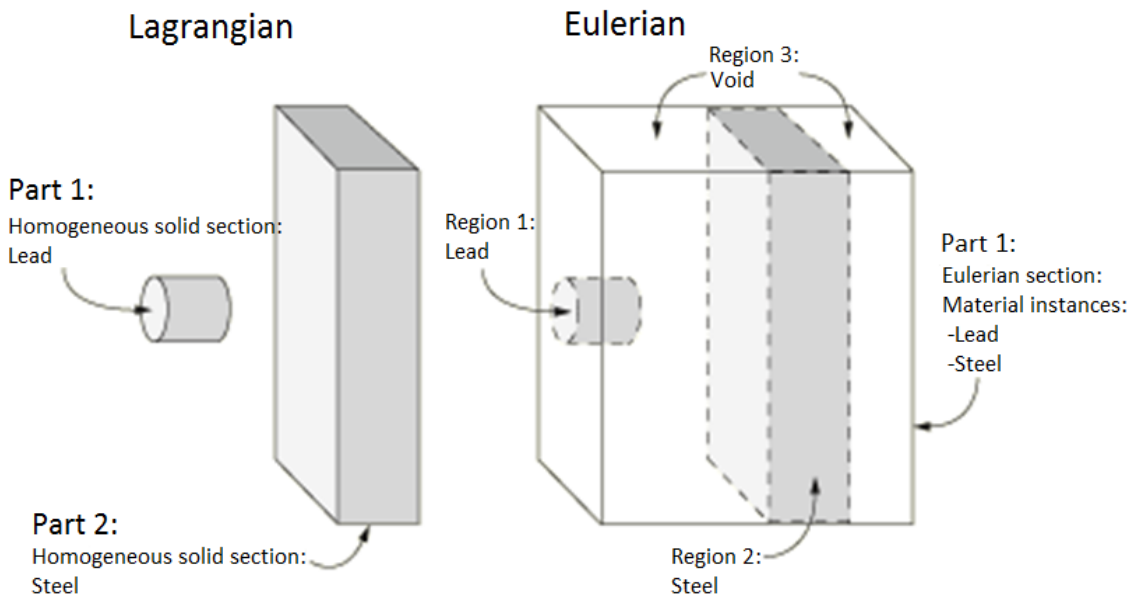

Figure 2-1 Comparison between Lagrangian and Eulerian techniques. Reproduced from [15]

2.1.3 ALE-method

The arbitrary Lagrangian-Eulerian (ALE) method is developed to simulate large deformation. It combines the advantages of Lagrangian and Eulerian approaches and minimizes their shortcomings. The ALE method does not change the topology of the structure and is therefore much faster than adaptive rezoning methods. It also maintains good element aspect ratios within the mesh. The research shows that ALE method is effective to cope with mesh distortions in large deformation analyses [16]. The comparison between Lagrangian, Eulerian and ALE-method is presented in Figure 2-2.

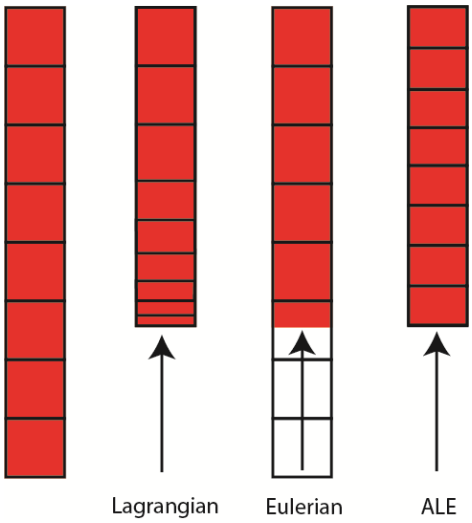

Figure 2-2 Comparison between different continuum representation methods. Reproduced from [17]

2.2 Element Formulation

The isoparametric formulation enables the generation of non-rectangular elements with curved sides and is mainly used in most engineering problems. The concept involves the interpolation of the geometry of the body and field variables with the shape functions in natural coordinate systems of elements. Depending on the dimension size of the problem, the shape functions can be constant, linear or quadratic. The field parameters are approximated in the natural coordinate system of an element and are differentiated with respect to global coordinates. It generally exhibits very good accuracy with an arbitrary geometry mapping to finite element mesh and is also well suited for nonlinear problems. [18,19]

2.2.1 Element Types

In case of quadrilateral 2D plane Lagrange elements, the element with linear interpolation functions consist of four nodes. If the shape functions are quadratic, midsize nodes are added and the node count increases to nine. With hexahedral 3D Lagrange elements the node count with linear shape functions is eight and with quadratic shape functions 27.

If the internal nodes are excluded and the boundary nodes are only considered, the Lagrange elements become serendipity elements. This leads to a total node count of eight with quadrilateral plane elements and 20 with hexahedral volume elements. All isoparametric elements lose accuracy when subjected to distortion resulting in nonrectangular shape. The nine- and 27-node elements are much less sensitive to distortion than eight- and 20-node elements. The element types for quadrilateral 2D elements are presented in Figure 2-3 and for hexahedral 3D elements in Figure 2-4. [18]

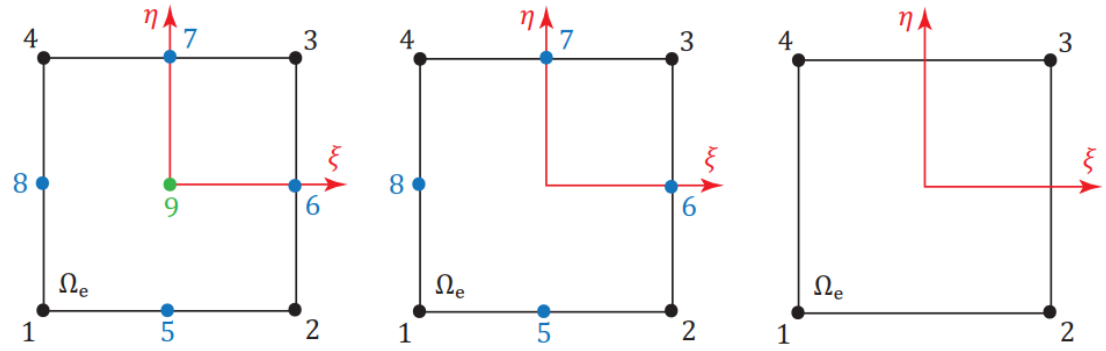

Figure 2-3 Quadrilateral 9-node, 8-node and 4-node elements.

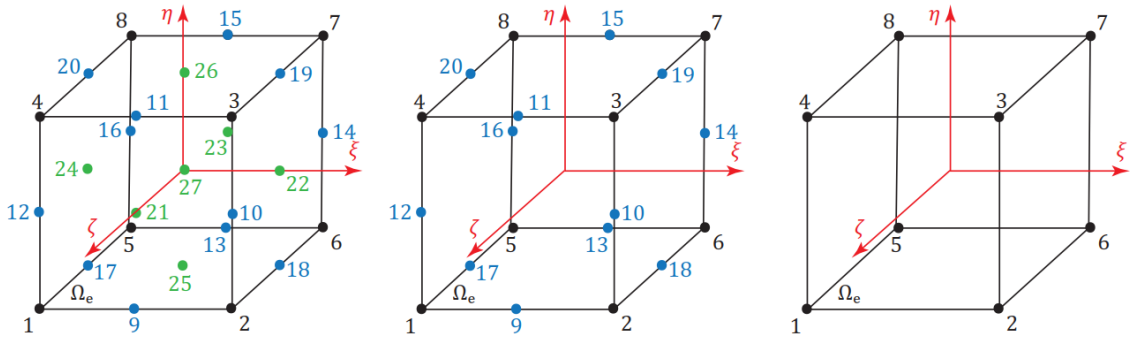

Figure 2-4 Hexahedral 27-node, 20-node and 8-node elements.

2.2.2 Element Instabilities

Usually first order approximations are used in the element formulation in problems involving elasto-plastic deformation since they tend to be more robust when large mesh distortion takes place. This leads to more economical solution time due to sparser tangent matrix used in the incremental solution discussed later in chapter 2.4. [18]

However, elements with low interpolation order cannot simulate pure bending states without transverse shear deformations. As these deformation states should not be present in the bending states, artificial increases occur in the stiffness matrix. This phenomenon is called the transverse shear locking. The shear locking can be avoided by using a higher interpolation order or reduced integration.

As mentioned before, although the use of higher interpolation order would eliminate the shear locking it leads to non-sparse tangent matrices and increases the computational time greatly. The reduced integration method also eliminates the shear locking, but can lead to rank deficiency of the tangent matrices leading to singularity. This element instability is known as the hourglass mode (Figure 2-5). [18,19]

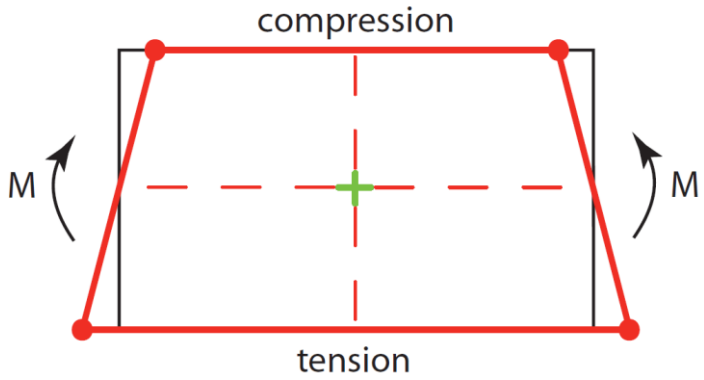

Figure 2-5 Behavior of single reduced integration element in bending. Reproduced from [17]

The existing hourglassing with first order reduced integration elements does not necessary lead to structural instability since it is compensated with artificial strain energy and the balance is maintained. However, it leads to falsified results since the strains are artificial resulting in excessive computed deformations [19]. An appropriate number of elements through the thickness of the body should be used in the mesh when using first order reduced integration elements in bending dominated problems (Figure 2-6).

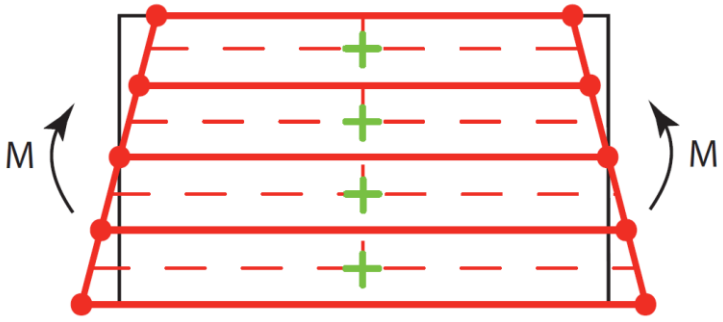

Figure 2-6 Behavior of multiple reduced integration elements in bending. Reproduced from [17]

2.2.3 Element Type Selection

The selection of elements plays an important role in metal forming analyses. As the use of higher order elements would completely remove any instability phenomenon, it often leads to non-economical solution times due to non-sparse tangent matrices. The use of reduced integration elements is often recommended in metal forming analyses. To maintain the same accuracy as with higher order elements and quadratic shape functions, more elements are needed with simple elements and linear shape functions. The calculation time with 8-node elements is less than 30 % of calculation time with 20-node

elements [15]. In case of large displacement analyses, the simple element formulations are known to give more robust numerical model and analysis than higher order elements [20].

Even though the reduced integration elements are less susceptible to shear locking effect, the zero energy modes may occur in analysis. The general recommendation according to [15] is to use at least four elements over the thickness of the body when using reduced integration elements in bending dominated problems. In addition, a proper hourglass control should be used. The hourglass energy should remain small compared to the internal energy of the system. The proposed limit value by [20] is 5 %.

2.3 Material Modeling

Beside the kinematic relations and balance laws, the information of the material response of a body is required to solve a boundary value problem. The constitutive equations describe the material response of a solid body when it undergoes a series of events as loading or temperature changes and deforms. For isotropic materials, the material response is the same regardless of the direction. The deformation for elasto-plastic materials as steel can be divided into elastic and plastic deformation. The elastic deformation reverts during the unloading phase, whereas the plastic deformations are permanent.

2.3.1 Uniaxial Elasto-plastic Material

Figure 2-7 describes a typical uniaxial elasto-plastic constitutive behavior. Until point A, the material response is elastic and the loading and unloading path is the same. Plastic deformations begin to take place after the stress in the material exceeds a threshold value known as the yield stress. Due to the hardening behavior, the stress is higher in point B than in point A. If unloading takes place in point B, the stress response follows a straight-line parallel to the elastic tangent between the origin and point A. However, the plastic flow resumes in point C. [18]

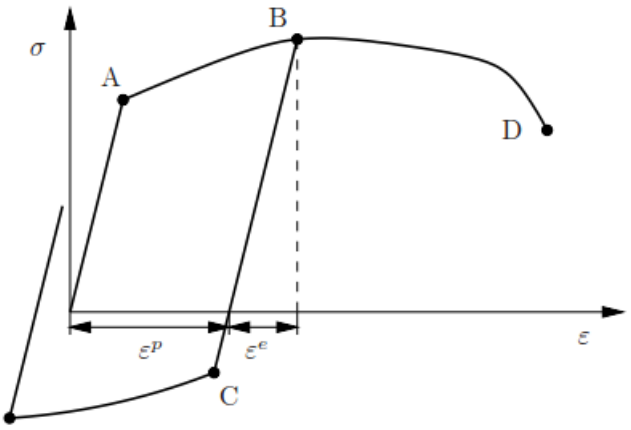

Figure 2-7 Uniaxial elasto-plastic constitutive behavior. [18]

2.3.2 Hardening Laws

If a material is first under tensile loading followed by compressive loading, the new yield strength value in compression tends to be lower than the last tensile yield stress value. The phenomenon is known as the Bauschinger effect and can be explained with the changes in the metal microstructure caused by plastic deformation [21].

The two most commonly used strain hardening laws in practical applications are isotropic hardening model and kinematic hardening model. With isotropic hardening models, the Bauschinger effect is ignored and the curves for tension and compression are identical. The kinematic hardening law assumes the change of stress of yielding in the reverse loading is equal to twice the initial yield stress. There are also mixed hardening models available that represent the material behavior between these two models. It is notable, that the kinematic and mixed hardening models induce anisotropic behavior in the material. The hardening models are presented in Figure 2-8. [21]

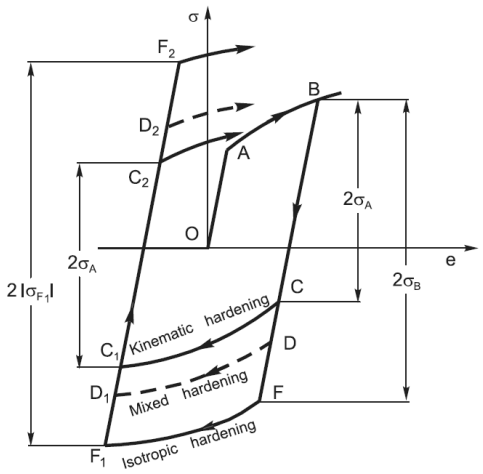

Figure 2-8 Hardening laws. [21]

2.3.3 Material Modeling in Structural Applications

The engineering strain measure if often used with nonlinear structural applications where strains are small since it can describe arbitrary rigid body motions correctly [18]. The strains are considered small when they are namely lower than 4% [21]. The small strain theory presents the stresses in the initial configuration which assumes the same geometric conditions in the current configuration in derivation of stress parameters. The small strain theory cannot therefore be used with problems involving large strains since it is not representing the material behavior correctly.

As the small strain theory is only applicable with infinitesimal strains, modelling of finite plasticity is essential for engineering analyses like metal forming, cutting and pile driving in the soils. This means that true or logarithmic strains and true or Cauchy stresses should be adopted in the analysis. [21]

Before any modern data processing systems, it was common to scale the load-extension diagram by dividing load by the initial cross-sectional area to obtain the engineering stress-strain curve. This curve often has an advantage that it is not dependent of the initial dimensions of the test-piece used in tensile testing. However, the resulted curve is not a true material property curve, because during the test the cross-sectional area of the test-piece will diminish so that the true stress of the material is actually greater compared to the engineering stress. The engineering stress-strain curve is still commonly used to derive a number of material properties. The Figure 2-9 shows a typical material response of obtained from physical experiment. [22]

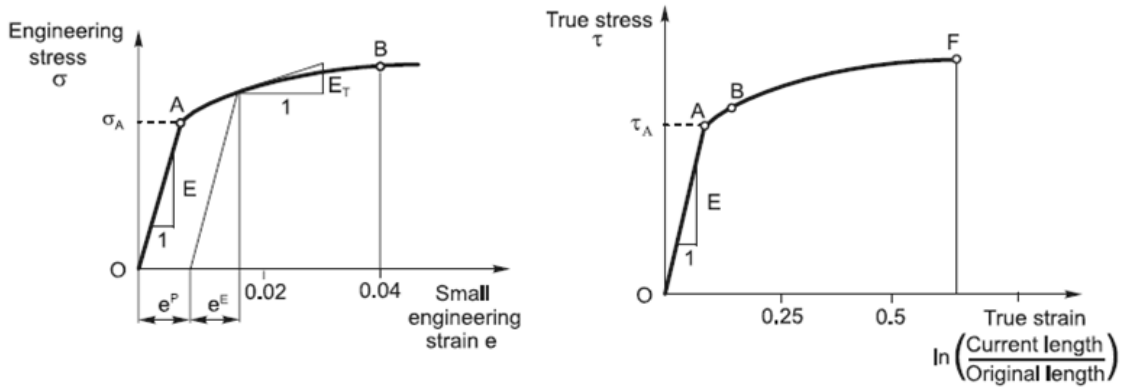

Figure 2-9 Typical uniaxial stress-strain dependency. Reproduced from [21].

When the results of tensile testing are used to predict the behavior of the material under other forms of loading, it is preferable to plot the data in terms of true stress and true strain. True stress and true strain can be derived from the engineering quantities as long as the deformation is uniform along the involved section. These relations are presented in equations (2.1) and (2.2) [23] :

$$\sigma_{true} = \sigma_{eng}(1 + \varepsilon_{eng}) \quad (2.1)$$

$$\varepsilon_{true} = \ln(1 + \varepsilon_{eng}) \quad (2.2)$$

2.4 Time Integration Method

There are two basic solution methods available for time integration, implicit and explicit method. In both of these methods, the nonlinear response of the structure is obtained incrementally. Let us consider a nonlinear load-displacement curve presented in Figure 2-10. For determining the response of the structure, the loading has to be specified as a function of time. Moreover, the total time has to be incremented so that the nonlinear solution path can be followed. [15]

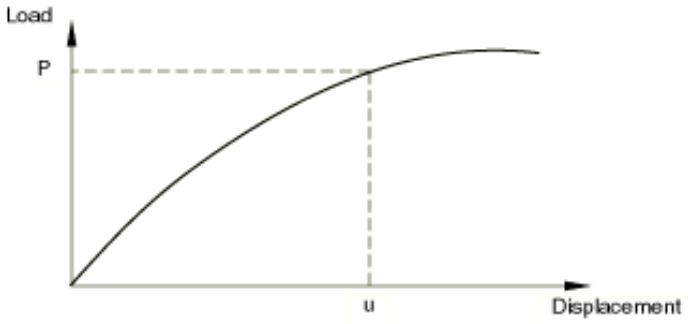

Figure 2-10 Nonlinear load-displacement curve. [15]

The dynamic equilibrium represents the balance between the inertia forces, damping forces and elastic forces in a body and the external loads acting on its surface. After some numerical manipulation, discretized form of the principle of virtual work in a finite element domain can be presented as [19]:

$$[M]\{\ddot{D}\} + [C]\{\dot{D}\} + [K]\{D\} = \{R^{ext}\}, \quad (2.3)$$

where

$[M]$ is the structural mass matrix,

$\{\ddot{D}\}$ is the acceleration vector,

$[C]$ is the structural damping matrix,

$\{\dot{D}\}$ is the velocity vector,

$\{K\}$ is the structural stiffness matrix,

$\{D\}$ is the displacement vector,

$\{R^{ext}\}$ is the external load vector.

In case of non-viscous materials, like metals, the damping term is often excluded from the equilibrium equation since it does not represent correctly structural damping [19]. In case of static equilibrium, where the body is not in motion, the dynamic equilibrium equation is reduced to:

$$\{R^{ext}\} - [K]\{U\} = 0, \tag{2.4}$$

2.4.1 Iterative Implicit Time Integration

In implicit methods, the nonlinear response is obtained by using a series of linear approximations. The Newton's method is a widely used implicit technique. The Newton's method uses iterative numerical techniques to find an equilibrium state on each time increment. Each time increment may require many iterations to satisfy the predefined accuracy requirements. An example of first and second iteration in a time increment is shown in Figure 2-11. When the equilibrium state of the current time increment is achieved, an inversion of the nonlinear equivalent stiffness matrix is needed in order to solve the displacement vector. [15]

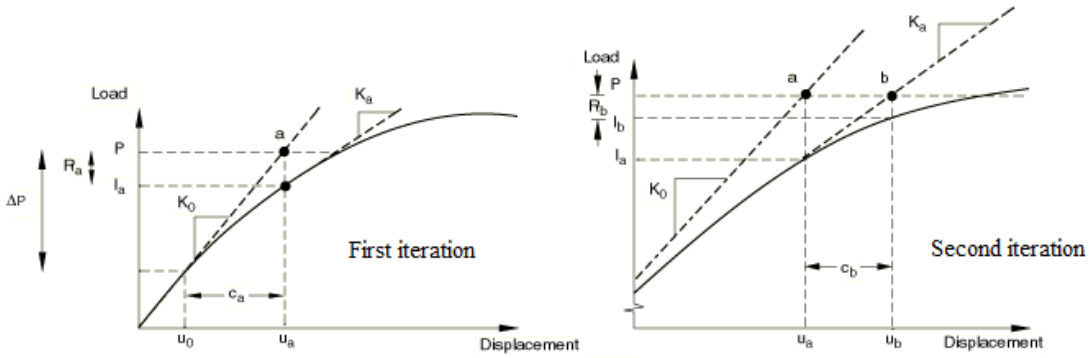

Figure 2-11 First and second iteration in an increment. [15]

When iterative methods are used, realistic criteria should be used for the termination of the iteration to ensure the efficiency of an incremental solution. After each completed iteration, the obtained solution should be checked whether it has met the convergence tolerances or whether the solution is diverging. If the convergence tolerances are too loose, the solution tends to be inaccurate while the criteria being too tight it is likely that the solution is needlessly accurate and much computational time is spent in vain. [24]

2.4.2 Direct Explicit Time Integration

The explicit approach is also an incremental method, but apart from traditional implicit method, it uses central difference algorithm that advances explicitly during time. This means that the model state in the end of each time step is determined purely by the results

of preceding time steps. The principle of central difference algorithm is shown in Figure 2-12.

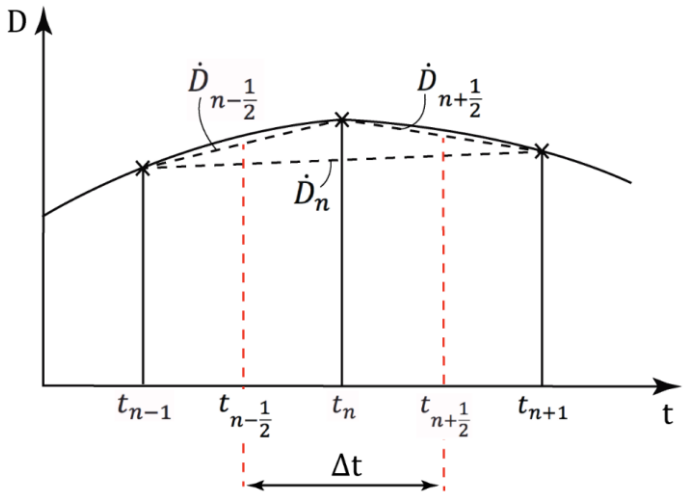

Figure 2-12 Central difference time integration method. Reproduced from [25]

In central difference algorithm, the equation of motion introduced previously is modified by lagging velocity by half time step [19]. Therefore, the equation of motion takes the form [19]:

$$[M]\{\ddot{D}\}_n + [C]\{\dot{D}\}_{n-1/2} + [K]\{D\}_n = \{R^{ext}\}_n \tag{2.5}$$

The nodal acceleration vector can be derived from Eq :

$$\{\ddot{D}\}_n = \left(\{R^{ext}\}_n - [C]\{\dot{D}\}_{n-1/2} - [K]\{D\}_n\right)[M]^{-1} \tag{2.6}$$

The approximations for velocity and displacement vectors when integrated explicitly through time are obtained from [15]:

$$\{\dot{D}\}_{n+1/2} = \{\dot{D}\}_{n-1/2} + \frac{\left(\Delta t_{n+1/2} + \Delta t_n\right)}{2}\ddot{D}_n \tag{2.7}$$

$$\{D\}_{n+1} = \{D\}_n + \Delta t_{n+1/2}\{\dot{D}\}_{n+1/2} \tag{2.8}$$

For complete derivation of equations (2.7) and (2.8), see [19].

The explicit dynamics analysis procedure utilizes the use of lumped element mass matrices, which is diagonal and requires no inversion. This, combined with the explicit integration rule, provides the computational efficiency of explicit solvers [15].

Solving the displacement vector $\{D\}_{n+1}$ requires that the internal load vector $\{R^{int}\}_n$ is known. The internal load vector is easy to evaluate because the constitutive nonlinear material models are functions of strain and the strain at time $n+1$ is known. This makes the explicit methods perform well with strongly nonlinear materials. [19]

The solution accuracy in implicit analysis is monitored with convergence criterion. However, since there are no iterations involved in explicit analysis, the solution accuracy cannot be controlled with the same principle. In order to produce accurate results, the time steps have to be very small for accelerations to remain nearly constant during an increment [15].

Explicit solvers considers the solving problems as wave propagation problems where residual forces are propagated as stress waves between the elements. In order to obtain a stable solution, the time increment has to be less than the stable time increment. The central difference operator is defined conditionally stable, meaning that the time increment is capped by numerical stability. Numerical instability is indicated by an obvious erroneous time-history solution that grows unbounded [19]. In terms of the highest eigenvalue in the system, the stability criterion is [19]:

$$\Delta t \leq \frac{2}{\omega_{max}}, \tag{2.9}$$

where

Δt is the time increment

ω_{max} is the highest eigenvalue in the system.

With stress propagation problems, there are often spurious oscillations or noise created by the algorithm involved in the structural response time-history. The mesh cannot accurately resolve the spurious oscillations and usually a small amount of damping is introduced to dissipate the high-frequency motion since their contribution to the structural response is insignificant [19]. Added damping reduces the stability limit, but it is required for stable integration. When damping is taken into account the expression (2.9) takes the form [19]:

$$\Delta t \leq \frac{2}{\omega_{max}}(\sqrt{1+\xi^2}-\xi), \tag{2.10}$$

where

Δt is the time increment

ω_{max} is the highest eigenvalue in the system

ξ is the fraction of critical damping in the highest mode.

The size of the time increment is limited by the Courant-Friedrichs-Lewy (CFL) condition, implying that induced stress wave cannot travel in a single time step farther than the smallest characteristics element dimension [19]. This maximum stable time increment size can be estimated from [19]:

$$\Delta t \leq \frac{L^e{}_{min}}{c_d}, \tag{2.11}$$

where

Δt is the time increment

$L^e{}_{min}$ is the smallest characteristic element dimension in the element mesh

c_d is the dilatational wave speed of the material.

For linear elastic material the dilatational wave speed is expressed as:

$$c_d = \sqrt{\frac{E}{\rho}}, \tag{2.12}$$

where

E is Young's modulus of the material

ρ is the density of the material.

It can be observed from equation (2.11) that the size of the stable time increment will be reduced if characteristic element length is decreased or dilatational wave speed of the material is increased. Furthermore, as stated in equation (2.12), the dilatational wave speed of the material will be increased if stiffness of the material is increased or density of the material is decreased.

2.4.3 Selection of the Time Integration Method

A lack of convergence and enormous calculation time are general issues when conducting highly nonlinear problems with conventional implicit finite element method. Especially when dealing with highly nonlinear transient dynamic problems, extremely small time steps of only few nanoseconds are required to obtain convergence [26].

The explicit method was developed by researchers to provide a more powerful alternative for solving complex nonlinear problems. Compared to implicit methods, explicit methods provide higher solving speed, more robust algorithm and stronger nonlinear capacity. Explicit methods can be applied in static and dynamic analysis of structures, especially when dealing with large deformations of otherwise highly nonlinear problems. [27]

Figure 2-13 illustrates the solution cost between implicit and explicit solvers when compared to the model size. It can be observed that with implicit solvers the solution time

increases more progressively when model size become large enough. With bulk metal forming simulations, the model size usually becomes large because high element count is often needed to accurately catch the highly nonlinear response of the body.

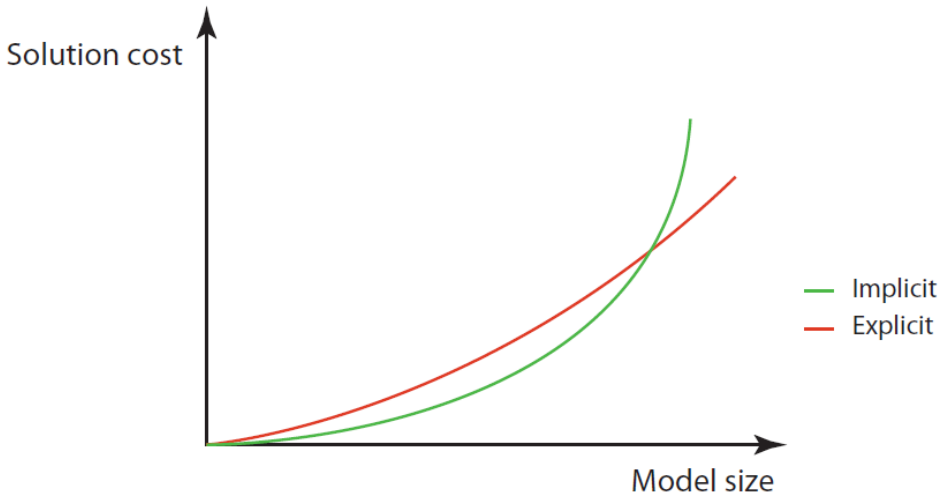

Figure 2-13 Solution time comparison. Reproduced from [17]

2.5 Quasi-Static Response

The nature of the explicit dynamic method is fully dynamic, originally developed for modeling high-speed impact events. In these types of events, the inertia effects of a body are in a dominant role in the solution. Metal forming processes are usually considered as quasi-static phenomena where inertia effects of a body are considered negligible. Usually it is computationally inefficient to model quasi-static problems using actual time of the process due to the small time increment required for stable integration, which leads to a large number of increments. [15]

As previously mentioned in chapter 2.4.2, the Courant-Friedrichs-Lewy condition limits the stable time increment to:

$$\Delta t = \min\left(\frac{L^e}{c_d}\right), \tag{2.13}$$

To find a cost efficient solution for the problem, the event has to be accelerated in some way. However, when the event is being accelerated, the state of static equilibrium evolves into a state of dynamic equilibrium and the inertia forces in a body become more dominant. The solution is no longer considered quasi-static but dynamic. The key is to find the shortest time period for the forming process in which the inertia effects remain insignificant. It is possible to artificially speed up the process by either increasing the load rates or using mass scaling. [15]

2.5.1 Loading Rates

The natural time of an event refers to the actual time taken for the physical process. It can be usually assumed that modeling a quasi-static process in its natural time will result in accurate static results. The loading rate can be increased to make the same physical event occur in less time. This requires that the solution is close enough to the true static solution and the dynamic effects can still be neglected. However, the material strain rates resulting from the accelerated simulation are artificially high by the same factor that is applied to increase the loading rate. If the material strain rate is sensitive, it is preferable to use mass scaling for economical solution since the material strain rates increase by the same factor as the loading rate. [15]

2.5.2 Mass Scaling

In cases where material strain rate plays an important role, the simulation can be artificially accelerated with mass scaling. As discussed in chapter 2.4.2, the dilatational wave speed of the material is:

$$c_d = \sqrt{\frac{E}{\rho}} \tag{2.14}$$

When the material density ρ is artificially increased with a factor of f^2, the dilatational wave speed of the material is decreased with a factor of f. Eventually the size of a stable time increment is increased with a factor of f. This way it is possible to perform the same analysis in a same natural period in less time, since fewer increments are required. As with increased loading rates, also the mass scaling amplifies the inertia effects of a body and therefore can lead to erroneous solution when excessive. [15]

2.5.3 Energy Balance

By monitoring the various energy states in the model it is possible to evaluate whether the simulation is yielding an appropriate quasi-static response or whether the inertia effects have become too dominant. In a proper quasi-static simulation, the external work is nearly equal to the internal energy of the system. As inertia effects should be negligible, the velocity of the material is very small and therefore the kinetic energy should be very small. In case of deforming material, according to the guidelines, the kinetic energy should not exceed a small fraction of 1 % of its internal energy during most of the process. In the early stages of forming, it is not usually possible for kinetic energy to remain small as the forming specimen is in motion before any actual deformation takes place. [15,20]

3 Numerical Analysis of Model Used for Validation

Dundu investigated experimentally the behavior of circular hollow members with flattened ends in compression. The flattening method used was full flattening and bolted connections were used. The prepared specimen prior to loading is presented Figure 3-1. The used test setup is presented in Figure 3-2. A notion was made that tubes with larger diameter-to-thickness ratios and smaller slenderness ratios tend to fail due to large inelastic deformation of the transition zone [13].

Figure 3-1 The flattened tube member prior to loading. [13]

Figure 3-2 The experimental test setup. [13]

This chapter provides a numerical analysis of one of the tested tubes and seeks to simulate the flattening process, the springback and the inelastic failure mode observed in the experimental study. The effect of residual stresses is also studied. The sequential analysis of the flattened tube is made in three parts. The first part of the analysis is the tube flattening. The tube section is squeezed in the lateral direction with flattening dies to its flattened form. In the second part of the analysis, the springback of the flattened tube is evaluated and the final deformed geometry and stress state are acquired. In the third part of the analysis, the maximum compressive resistance of the tube is determined. The analysis phases are shown in Figure 3-3.

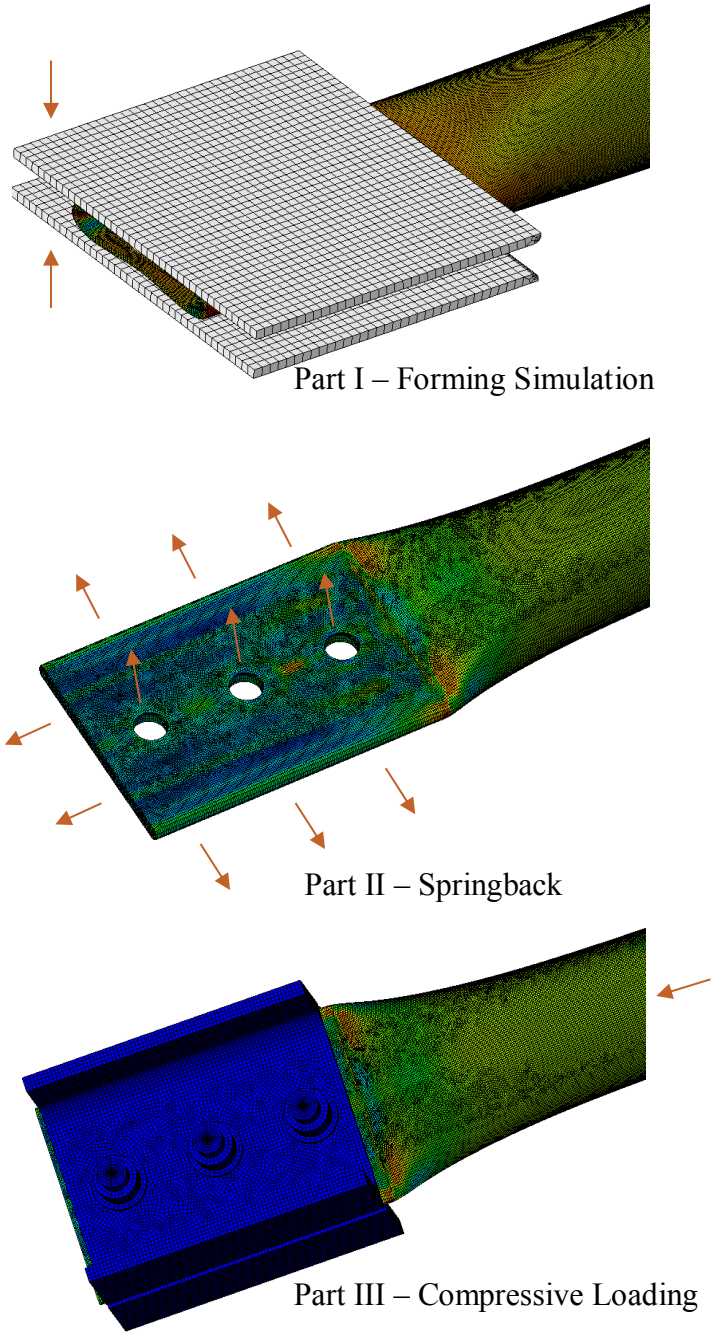

Figure 3-3 Three phases of the sequential analysis.

3.1 Analysis Path for Tube Flattening Simulation

The flattening simulation is conducted with Abaqus explicit solver where key analysis parameters are the length of time period, mass scale factor and hourglass control method. The first goal is to obtain a proper time period where the inertia effects remain small enough. The second goal is to find proper hourglass control method for keeping artificial strain energy small enough to yield realistic response. The results of the analysis parameter study are presented in chapter 3.2.7. Once the analysis has yielded a proper quasi-static response, the overall analysis may proceed to the second part.

When a metal is being formed, the elastic and plastic deformations received provide the information required to evaluate the springback effect. Whenever there is a stress in the structure, there will also be some elastic strain incorporated in the total strain. The quantity of elastic strain is small, typically less than one per mil. The elastic strain is often neglected, but in some cases, it can be crucial part in the analysis. [22]

Flattening of a tube is a typical example that involves permanent plastic flow and large strain rates. During an unloading phase, after the tube end is flattened, the elastic strain reverts and gives the flattened end a small elastic shape change. This elastic shape change is called the springback effect. The springback of the tube is evaluated in the second part of the overall analysis. The analysis model from the first part is copied as a new model but some actions are required before the analysis. The rigid tools are first deleted from the model assembly and the explicit time integration is changed to implicit to make sure that there is not any inertia effects present in the end of the analysis. The contacts and analysis conditions have to be redefined due to altered circumstances. The mesh topology of the tube however must remain the same since the stresses and strains from the first part are imported to the second part and used as its initial state. Once the analysis has converged, the overall analysis may proceed to the third part.

The compressive resistance of the flattened tube is obtained in the third part of the overall analysis. Again, some modifications in the model are required before the analysis. In case of bolted connection, the bolts and support profiles are included in the model. The evenly distributed compressive loading is modelled with a rigid punch with displacement boundary condition. The time integration method is switched back to explicit for more robust performance since the strains are again large. The contacts and analysis conditions are redefined to match the loading setup. It should be noted, that the mesh topology must again remain unchanged. The stresses and strains are imported as an initial condition from the last step of the springback analysis. As result, a force versus displacement graph is obtained for evaluating maximum compressive resistance and overall behavior of the tube. As in part one, the energy levels have to be monitored for ensuring a proper quasi-static response. The flowchart of overall analysis procedure is presented in Figure 3-4.

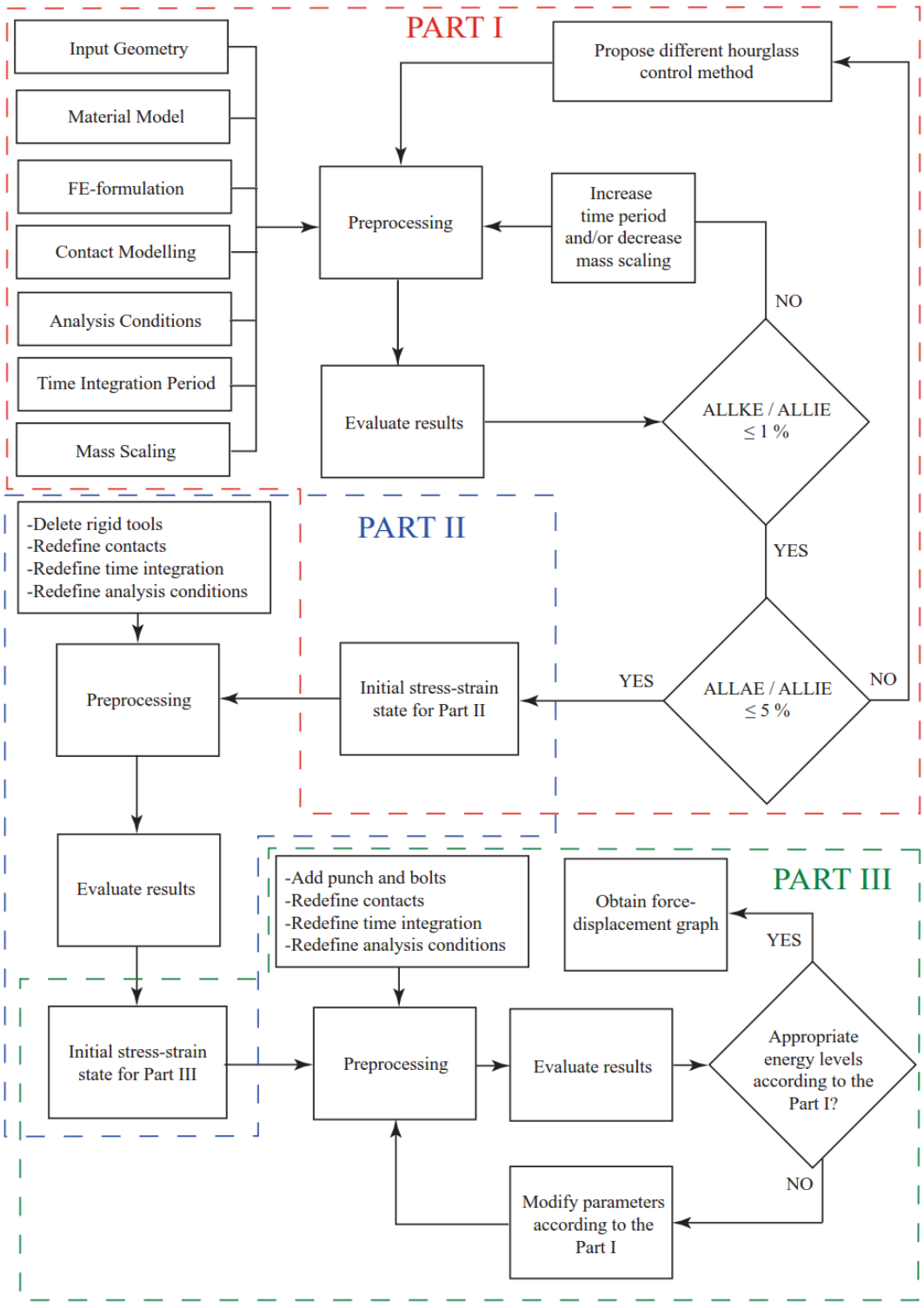

Figure 3-4 Flowchart of the overall analysis procedure.

3.2 Part I - Forming Simulation

The following subchapter explain in detail how the forming simulation takes place and how the selected time integration and element formulation parameters affect results. The analysis proceeds to part two when the conditions defined in Figure 3-4 are satisfied.

3.2.1 Input Geometry

A tube profile subjected to flattening is CHS76.2x4.0. Only one quarter of the tube is modelled and symmetry conditions with respect to ZY- and XZ-planes are applied. One rigid die is modelled to simulate the flattening die. A rigid plane in the longitudinal direction is applied to avoid any self-penetration. The relevant input geometry parameters are presented in Table 3.1. The input geometry of the forming setup is shown in Figure 3-5.

Table 3.1 Input geometry parameters

Tube diameter d_{tube} [mm]	76.2
Tube wall thickness t_{tube} [mm]	4.0
Length of the tube L_{tube} [mm]	800
Length of the die L_{r_die} [mm]	130

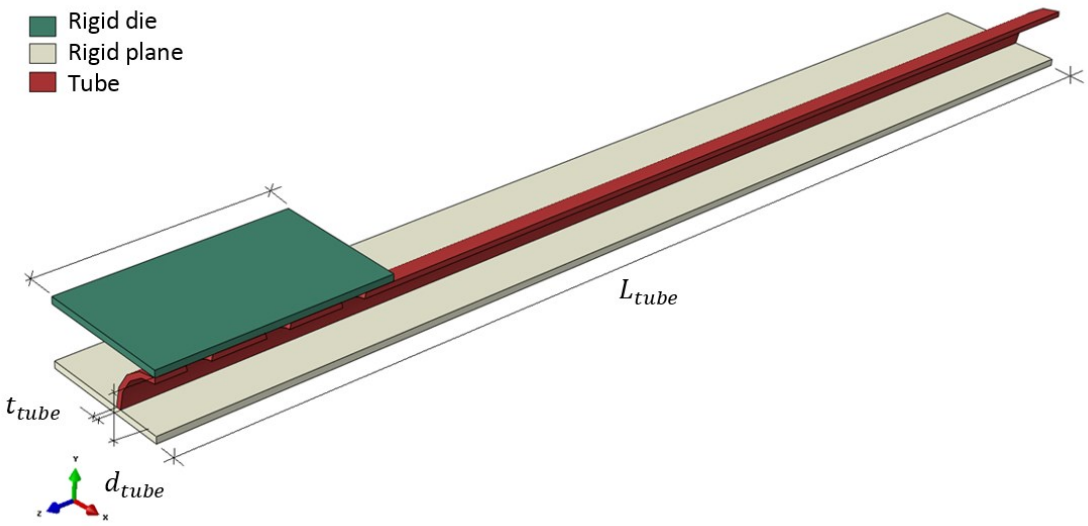

Figure 3-5 Input geometry of the forming setup.

Bolt holes for three M16 bolts are modelled prior to flattening as circular holes where the arc length is equal to the bolt hole diameter (18 mm) (Figure 3-6). The end distance of the first bolt is 30 mm and the spacing between the bolts is 55 mm.

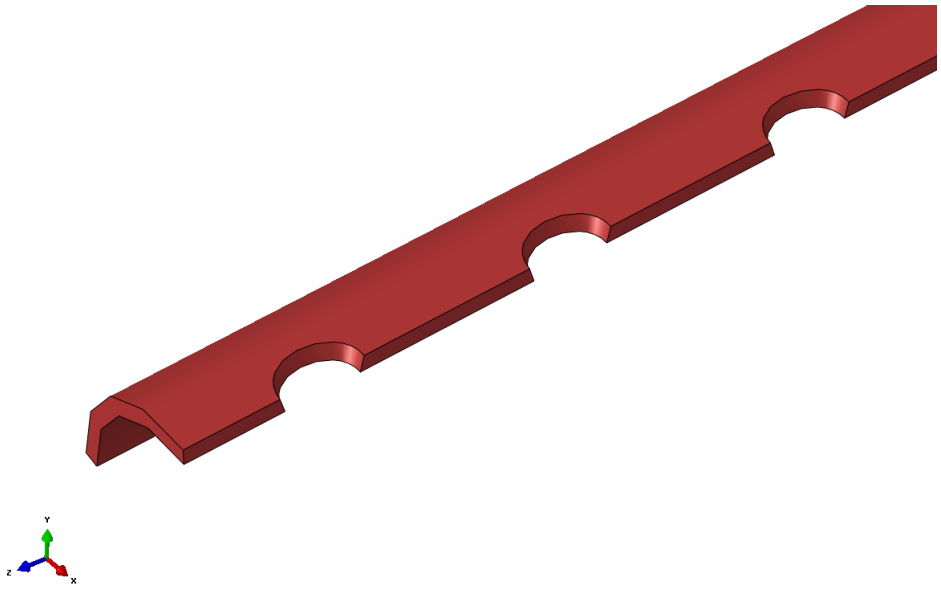

Figure 3-6 Bolt holes.

3.2.2 Material Model

The material of the tube is steel S355. As the plastic flow is significant and the straining is mostly monotonic, isotropic hardening behavior is assumed in the analysis. The average linear material properties obtained from the coupon tests [11] are presented in the Table 3.2.

Table 3.2 Measured linear material parameters (engineering stress-strain).

$E\ [N/mm^2]$	202410
υ [-]	0.3
$\rho\ [kg/m^3]$	7850
$\sigma_{eng,y}\ [MPa]$	395.00
$\varepsilon_{eng,y}$ [-]	0.001951

The material properties are next converted according to Equations (2.1) and (2.2) to represent a linear true stress-strain material model. The converted material properties are presented in Table 3.3.

Table 3.3 Converted linear material parameters (true stress-strain).

$E\ [N/mm^2]$	202410
υ [-]	0.3
$\sigma_{true,y}\ [MPa]$	395.77
$\varepsilon_{eng,y}$ [-]	0.001949

The Ramberg-Osgood relation is used to model the plastic portion of the stress-strain curve for smooth material response. The proposed true cyclic stress-strain curve is described according to [20] as:

$$\varepsilon = \frac{\sigma}{E} + \left(\frac{\sigma}{K}\right)^{10} \tag{3.1}$$

where the value of the coefficient K is $600\ MPa$. The cyclic Ramberg-Osgood stress-strain curve is described in Figure 3-7. When the linear elastic portion (the orange line in Figure 3-8) based on the measured material properties is combined with the plastic portion (the purple line in Figure 3-8), the curve takes its final shape as presented in Figure 3-8. A linear plastic region (the green line in Figure 3-8) is added to connect the two curves. Before the plasticity data can be input to Abaqus, the elastic strain $(\frac{\sigma}{E})$ needs to be subtracted from the total strain.

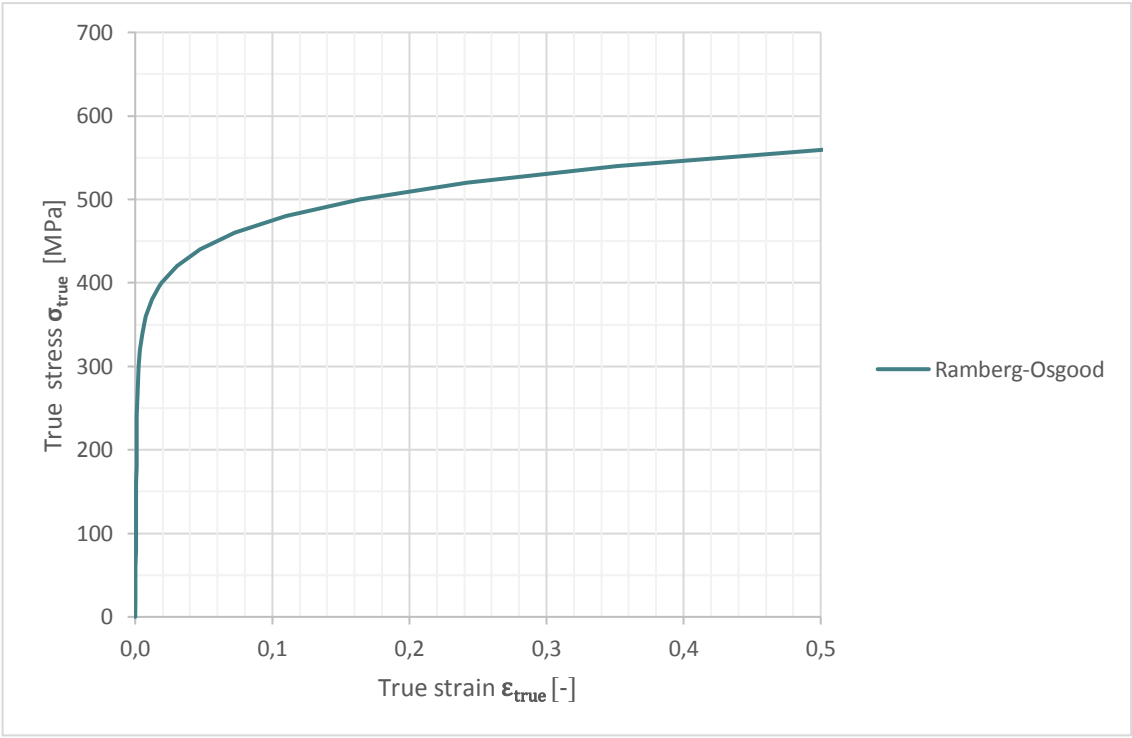

Figure 3-7 The true cyclic nonlinear material model.

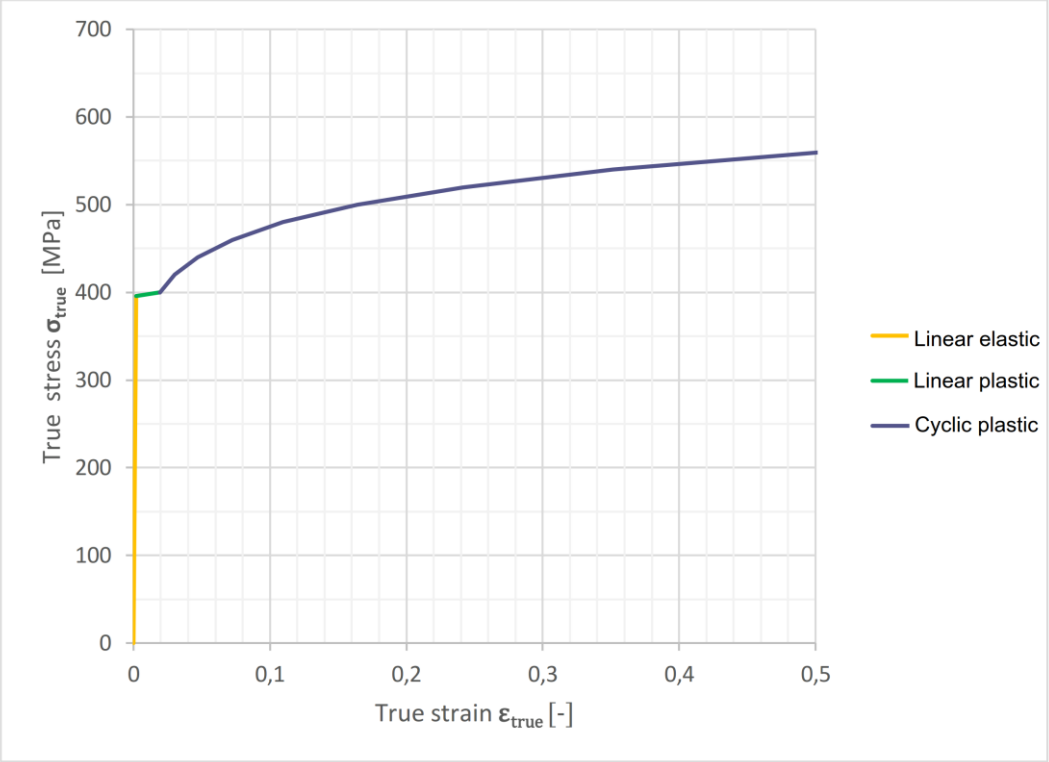

Figure 3-8 Combined nonlinear material model.

3.2.3 FE-modelling

The body of the tube is discretized with 8-node reduced integration solid elements (C3D8R) with added hourglass control according to the recommendations discussed in chapter 2.2.3. First order accuracy and standard distortion control are used in the element formulations. The discretized forming setup is presented in Figure 3-9. Four element layers over the thickness of the tube is used (Figure 3-10). Four different hourglass controls are evaluated to monitor the shear locking effects and zero energy modes discussed earlier in 2.2.2. The hourglass control definitions are presented in Table 3.4.

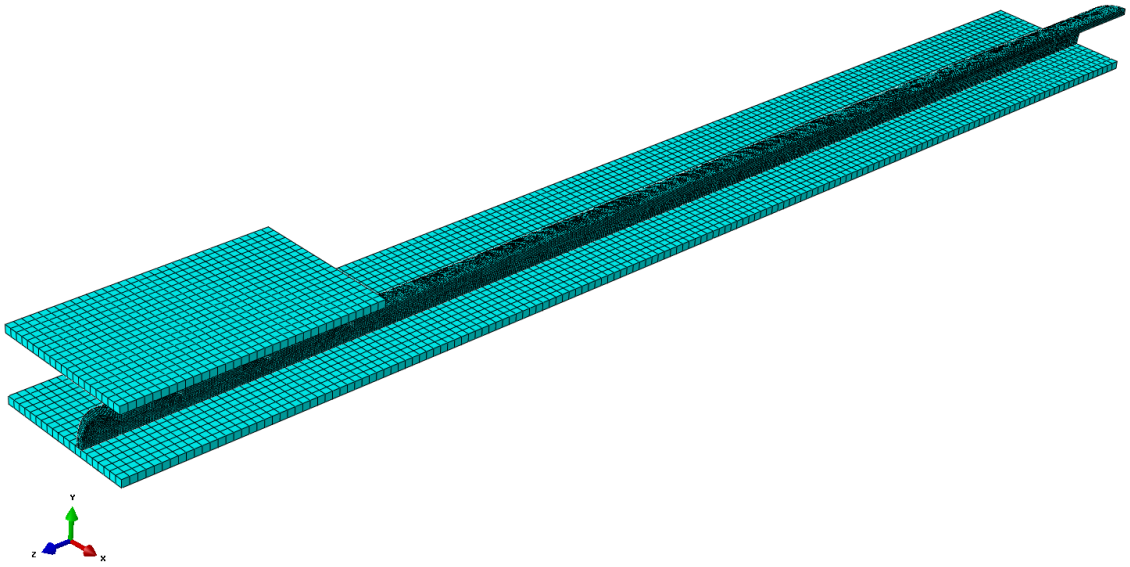

Figure 3-9 Discretized forming setup.

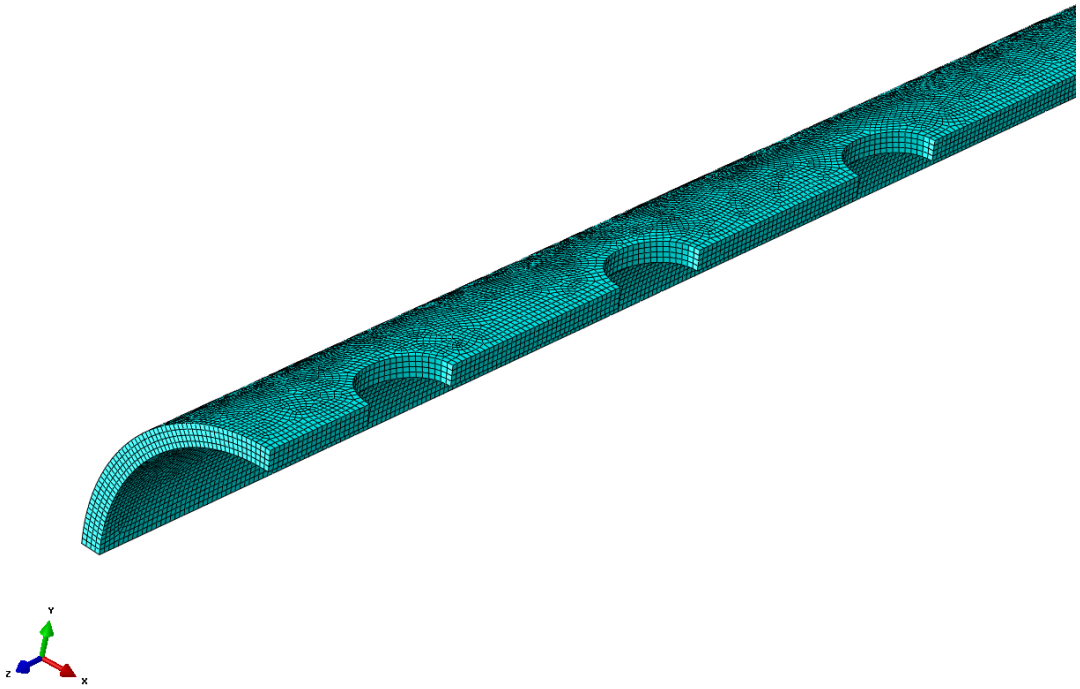

Figure 3-10 Mesh of the tube.

Table 3.4 Hourglass method definition.

ID	**Hourglass control method**
HG-1	Enhanced
HG-2	Relax stiffness
HG-3	Stiffness
HG-4	Combined

3.2.4 Time Integration

To obtain an economical solution time, the tube flattening simulation requires the use of explicit time integration methods introduced previously in chapter 2.4.2. The program calculates automatically the stable time increment sizes based on the Courant-Friedrichs-Lewy condition. A quasi-static response and economical solution time require that a proper time for the flattening simulation must be determined by evaluating a set of different time periods and mass scaling factors. The proposed simulation times and mass scale factors are presented in Table 3.5 and Table 3.6. A smooth ramping is used in the time integration i.e. the load is not applied instantaneously but with a smooth sinusoidal curve. A double output precision is used in the analyses.

Table 3.5 Evaluated time periods.

ID	Time period [s]
TP-1	0.005
TP-2	0.01
TP-3	0.015

Table 3.6 Evaluated mass scaling factors.

ID	Mass scaling factor f^2
MS-1	4
MS-2	9
MS-3	25

3.2.5 Contact Modeling

All the contacts with rigid parts in the model are assumed to yield frictionless tangential behavior. A frictional explicit general contact with coefficient $\mu = 0.2$ is used throughout the model to represent self-contact of the tube. A kinematic contact method with finite sliding is used between the tube and the rigid parts. No additional contact properties are used in the analysis.

3.2.6 Analysis Conditions

The analysis conditions used in the analysis are presented in Figure 3-11. The Table 3.7 indicates whether a condition is created, propagated or being inactive in the current analysis step. The following subchapters explain how the forming process takes place.

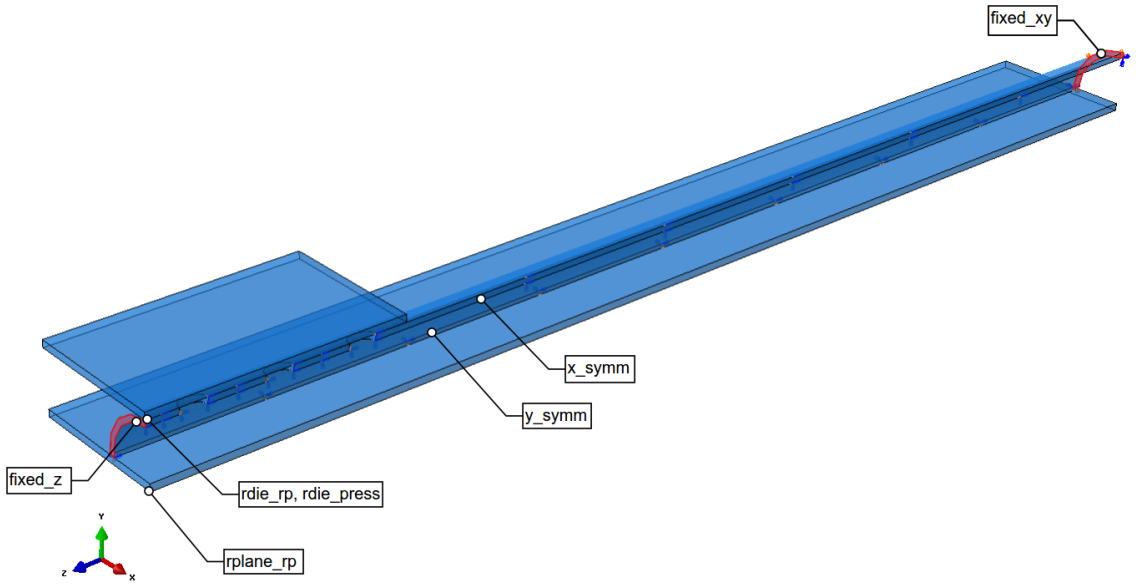

Figure 3-11 Definition of the analysis conditions.

Table 3.7 Analysis Conditions.

Name	Analysis step		Description
	Initial	Step-1	
fixed_xy	Created	Propagated	Cross-section of the tube fixed in the xy-plane.
fixed_z	Created	Propagated	Tube end fixed in the z-direction.
rdie_press		Created	The rigid punch motion in y-direction.
rdie_rp		Created	Fixed nodal support for the rigid die.
rplane_rp		Created	Fixed nodal support for the rigid plane.
x_symm	Created	Propagated	Symmetry condition in x-direction.
y_symm	Created	Propagated	Symmetry condition in y-direction.

3.2.6.1 Initial step

The symmetry condition with respect to YZ-plane is created with the BC *x_symm* and with respect to XZ-plane is created with the BC *y_symm*. The first tube end is fixed in X- and Y-direction with the BC *fixed_xy* to ensure that the cross section remains undeformed and the axial shortening can happen. The second tube end is fixed in only Z-direction with the BC *fixed_z*. These conditions remain unchanged throughout the analysis.

3.2.6.2 Step-1

In the flattening stage, the rigid die squeezes the tube sides together with the *rdie_press*. The total displacement of the die in Y-direction is 34.1 *mm*. The *rdie_rp* and *rplane_rp* are used to prevent motion in any other degree of freedom than the operational direction of the rigid part.

3.2.7 Analysis Parameter Study

The results of the forming simulation are presented in the following chapter. The first goal was to obtain a proper time period for solution to remain quasi-static. This was done by evaluating different time periods in the forming simulation. The second goal was to determine the most economical solution time, by which the solution still gives a quasi-static response. This was done by introducing different mass scaling factors in the analysis. The third goal was to minimize shear locking effects and zero energy modes by finding the most suitable hourglass control method. The rigid parts are excluded from the energy calculations since they do not have any mass.

3.2.8 Time period study

Table 3.8 shows a summary of the analyses with different time periods and an average value of the ratio of the kinetic energy to the internal energy with different time periods. HG-2 was used as an hourglass control method in every analysis. The internal and kinetic energies for different time periods are presented in Figures 3.12-3.14.

Table 3.8 Analysis summary of the time period study using the hourglass control method HG-2.

ID	Total time period [s]	Number of increments	Kinetic energy / Internal energy [%]
TP-1	0.005	66883	4.21
TP-2	0.010	128914	1.06
TP-3	0.015	193367	0.47

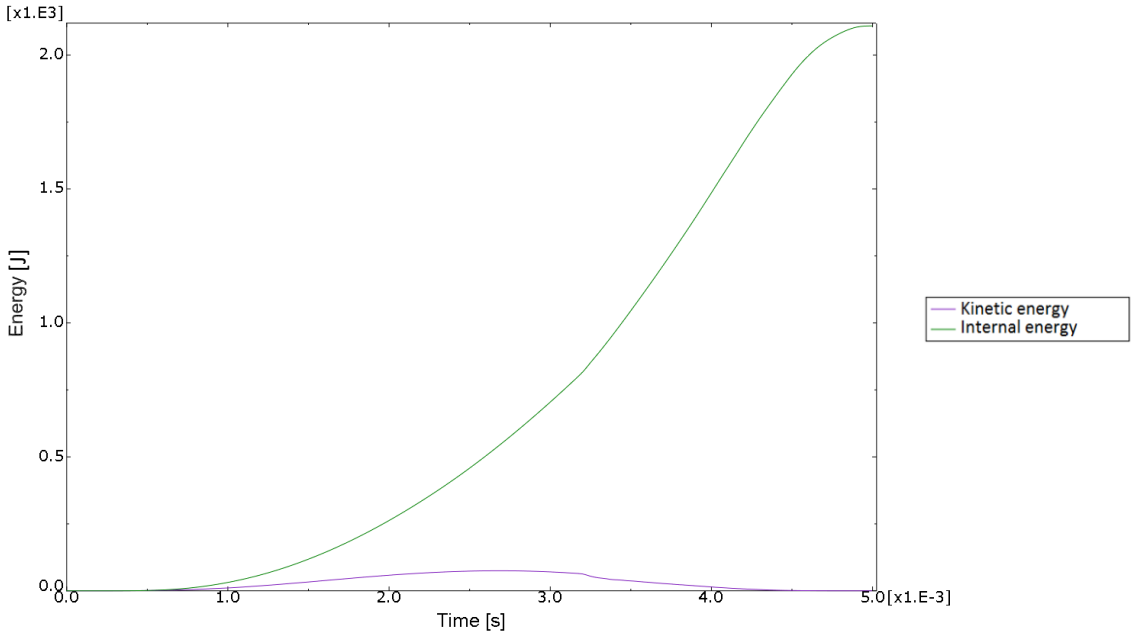

Figure 3-12 Internal and kinetic energy (TP-1).

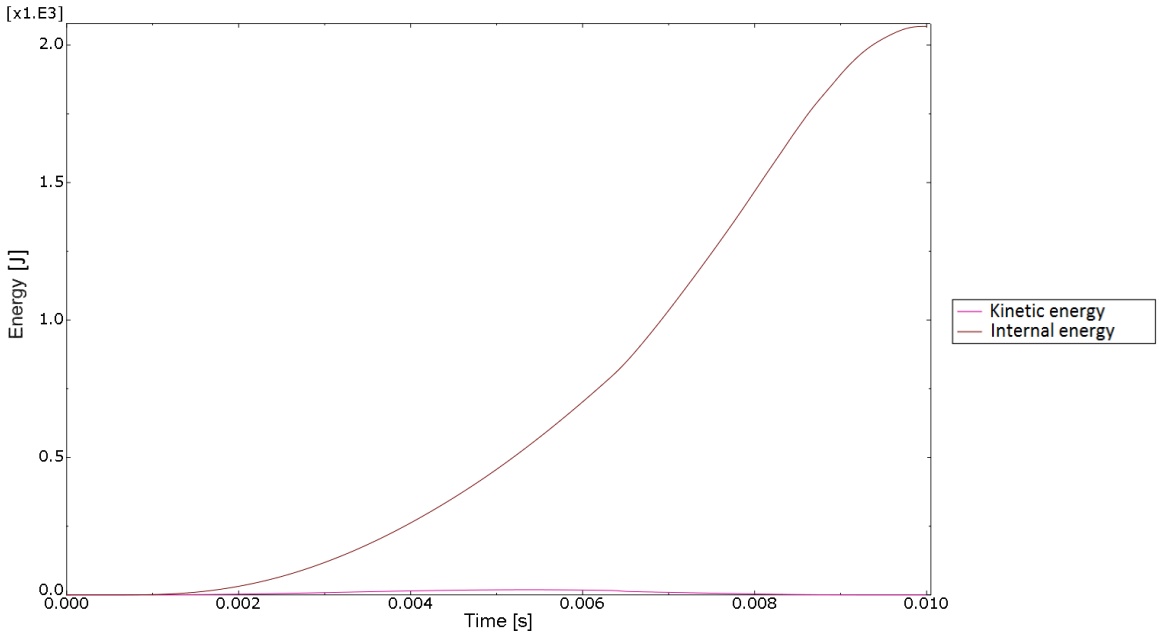

Figure 3-13 Internal and kinetic energy (TP-2).

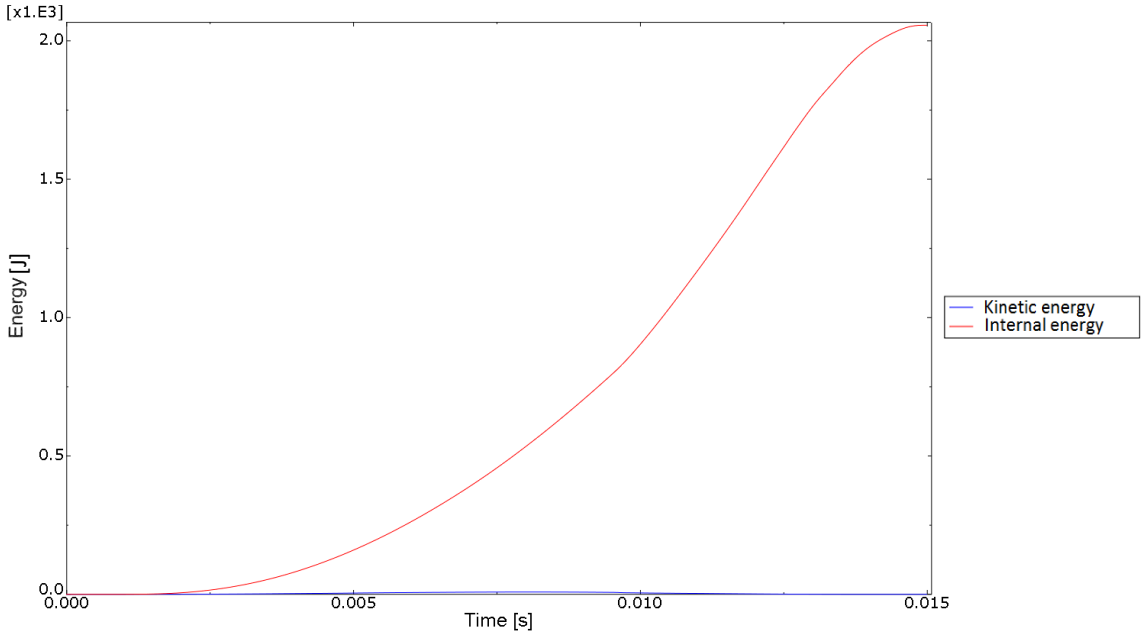

Figure 3-14 Internal and kinetic energy (TP-3).

3.2.8.1 Mass scale factor study

Table 3.9 shows a summary of the analyses with different mass scaling factors and a corresponding average value of the ratio of the kinetic energy to the internal energy. The time period TP-3 and the default hourglass control (relax stiffness) was used in every analysis. The internal and kinetic energies for different mass scale factors are presented in Figures 3.15-3.17. A comparison between the energy ratios is presented in Figure 3-18.

Table 3.9 Analysis summary of the mass scale factor study using the time period TP-3.

ID	Total time period [s]	Number of increments	Kinetic energy / Internal energy [%]
MS-1	0.015	96902	1.88
MS-2	0.015	66886	4.21
MS-3	0.015	40142	11.48

As shown on Table 3.9 all the mass scale factors used increased the amount of kinetic energy excessively and led to falsified results. No mass scaling can be used in this forming simulation.

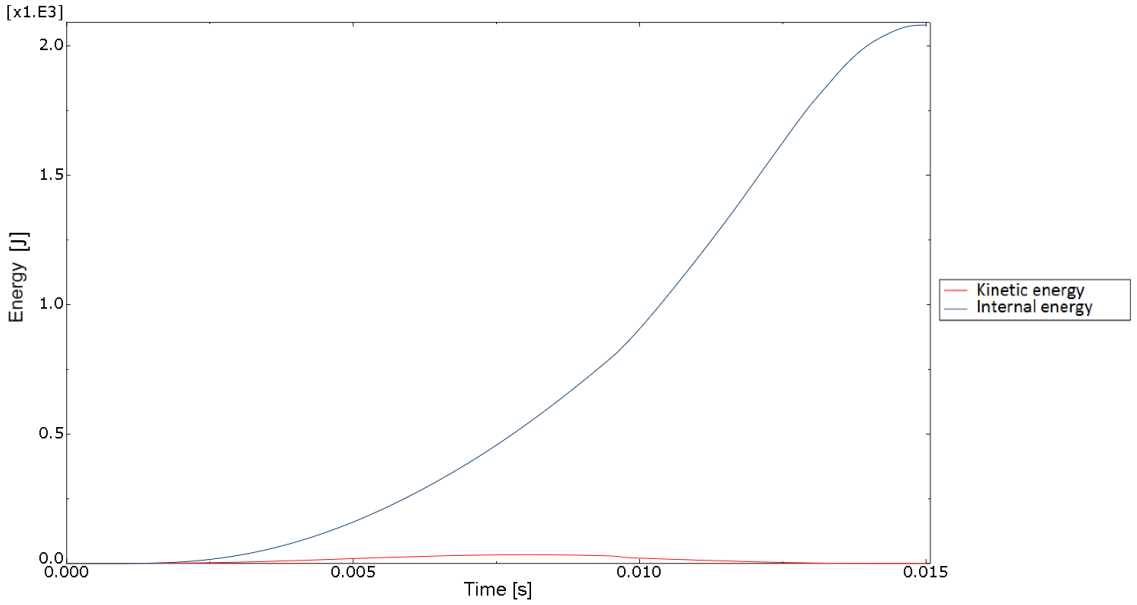

Figure 3-15 Internal and kinetic energy (MS-1).

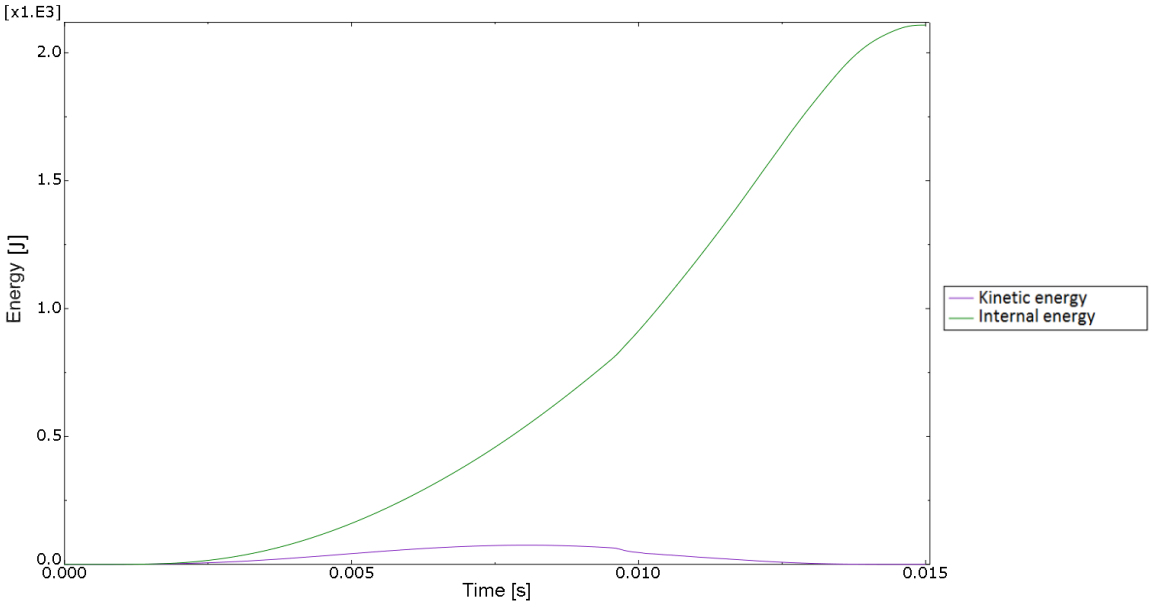

Figure 3-16 Internal and kinetic energy (MS-2).

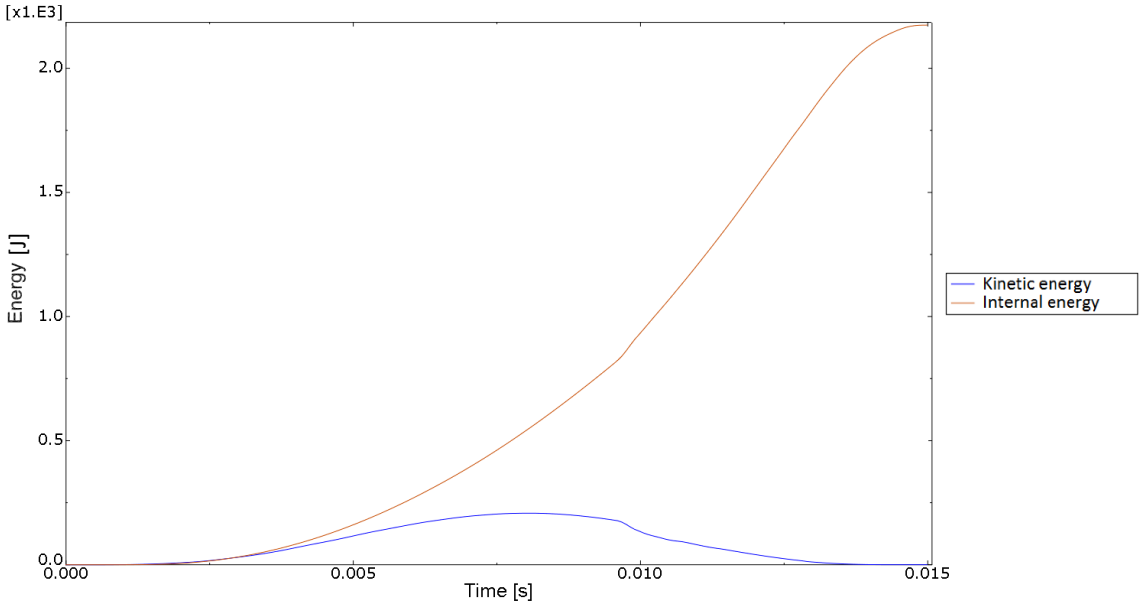

Figure 3-17 Internal and kinetic energy (MS-3).

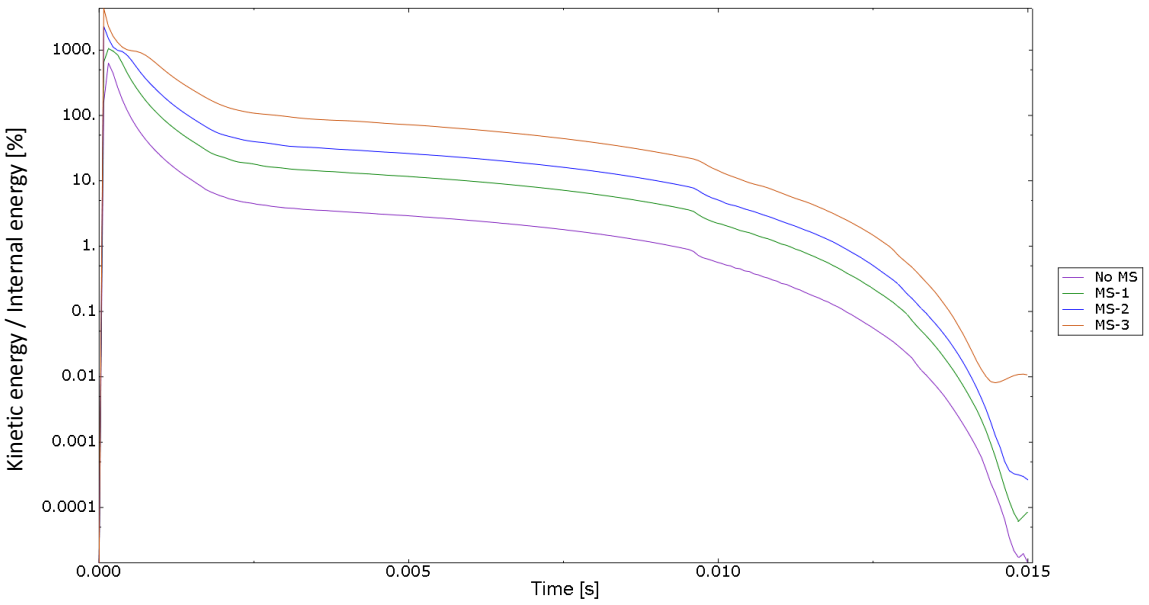

Figure 3-18 Comparison of the ratio of kinetic energy to the internal energy.

3.2.8.2 Hourglass control study

Table 3.10 shows a summary of the analyses with different hourglass controls. The used time period was TP-1. No mass scaling was used in the analyses. The internal and artificial strain energies for different hourglass controls are presented in Figures 3-19 to 3-22. Figure 3-23 shows a comparison of the ratio of the artificial strain energy to the internal energy with different control methods.

Table 3.10 Analysis summary of the hourglass control study.

ID	Time period [s]	Number of increments	Artificial strain energy / Internal energy [%]
HG-1	0.005	67061	25.5
HG-2	0.005	66883	2.52
HG-3	0.005	66885	10.64
HG-4	0.005	67697	5.17

As seen on Table 3.10, the only hourglass control that satisfies the proposed limit value of 5 % [20] is HG-2 (relax stiffness method). The three other control methods led to excessive deformation and severe element distortion. Due to the element distortion, none of these models could converge in the springback part of the analysis.

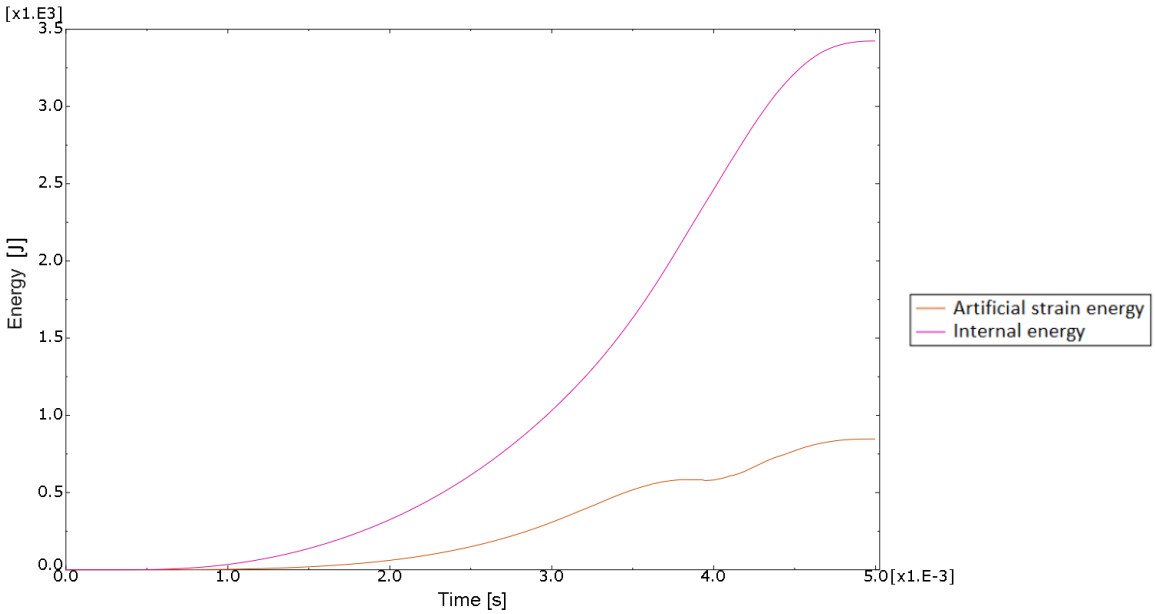

Figure 3-19 Internal and artificial strain energy (HG-1).

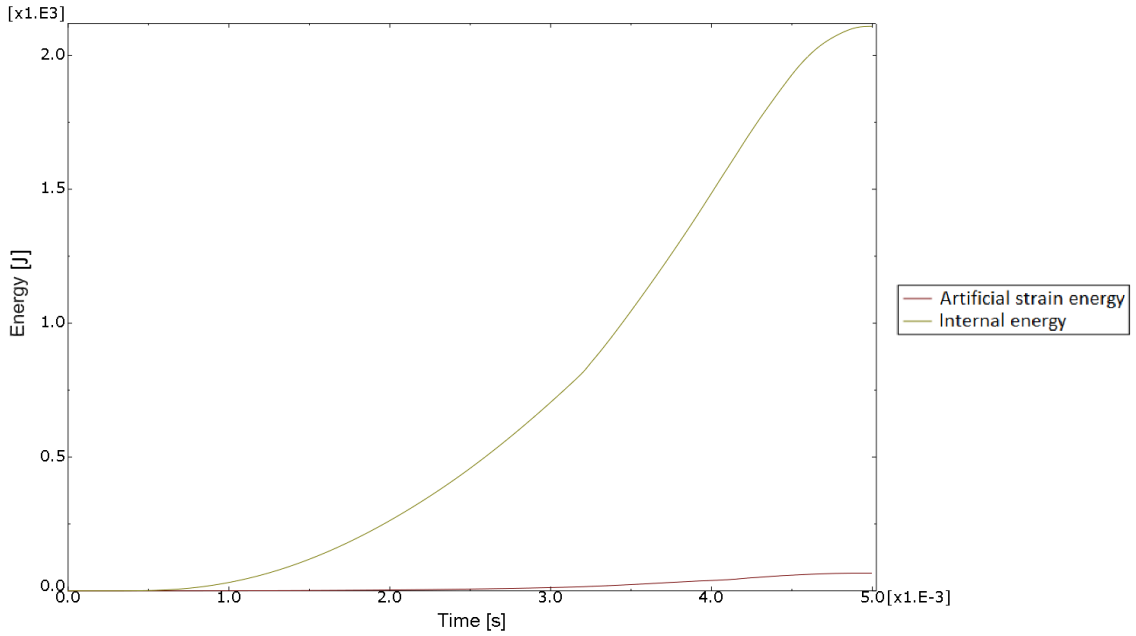

Figure 3-20 Internal and artificial strain energy (HG-2).

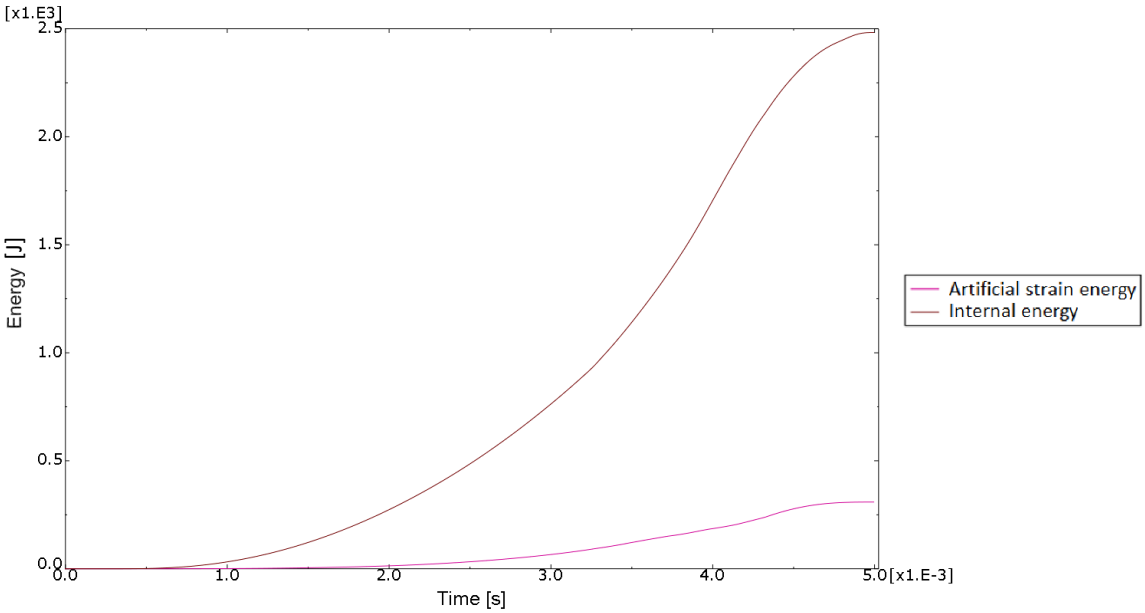

Figure 3-21 Internal and artificial strain energy (HG-3).

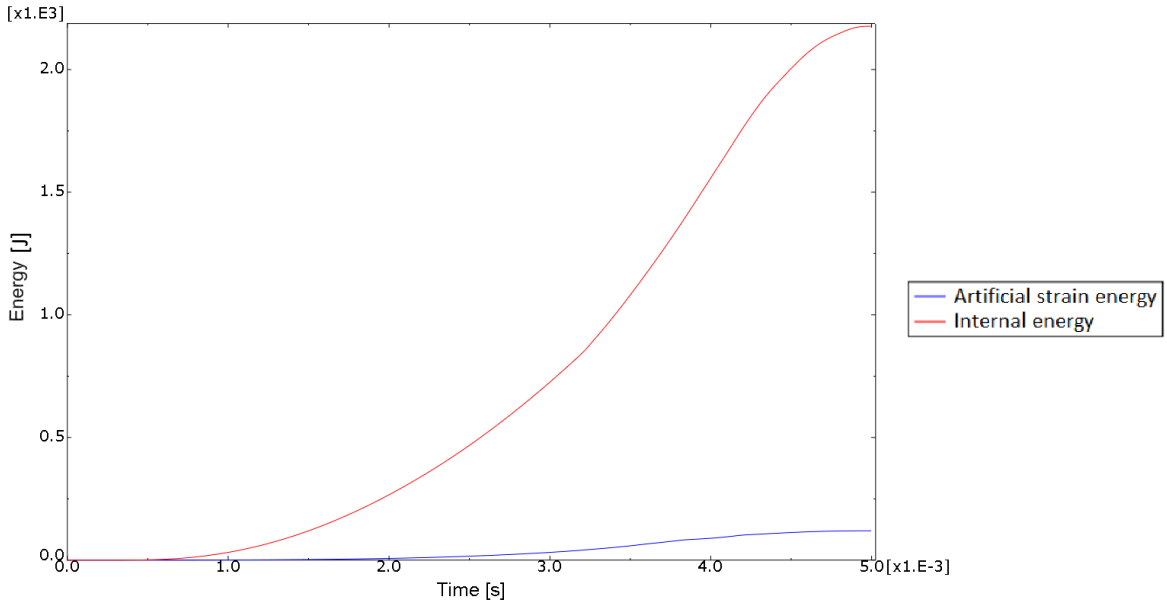

Figure 3-22 Internal and artificial strain energy (HG-4).

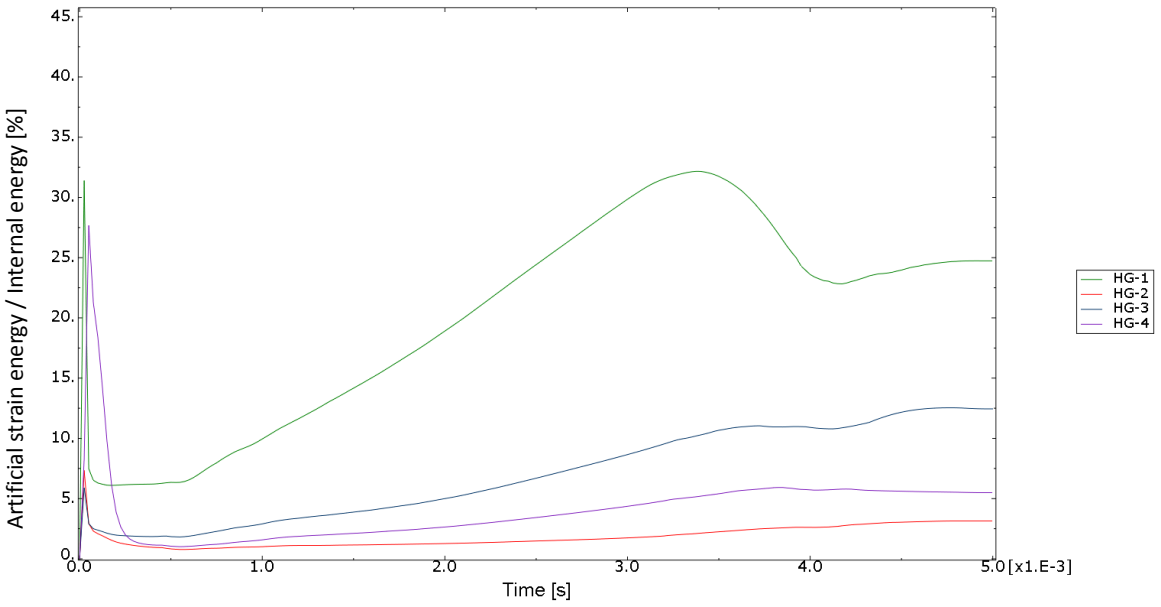

Figure 3-23 Comparison of the ratio of artificial strain energy to the internal energy.

3.2.9 Results of Part I

Table 3.11 shows a summary of the analysis. The energy summary is presented in Figure 3-24. In a proper quasi-static simulation, the ratio of internal energy to the external work should be close to 100 %. Due to the self-contact, a small amount of external work is dissipated through friction.

Table 3.11 Analysis summary of part I.

Total time [s]	0.015
Number of increments [-]	193367
Kinetic energy / Internal energy [%]	0.47
Artificial strain energy / Internal energy [%]	2.44
Internal energy / External work [%]	98.35

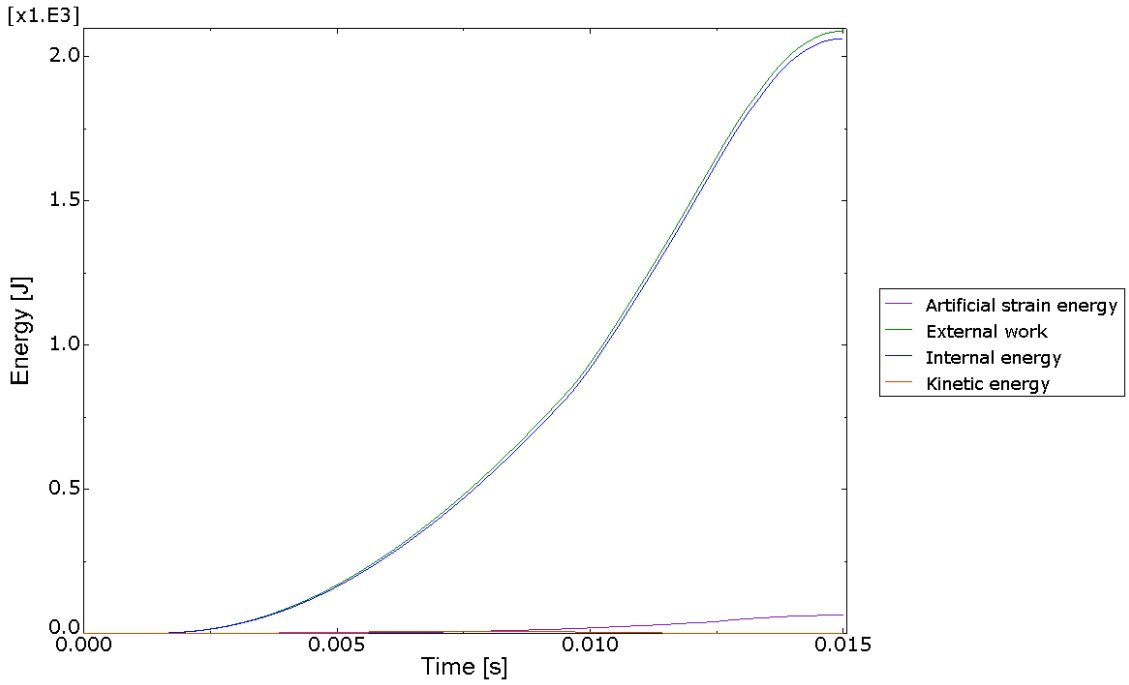

Figure 3-24 Energy summary of the forming analysis.

In the following subchapters, the results are presented with geometry of a full model to give a more illustrative presentation.

3.2.9.1 *Evolution of the plastic mechanism*

During the flattening process, the tube undergoes high plastic deformation and a plastic mechanism is formed. The evolution of the plastic mechanism in XY-plane is shown in Figure 3-25. The first set of plastic hinges appears on the die contact area as shown in Figure 3-26. As the flattening continues, a second set of plastic hinges appears on the tube sides as presented in Figure 3-27.

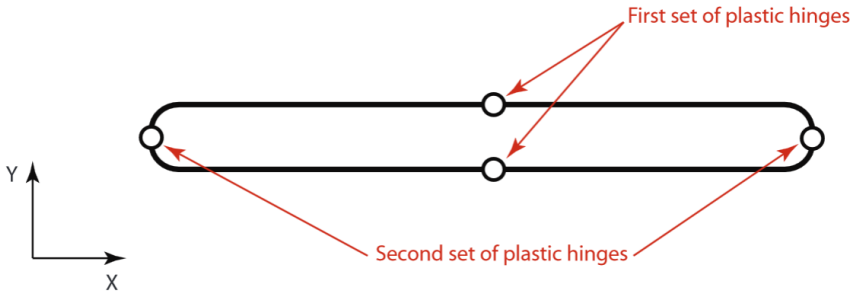

Figure 3-25 Evolution of the plastic mechanism in XY-plane.

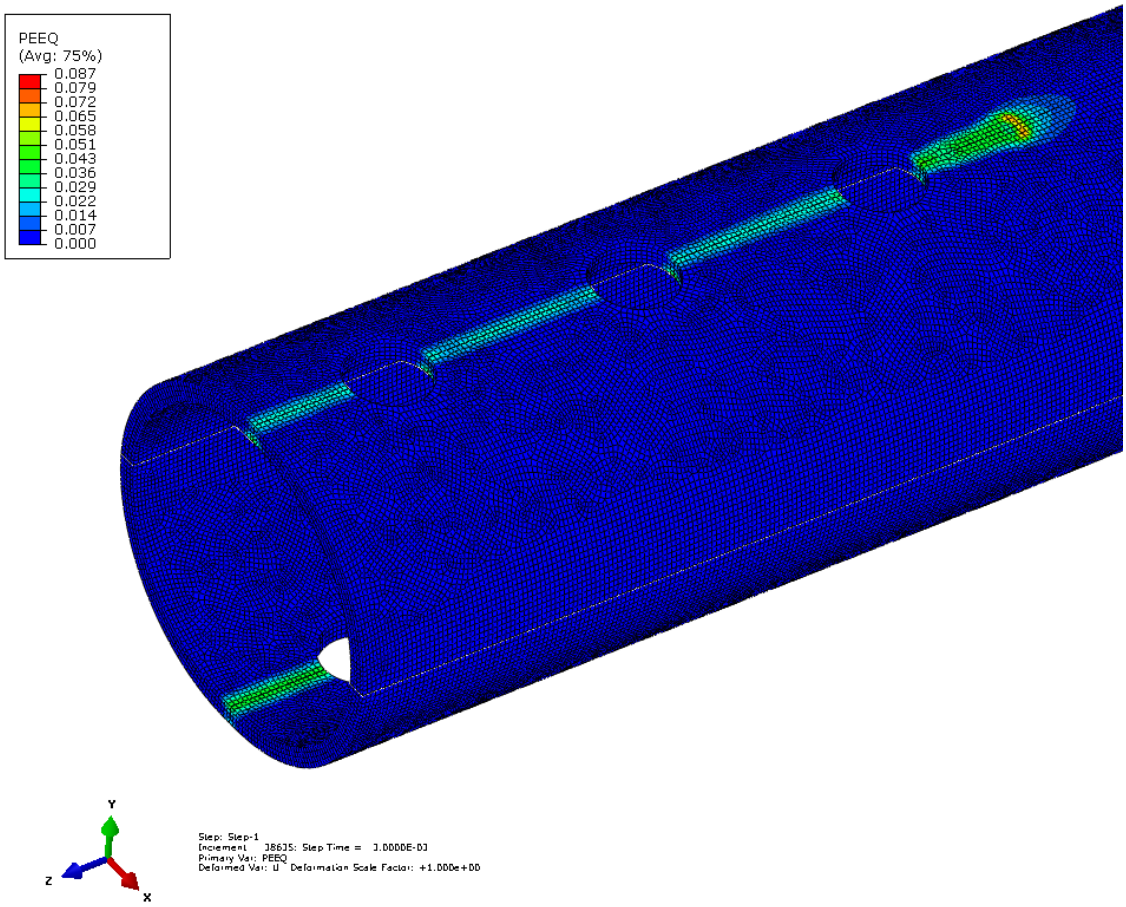

Figure 3-26 First set of plastic hinges on the analysis time t=0.003s.

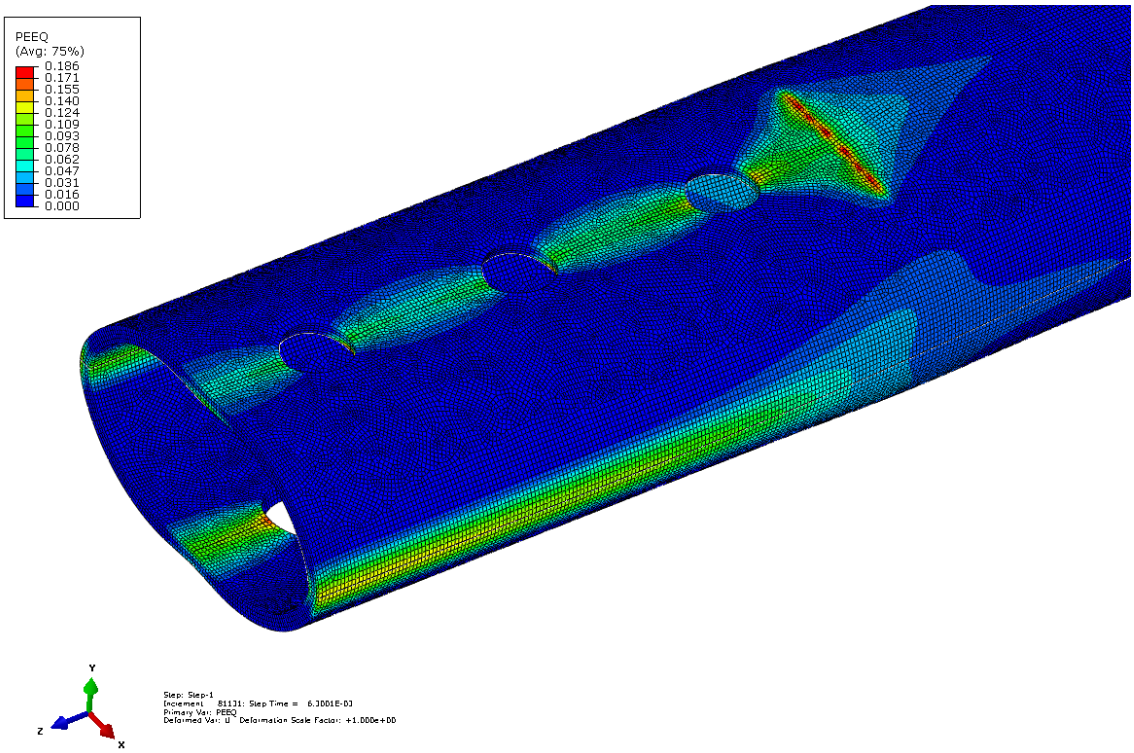

Figure 3-27 Second set of plastic hinges on the analysis time t=0.063s.

After the plastic mechanism is fully developed in XY-plane, the third set of plastic hinges (Figure 3-28) starts to form in YZ-plane as can be already seen in Figure 3-27. The final stage in the end of the analysis is shown in Figure 3-29.

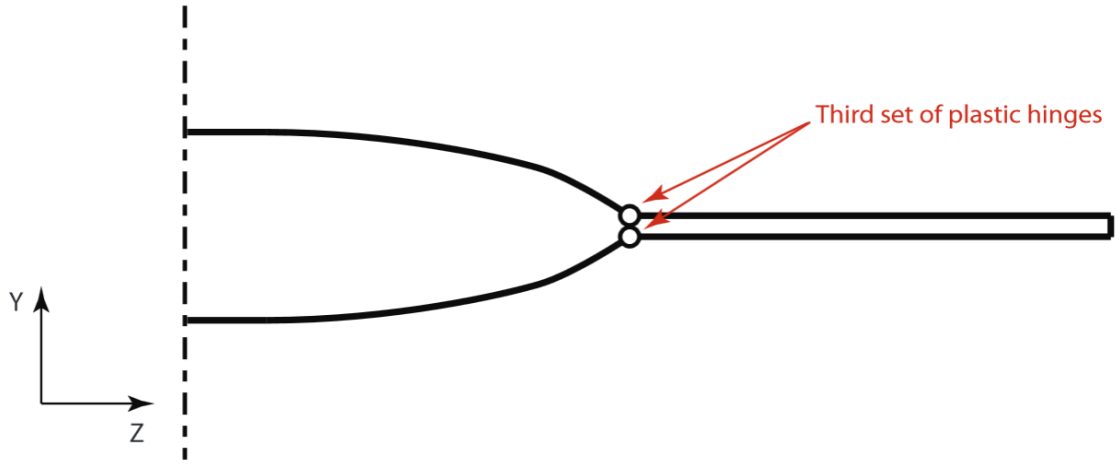

Figure 3-28 The plastic mechanism in YZ-plane.

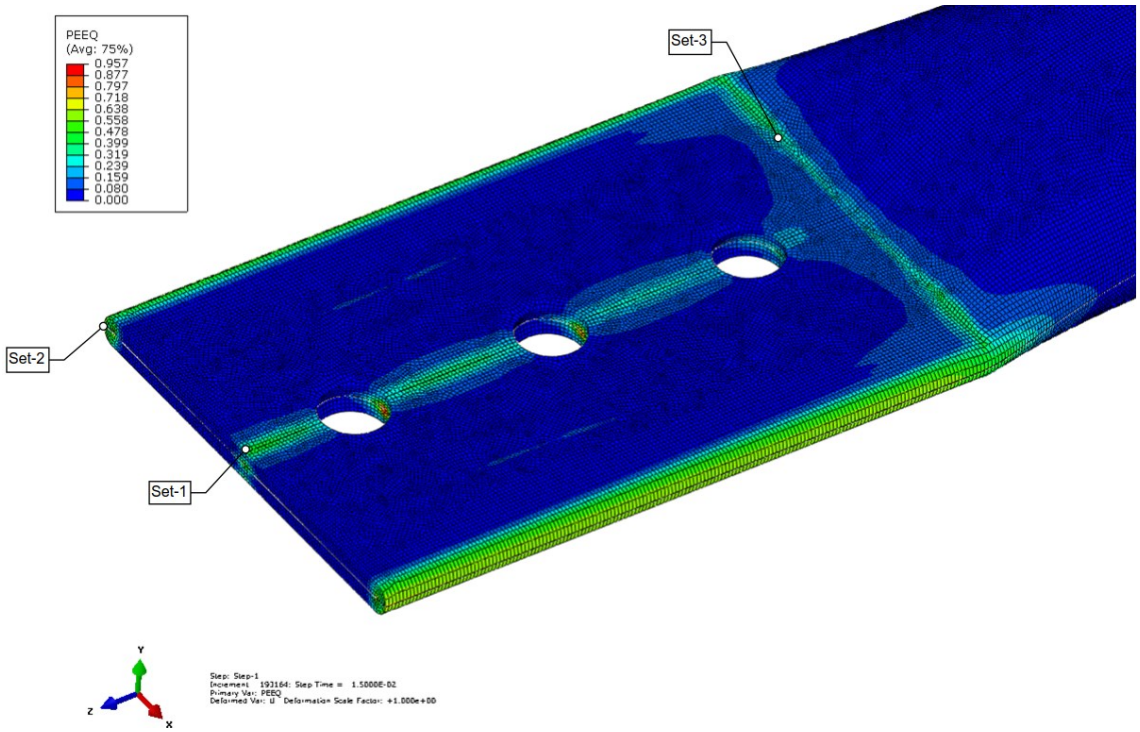

Figure 3-29 The equivalent plastic strains at the end of the analysis.

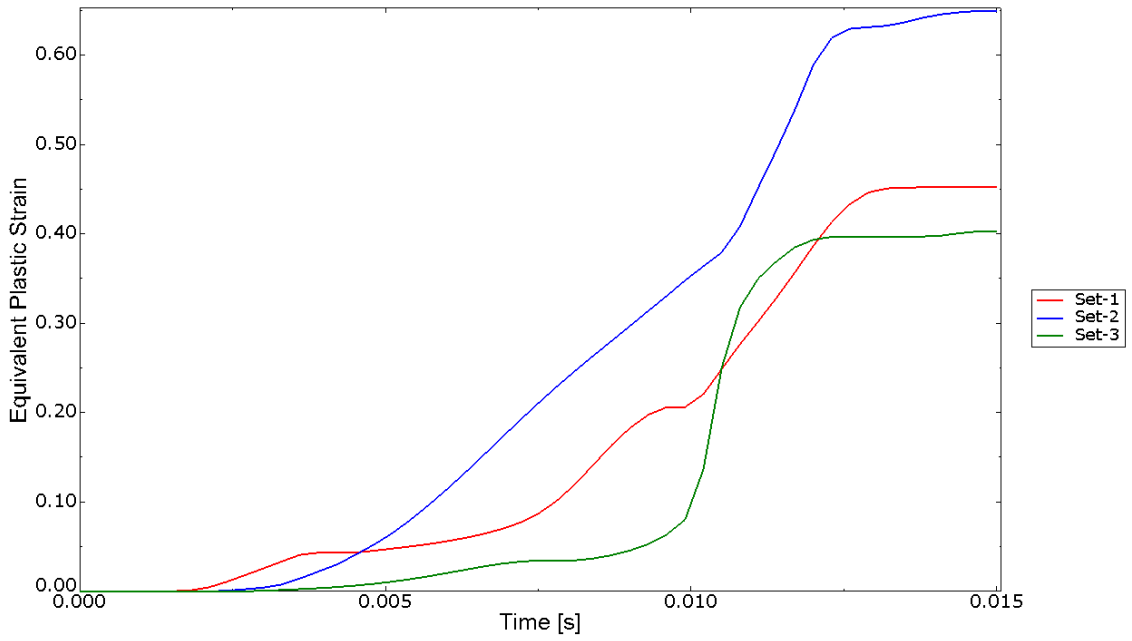

Figure 3-30 shows the equivalent plastic strains with respect to the analysis time. The total equivalent plastic strain is equivalent to von Mises -stress and is defined in a material point at the analysis time t by [17]:

$$\bar{\varepsilon}^{pl} = \bar{\varepsilon}^{pl}|_0 + \int_0^t \sqrt{\frac{2}{3}\dot{\varepsilon}^{pl}:\dot{\varepsilon}^{pl}}\,dt \tag{3.2}$$

where

$\bar{\varepsilon}^{pl}|_0$ is the initial equivalent plastic strain

$\dot{\varepsilon}^{pl}$ is the plastic strain matrix

A node on the top surface on each set of plastic hinge line is selected to illustrate the evolution of the plastic mechanism.

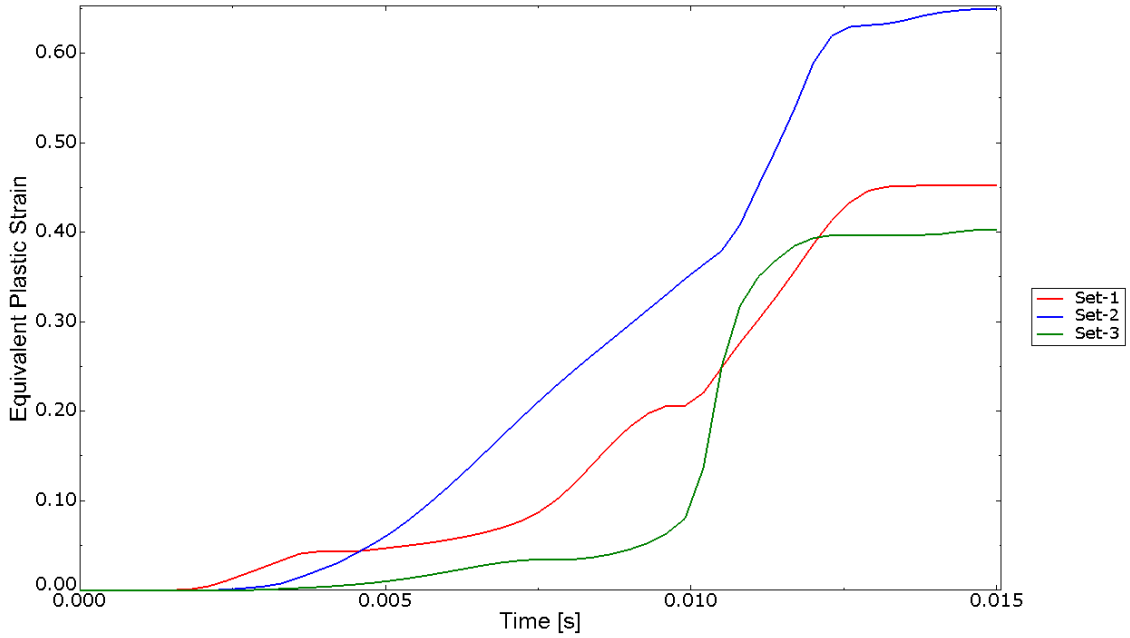

Figure 3-30 Equivalent plastic strains as a function of the analysis time.

3.2.9.2 Equivalent von Mises stresses

The equivalent von Mises stresses in the end of the analysis for the whole tube are presented in Figure 3-31. It can be seen that the stresses resulting from the flattening extend over the midpoint of the member but the fixed end remains free from stresses.

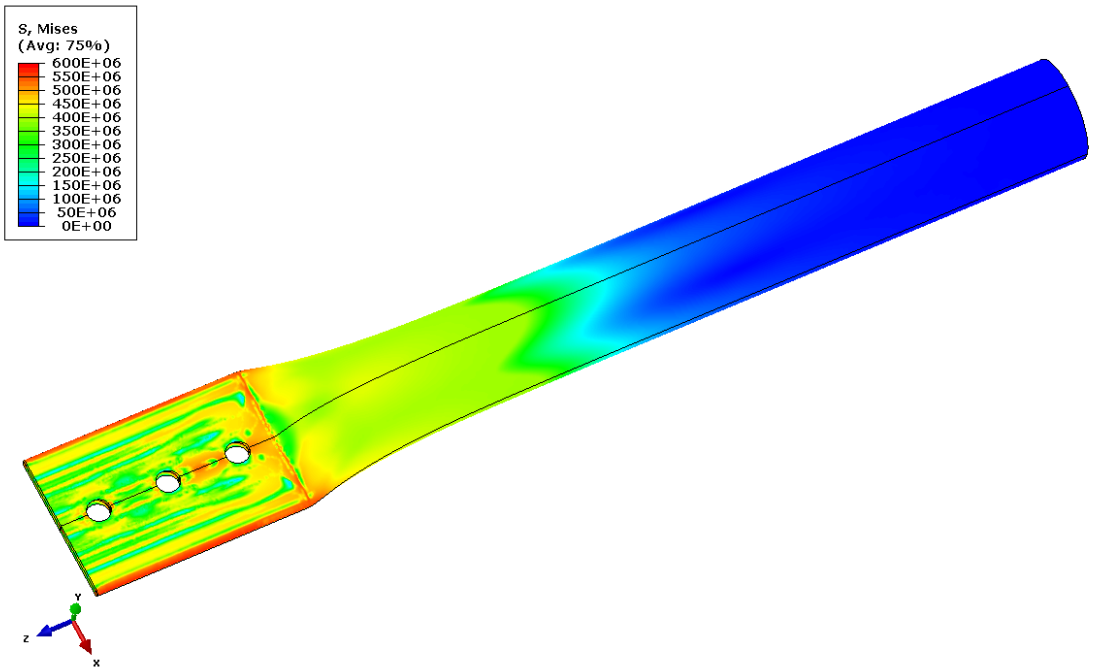

Figure 3-31 The equivalent von Mises stresses in the tube.

A closeup for the equivalent stresses in the flattened region is shown in Figure 3-32. The stresses in the areas near the bolt holes are not completely valid since the bolt holes would not be drilled prior to the flattening but after the springback. The hole drilling would relieve the residual stresses; for now small concentrations appear on the edge areas. Since the simulation of the hole drilling was not within the scope of this thesis, a shortcut is taken. Eventually this matter does not play an important role as can be seen in the following chapters.

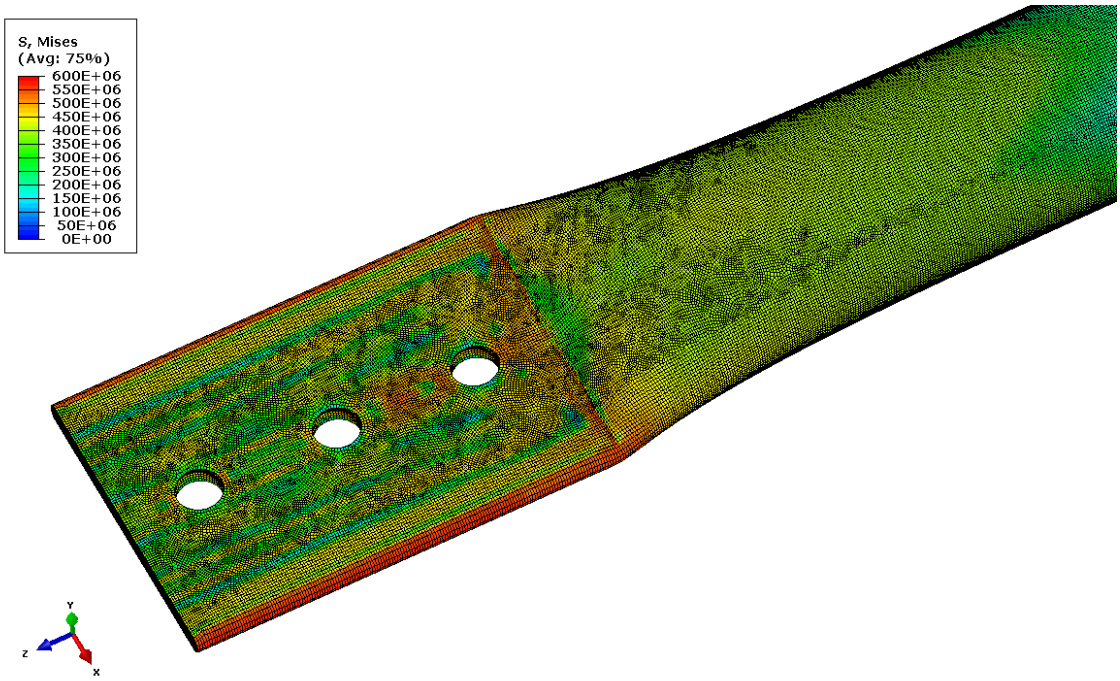

Figure 3-32 The equivalent von Mises stresses in the flattened region.

3.2.9.3 Tool response

The punch die load as a function of the displacement is presented in Figure 3-33. Towards the end of the analysis, the required punching force increases exponentially; the maximum punching force being 1.83 MN. The overall structural response is rather smooth with only small jumps in the curve.

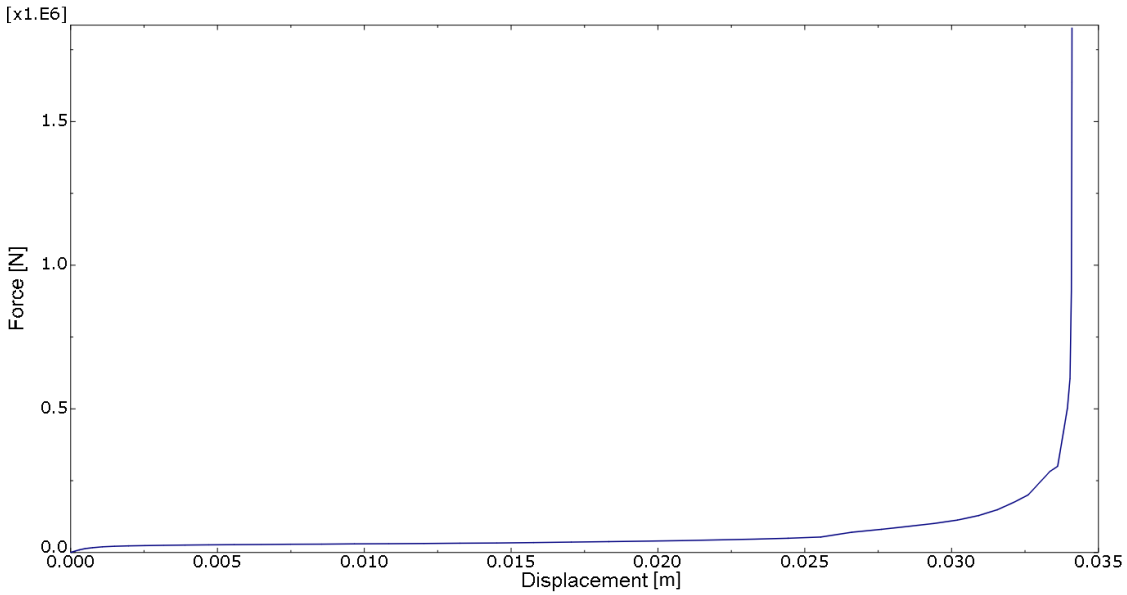

Figure 3-33 The punch die load as a function of the displacement.

3.2.10 Remarks on Part I

The first part of the analysis covered the forming simulation of the tube. Different time periods, mass scaling factors and hourglass controls were evaluated. The parameter study revealed that the appropriate time period for this forming problem is TP-3 where the time period size for the forming is $0.015\ s$. The total amount of kinetic energy in the analysis was 0.47 %, which is less than the proposed limit value of 1 % [20].

The mass scaling study showed that no mass scaling can be used with the applied time period TP-3, since the amount of kinetic energy exceeds the limit value in every case studied.

The hourglass control study showed that the only the relax stiffness method (HG-2) can be used with this problem since the total amount of artificial strain energy exceeds the proposed limit value of 5 % [20] in every other case.

3.3 Part II – Springback

This chapter examines the magnitude of springback and final residual stress distribution of the tube. First, the analysis parameters are redefined to match the current analysis setup. Next, the residual stresses and plastic strains from the part one analysis are imported as an initial state variable. Finally, the final shape of the tube and residual stress distribution is obtained to be used in part three analysis.

3.3.1 Redefined Parameters for Part II

First, the model from the part one is copied and the rigid die is removed from the assembly. Next, the explicit analysis step is replaced with an implicit static step and time stepping is redefined. Full Newton method is used as a numerical solving technique. The contacts are replaced with implicit surface to surface contacts which have same tangential behavior as in part one. The analysis conditions are redefined by simply supporting the tube ends so that the elastic strain reversion can take place. The redefined analysis conditions are presented in Figure 3-34. Finally, a predefined field is created where deformed geometry and the stress and strain states of the tube are imported from last step of the part one analysis.

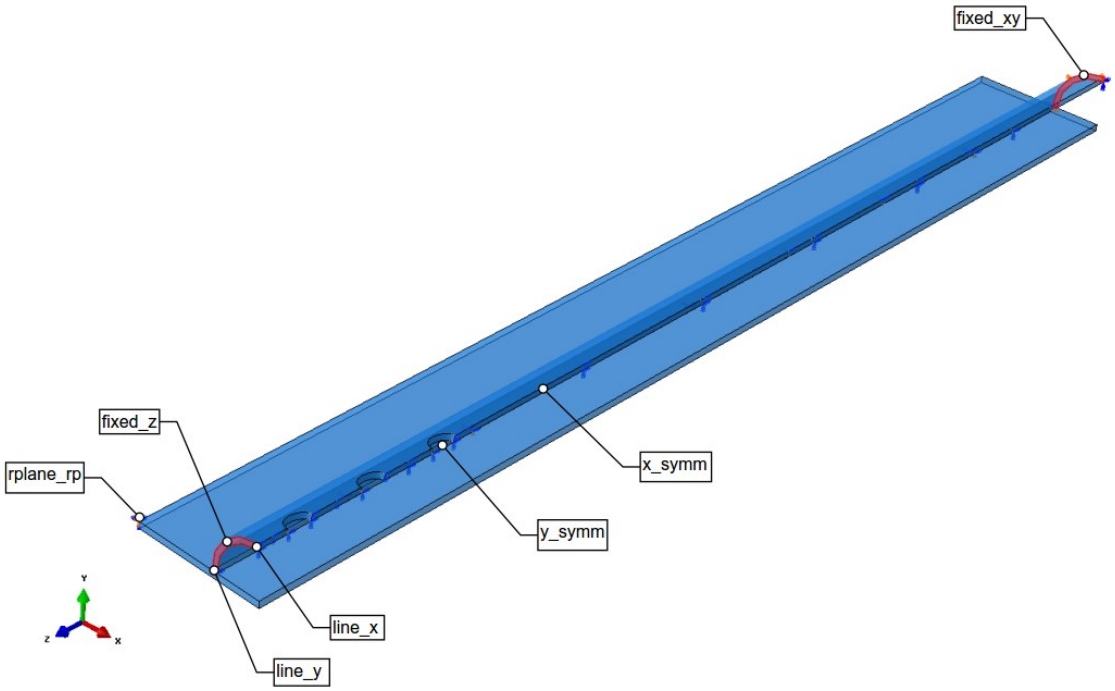

Figure 3-34 Redefined analysis conditions.

3.3.2 Results of Part II

The following subchapters evaluate the shape change of the tube during the springback step and the final residual stress distribution. Table 3.12 shows a summary of the analysis. The energy summary is presented in Figure 3-35. The energy summary shows that no stabilization was needed in the analysis and the internal energy is close to the strain energy. A small amount of energy is dissipated due to plasticization.

Table 3.12 Analysis summary of part II.

Total time [s]	1
Number of increments [-]	5
Artificial strain energy / Internal energy [%]	0.23
Static stabilization energy / Internal energy [%]	0.00
Strain energy / Internal energy [%]	99.42

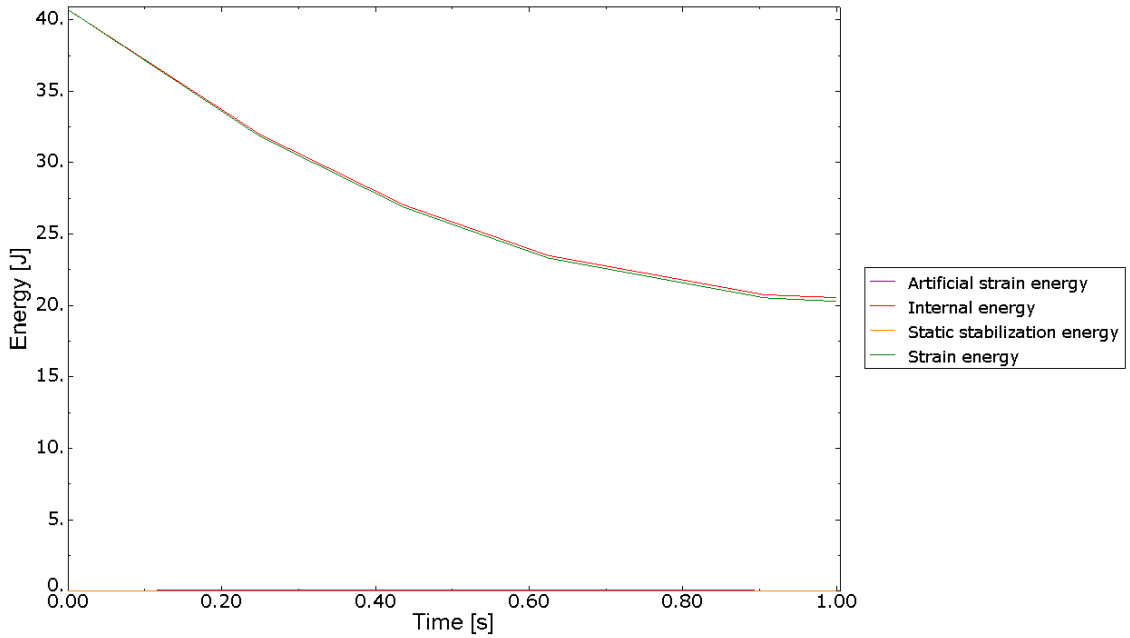

Figure 3-35 Energy summary of the springback analysis.

3.3.2.1 Shape change

Figure 3-36 shows the magnitude of the springback in the whole model. It can be observed that the major part of the elastic strain reversion mainly takes place near the transition zone. A close-up from the transition zone is shown in Figure 3-37. Figure 3-38 shows both the deformed and the undeformed shape overlapped.

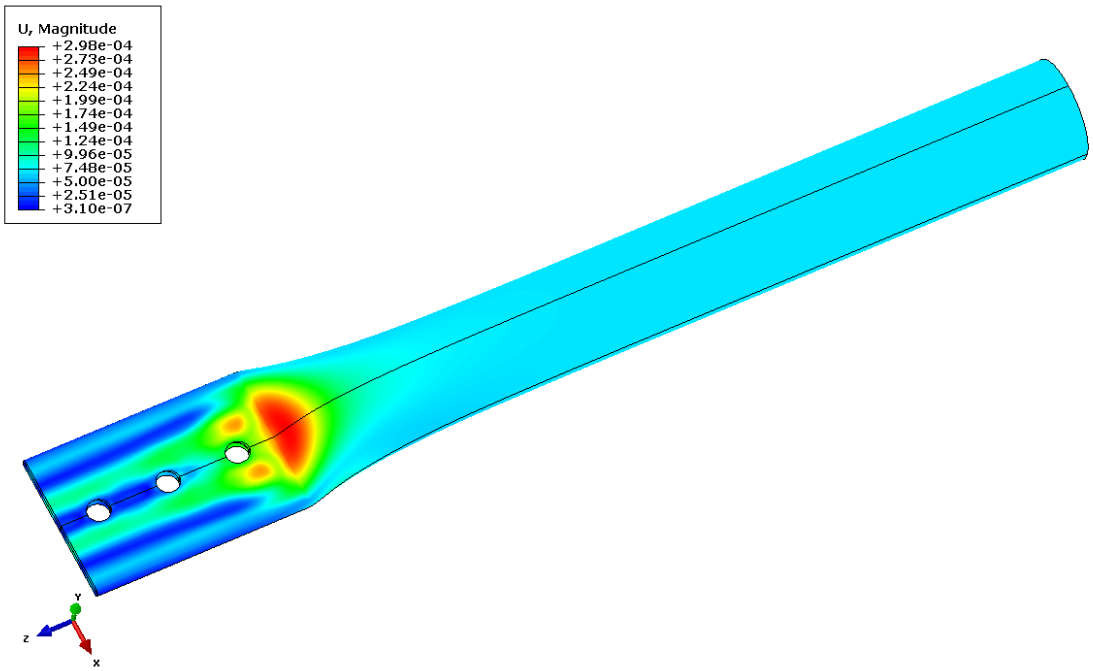

Figure 3-36 Magnitude of the springback in the whole tube.

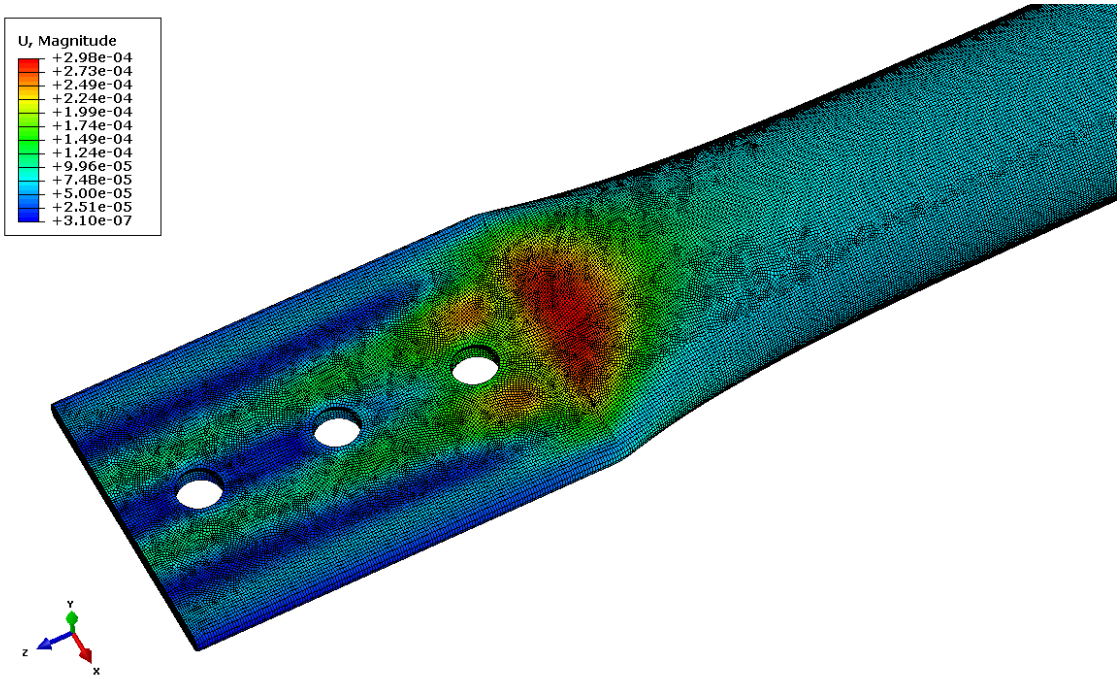

Figure 3-37 Magnitude of the springback in the transition region.

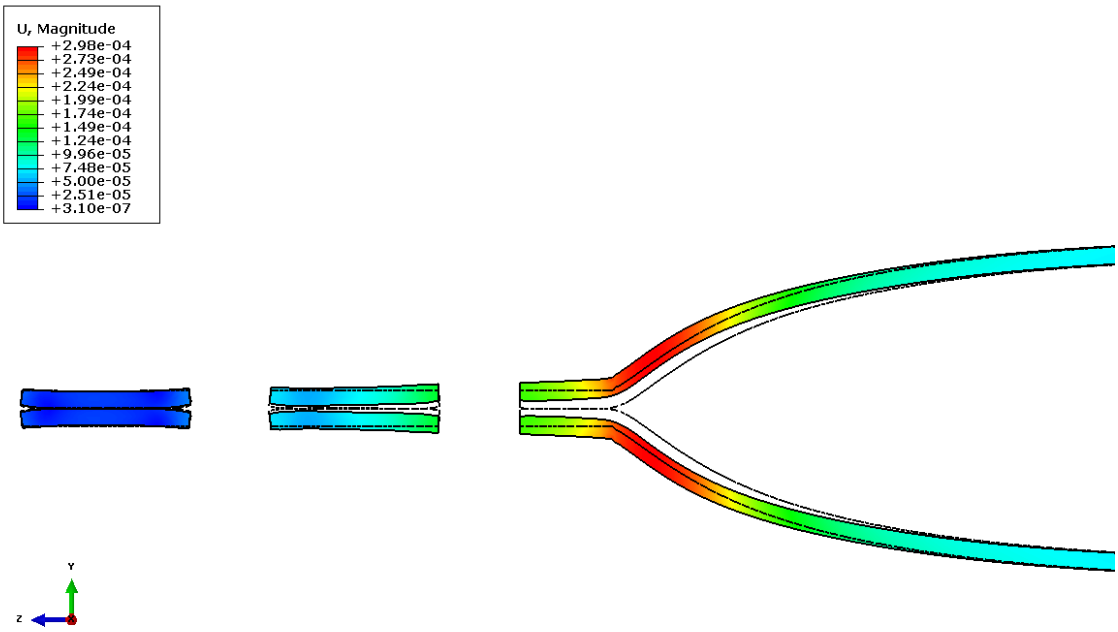

(a) Shape change in the longitudinal section

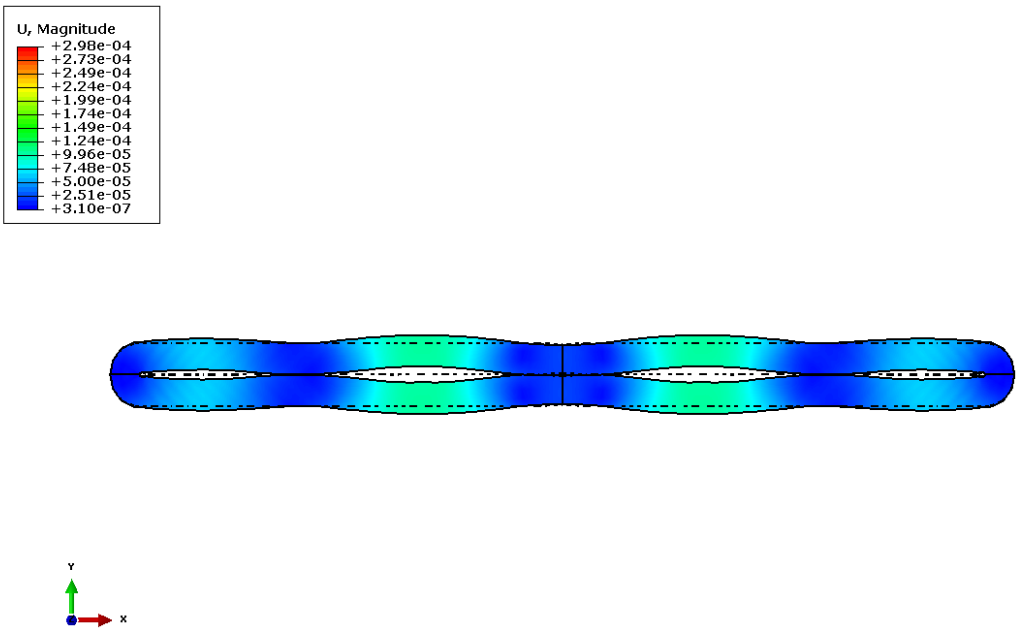

(b) Shape change in the transverse section

Figure 3-38 Shape change due to the springback (deformation scale = 10).

3.3.2.2 Stress states before and after the springback

The stress states of the whole tube are shown in Figure 3-39 and those for the flattened region in Figure 3-40. A significant decrease in the stresses can be observed when the final stress distribution is compared to the stress distribution prior to the springback. This implies that the springback plays a significant role for the bearing capacity of the tube and should be considered later on in the part three.

The maximum absolute values of the principal stress are shown for the whole tube and for the flattened region, respectively, in Figure 3-41 and Figure 3-42. The principal stress directions for the flattened region are shown in Figure 3-43. Figure 3-44 shows components of the stress vectors in Figure 3-43. The center area in the transition zone is in compression where tensile stresses dominate the corner areas propagating towards the center area in the circular end of the transition zone. The large tensile stresses in the stiffer corner areas propose that the residual stresses are favorable when the tube is subjected to compression.

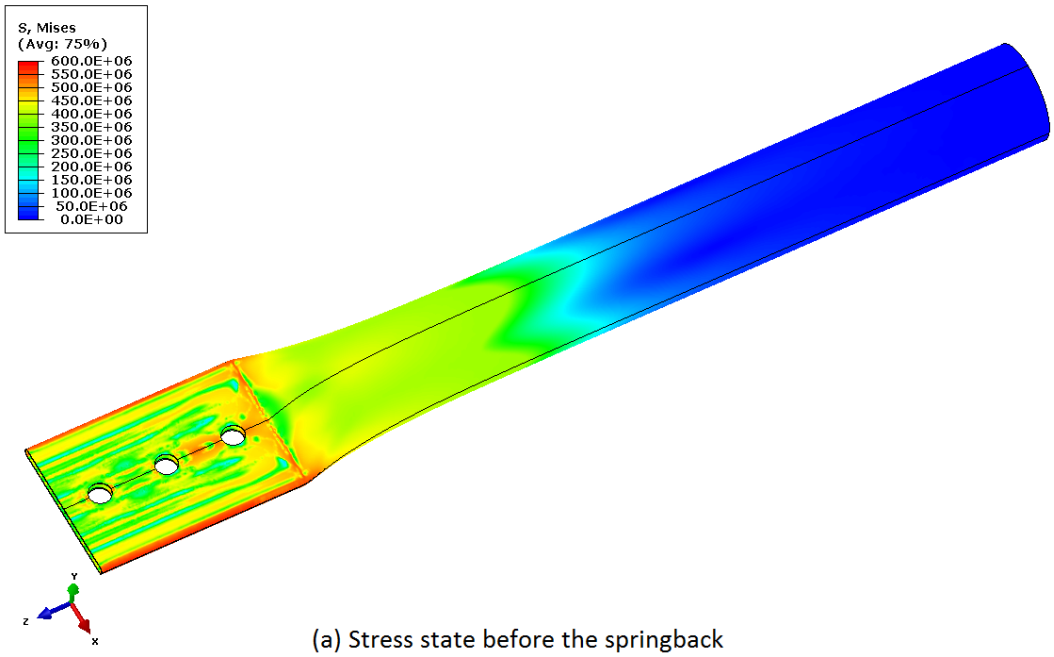

(a) Stress state before the springback

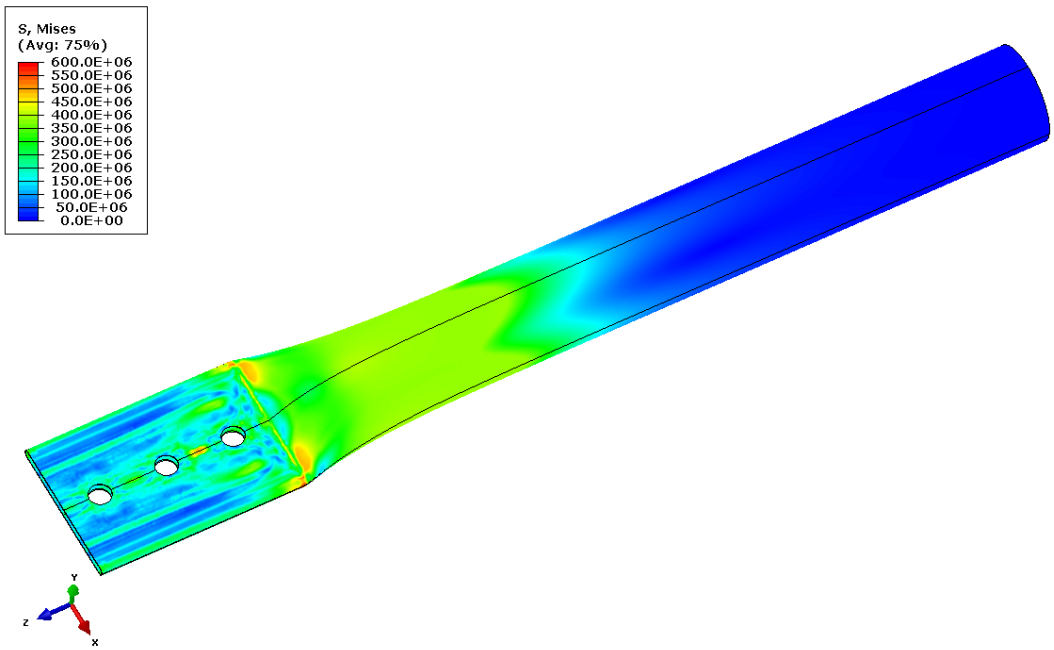

(b) Stress state after the springback

Figure 3-39 Final residual stress distribution in the whole tube.

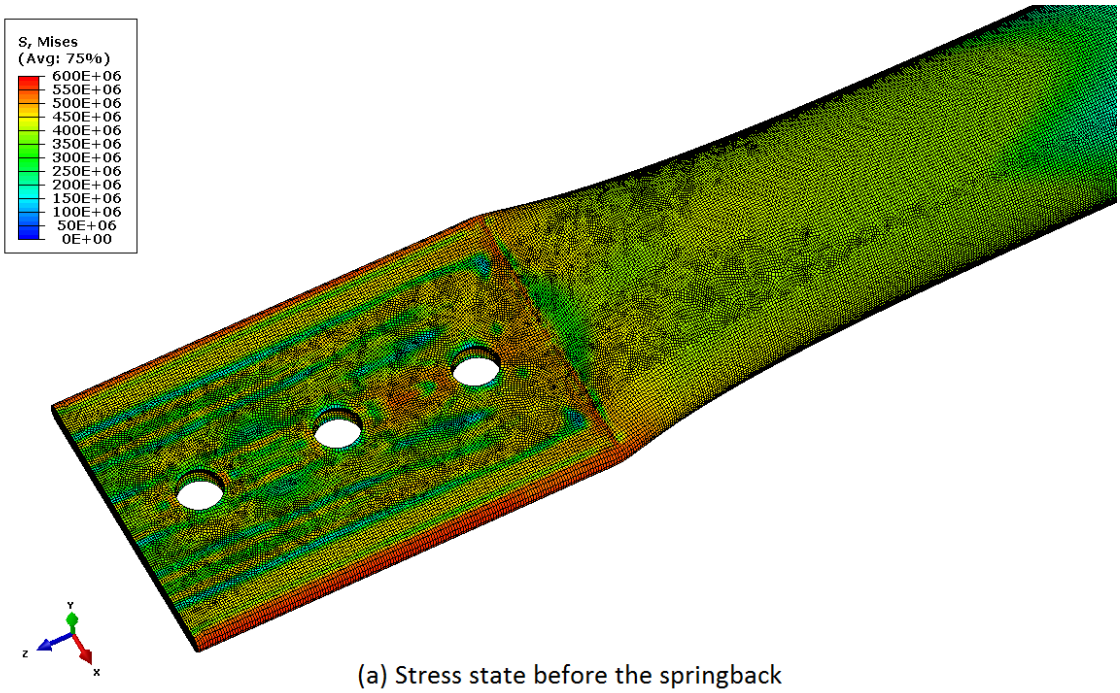

(a) Stress state before the springback

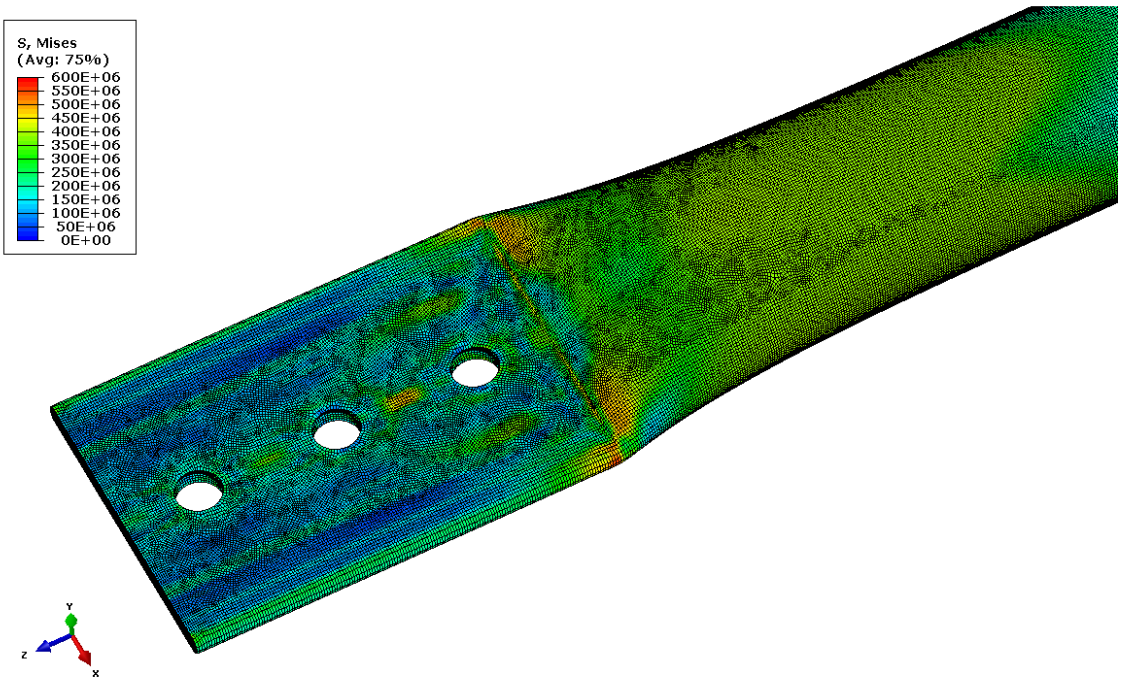

(b) Stress state after the springback

Figure 3-40 Equivalent von Mises stresses in the flattened region.

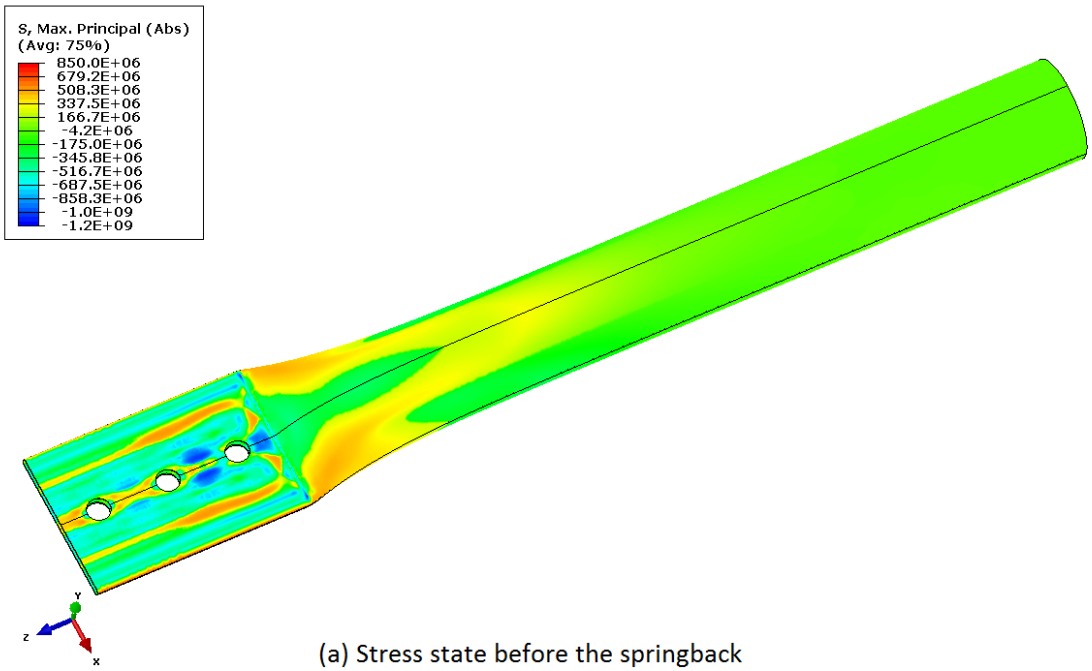

(a) Stress state before the springback

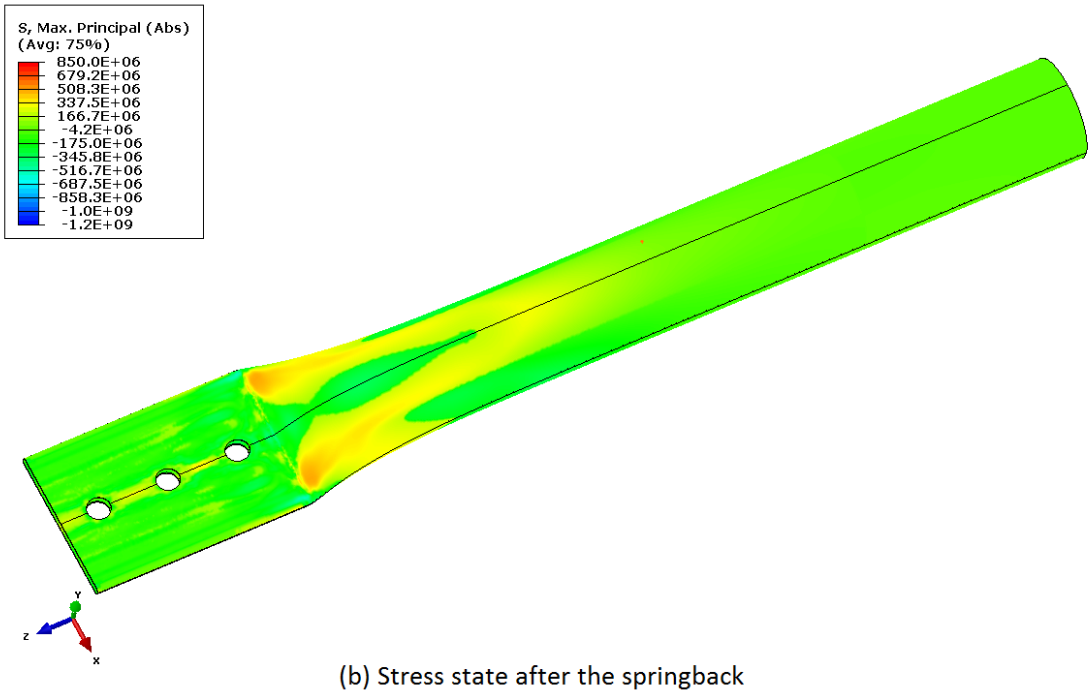

(b) Stress state after the springback

Figure 3-41 Maximum absolute principal stress values on surfaces of the whole tube.

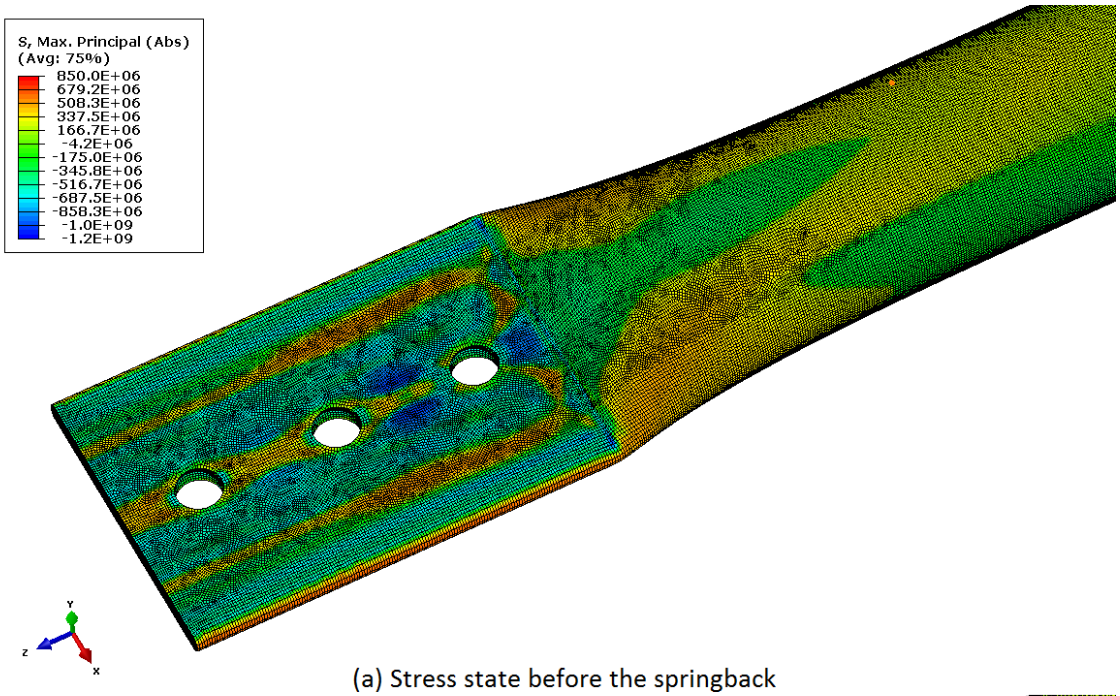

(a) Stress state before the springback

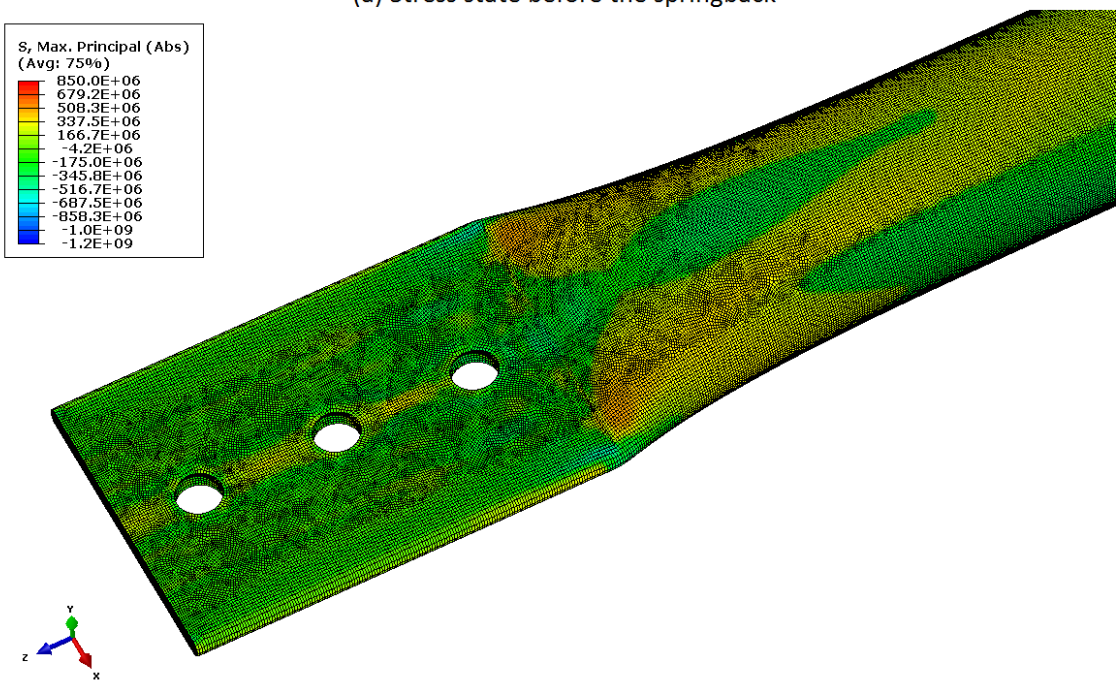

(b) Stress state after the springback

Figure 3-42 Maximum absolute principal stress values on surfaces of the flattened region.

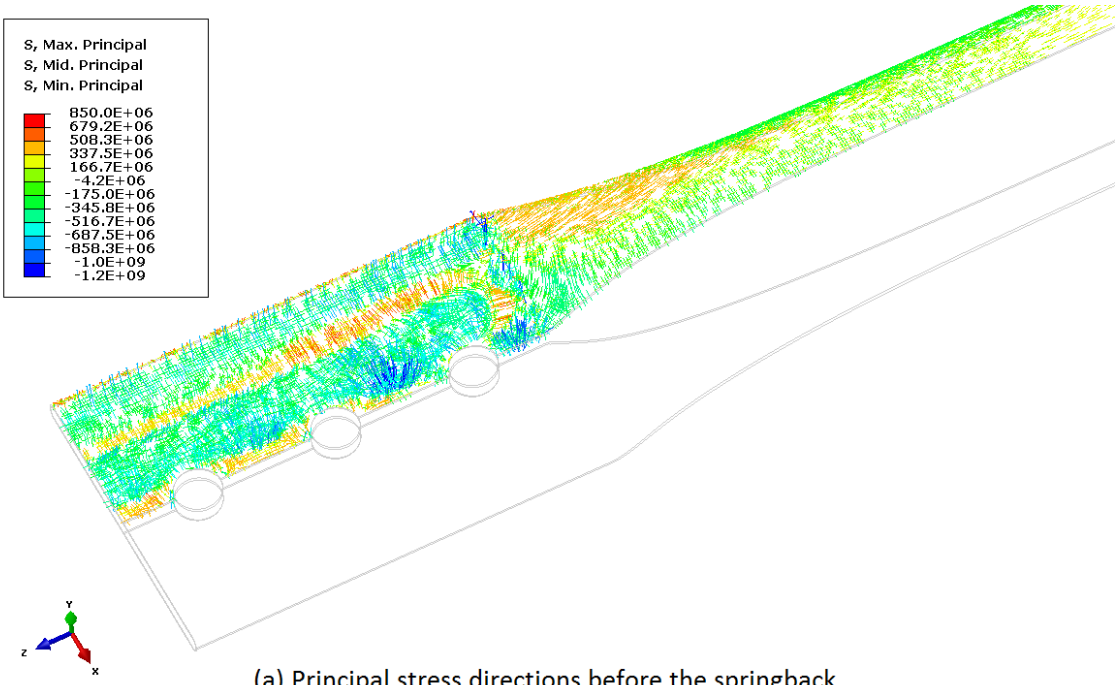

(a) Principal stress directions before the springback

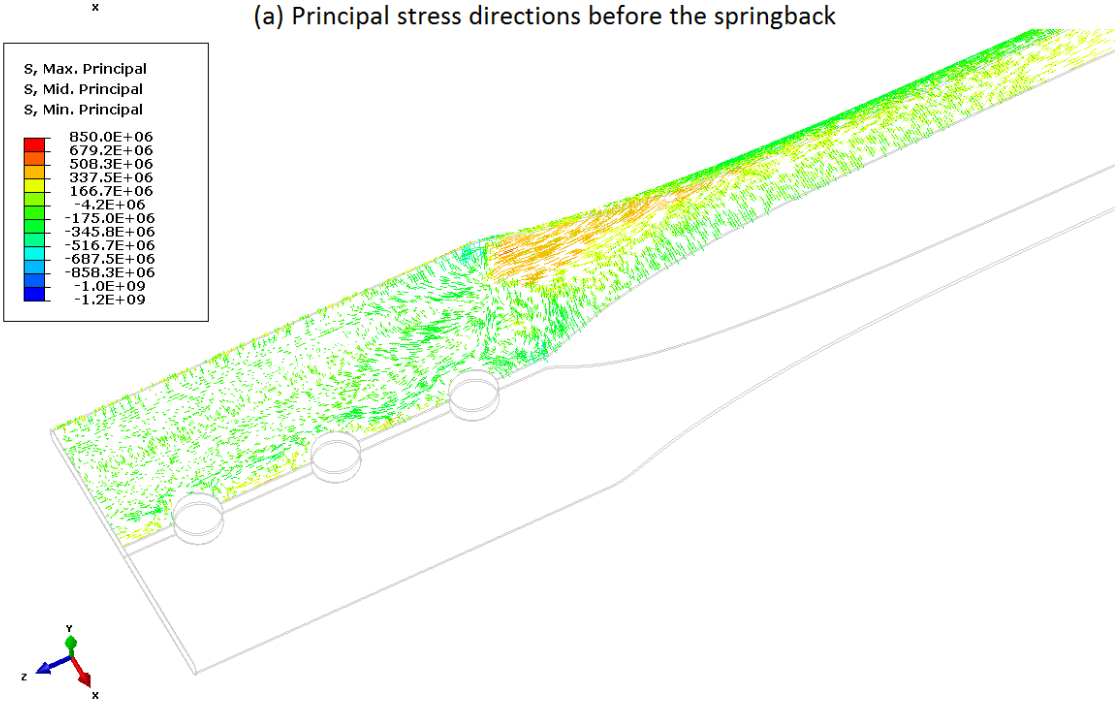

(b) Principal stress directions after the springback

Figure 3-43 Principal stress directions on surfaces of the flattened region.

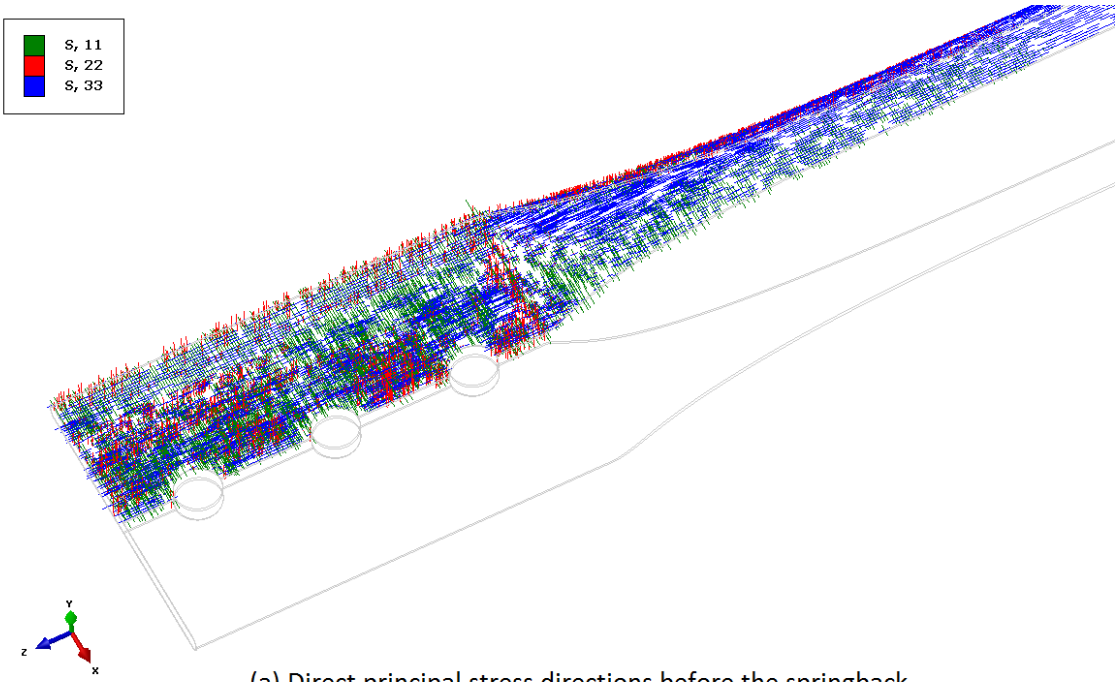

(a) Direct principal stress directions before the springback

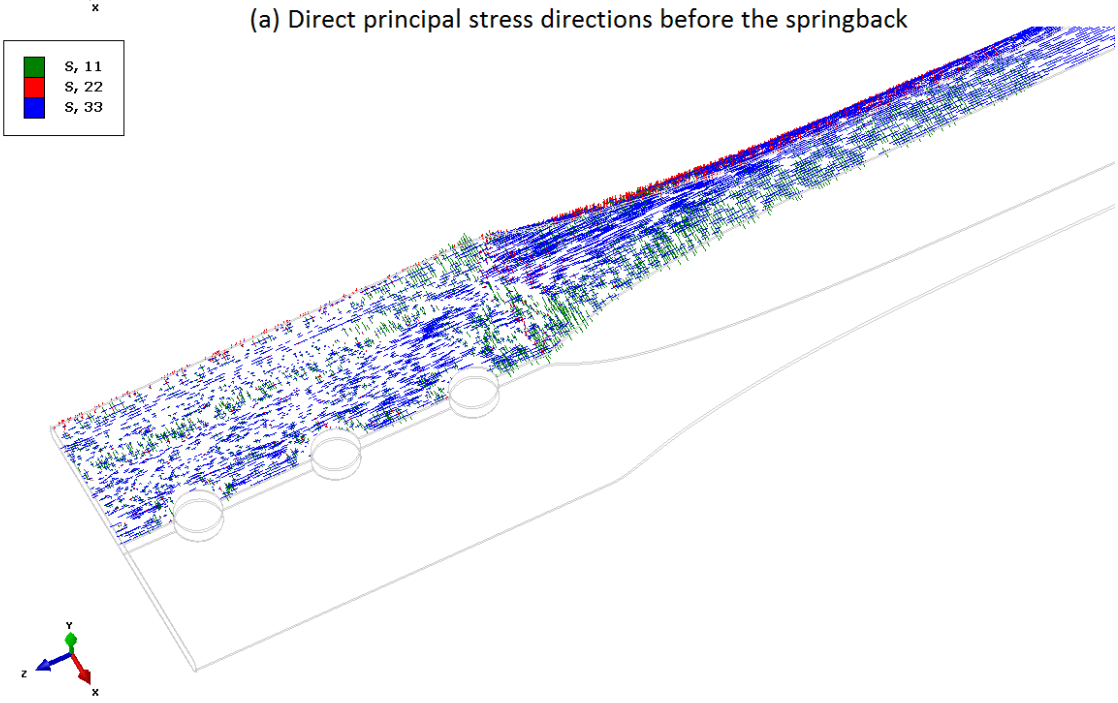

(b) Direct principal stress directions after the springback

Figure 3-44 Direct principal stress directions on surfaces of the flattened region.

3.3.3 Remarks on Part II

The part two consisted of the springback analysis of the flattened tube. The results evaluated the shape changes and the final residual stress distributions. It can be observed that the magnitude of the springback of the tube is quite small with the highest magnitude value being 0.298 mm. The springback is most evident in Y-direction.

However, there is a significant reduction in the stress state before and after the springback as illustrated in Figure 3-40. The highest tensile residual stresses are located at the corner areas in the flat end of the transition zone and in the center area of the circular end of the transition zone as can be observed from Figure 3-41. The center area of the transition zone is in compression. The residual stress pattern and the governing plastic strains are next transferred to the last part of the analysis where the compressive strength of the tube is determined.

3.4 Part III – Compressive Loading

The last part of the analysis studies the behavior of the flattened tube member under axial compressive loading. First, the part assembly and the analysis parameters are redefined to match the experimental test setup. Next, the residual stresses and plastic strains from part two are imported as an initial state. Finally, the maximum compressive resistance is obtained. A comparison to the model without initial stress state is made.

3.4.1 Redefined Parameters for Part III

The model from part two is copied and channel section and bolts are added to the assembly to represent the support conditions used in the experimental study. A rigid punch is used to induce uniform compressive loading to the channel sections. The rigid plane is kept in the longitudinal direction to avoid any self-penetration. The channel section profile is UPE120 and the bolts are fully threaded standard M16 grade 8.8 bolts. The updated assembly configuration is presented completely in Figure 3-45 and a close-up of the channel section and the bolts is presented in Figure 3-46. The new parts are adjusted to establish contact between the bolts and the tube right at the beginning of the analysis. This will eliminate the flat part from the force-displacement curve. The same element formulation used in the first part is adopted for the channel section and the bolts. The material properties of the channel section are the same as used for the tube in the first part. Multilinear material properties for the grade 8.8 bolts are given by [28] and are presented in Figure 3-47.

The implicit analysis step is replaced with explicit dynamic step and the time stepping is redefined. A suitable time period for this study was to be found $t = 0.015\,s$. No mass scaling is used in the analysis. The contacts are switched back to general explicit surface to surface contacts with same tangential behavior than in the part one. The analysis conditions are updated by adding an extra symmetry plane with respect to XY-plane. A displacement of $-25\,mm$ is added to the rigid punch in Z-direction to represent the compressive loading. The channel section and the punch are fixed in X- and Y-direction. A predefined field is created where deformed geometry and the stress and strain states are imported from last step of part two analysis as an initial state.

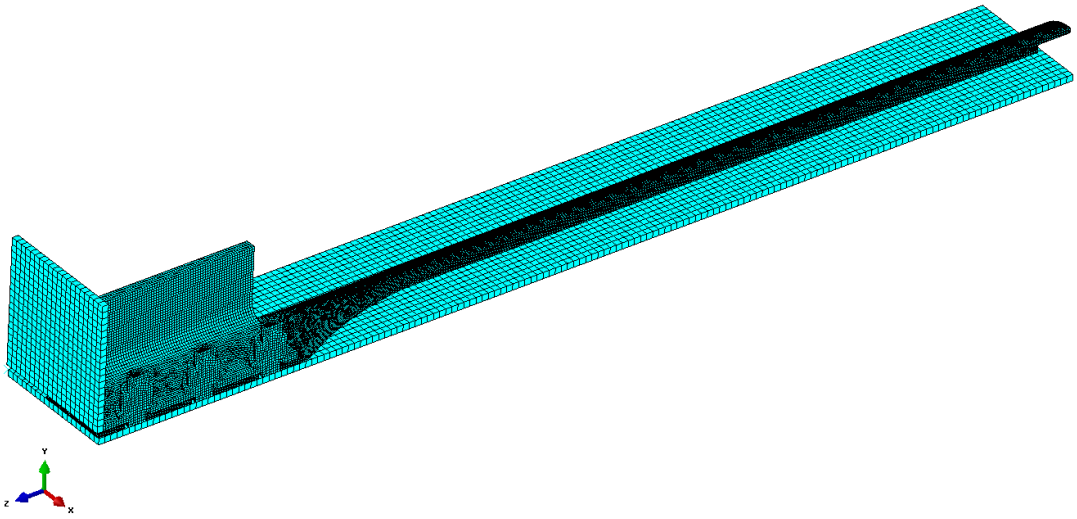

Figure 3-45 Updated assembly for part III.

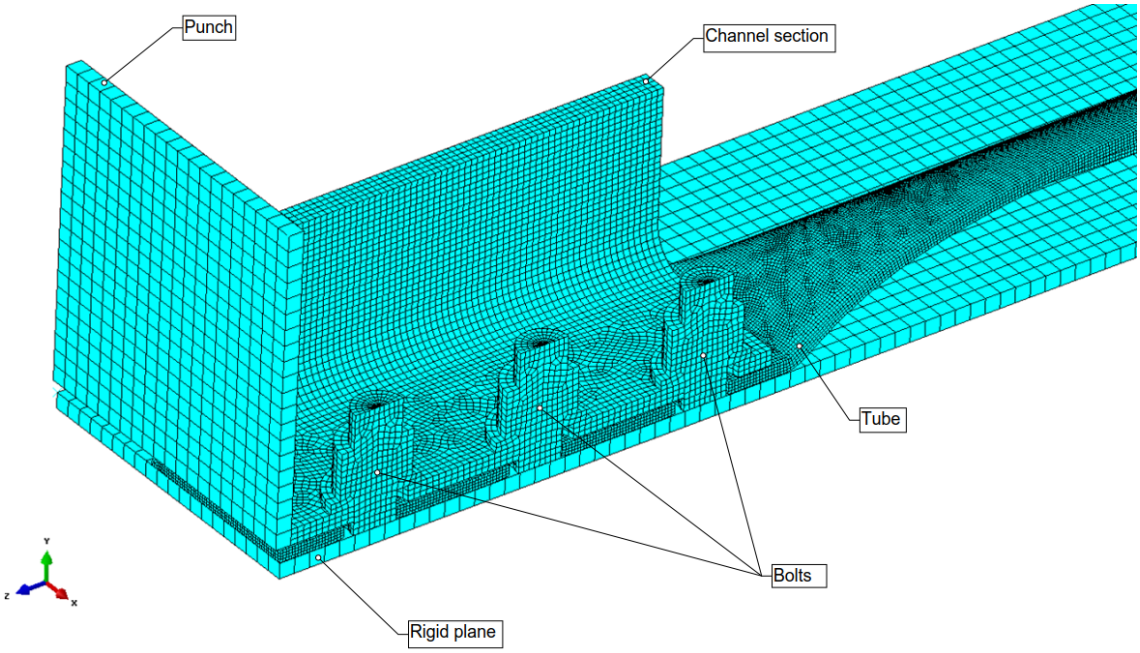

Figure 3-46 A close-up of the channel section and the bolts.

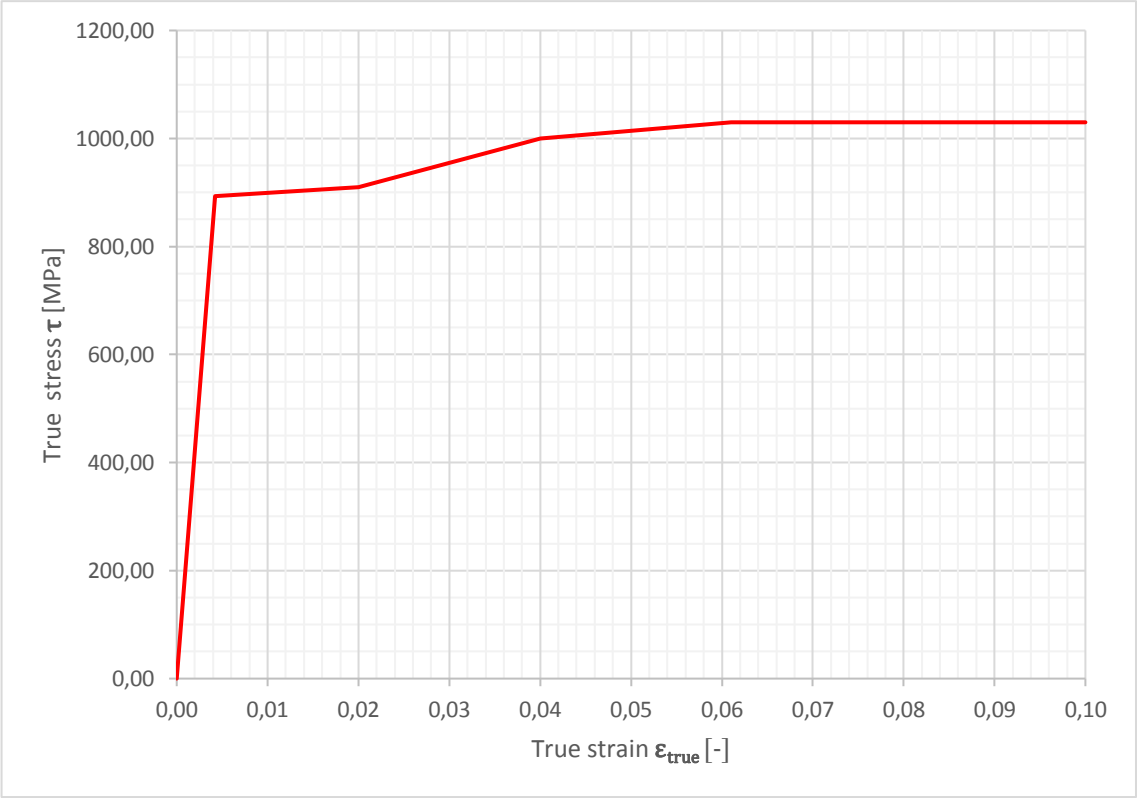

Figure 3-47 Material properties for the grade 8.8 bolt.

3.4.2 Results of Part III

The following subchapters introduce the results of the numerical and experimental studies and the comparison between the results. The first model is a geometrically and materially nonlinear model with initial stress state whereas the second model assumes the virgin material properties for the specimen.

3.4.2.1 Numerical models

The analysis summary is presented in Table 3.13. The energy ratios are well within the proposed limits. The history outputs for model energies are presented in Figure 3-48. The external work is balanced with internal plastic dissipation and frictional dissipation that can be considered as heat energy. There is a small amount of kinetic energy at the beginning of the analysis since no contact has yet been established with the specimen and the channel sections are in free motion. Technically the analysis is fully dynamic before the contact with the specimen is established. However, due to very small velocities this has no significant effect on the results and can be neglected.

Table 3.13 Analysis summary.

	Model I	Model II
Total time period [s]	0.015	0.015
Number of increments [-]	351438	354138
Stable time increment size [s]	4.23e-8	4.23e-8
Kinetic energy / Internal energy [%]	0.51	0.41
Artificial strain energy / Internal energy [%]	2.67	3.78
Internal energy / External work [%]	78.36	86.38
Frictional dissipation / External work [%]	21.02	13.01

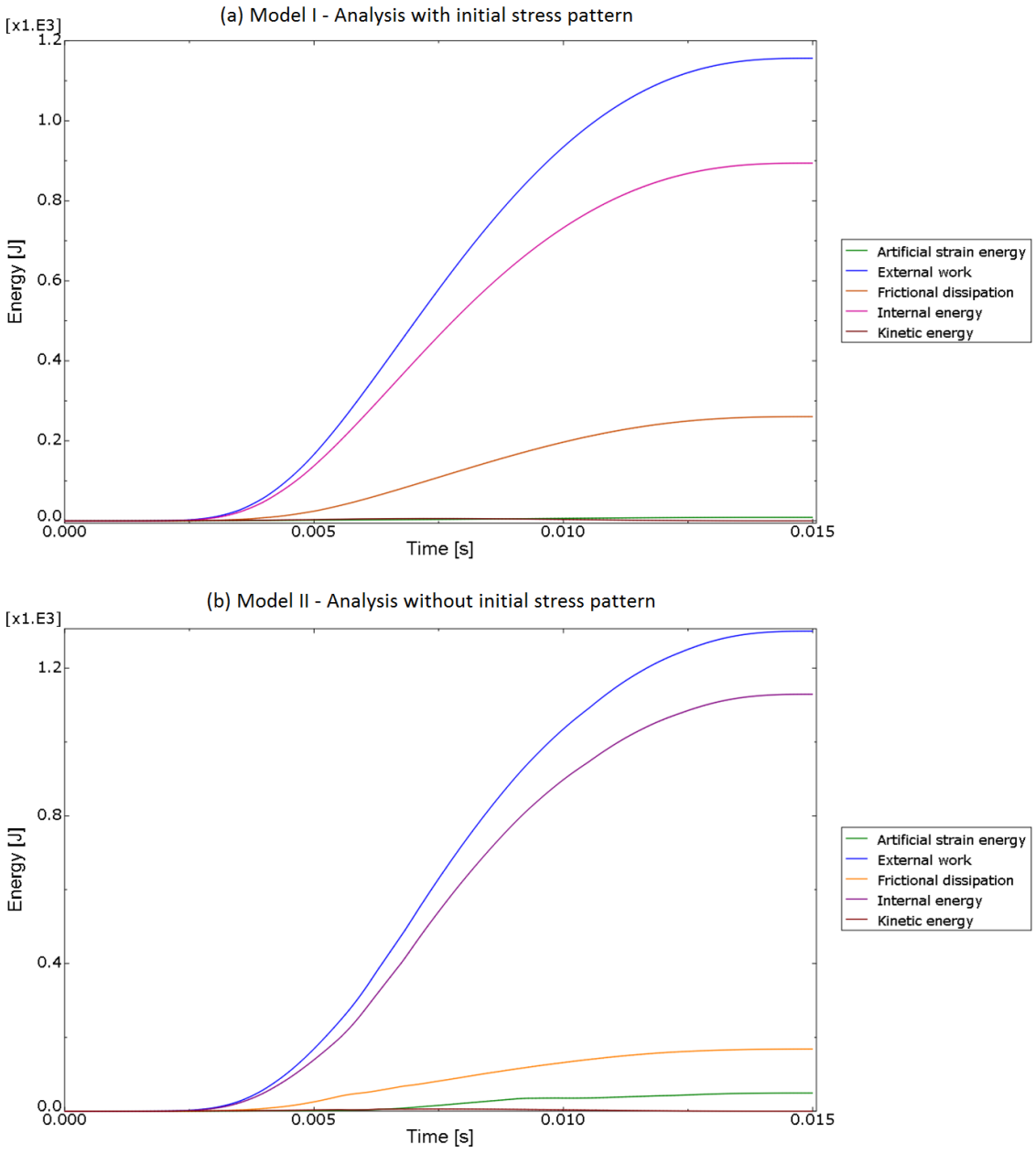

Figure 3-48 Energy summaries.

The specimen reached its maximum compressive resistance with Model I at the analysis time 0.0059 *s* and Model II at the analysis time 0.0054 *s*. Specimens in both models failed due to the excessive deformation of the transition zone. The failure mode is the same characteristic failure mode observed by Dundu [13]. The model state in the end of the analysis is described in Figure 3-49.

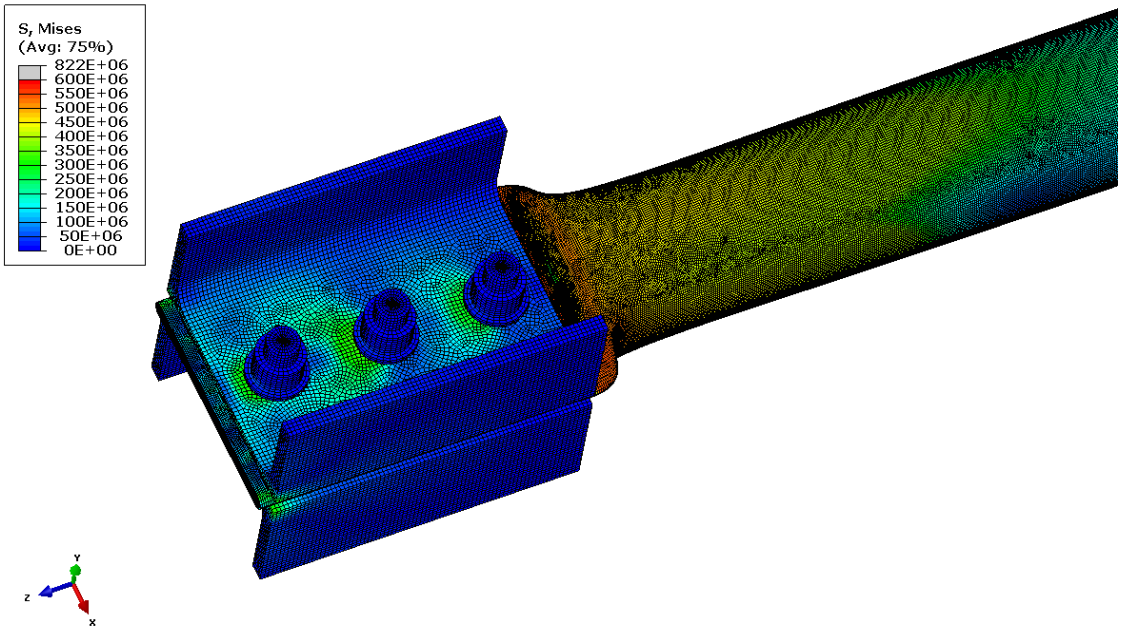

(a) Model I - With initial stress pattern

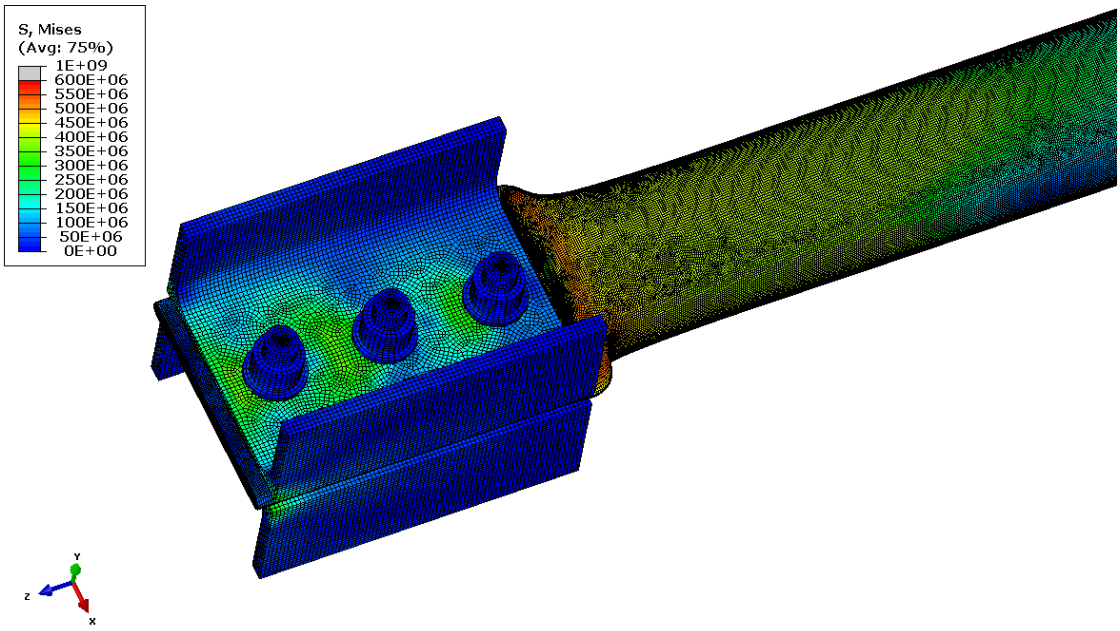

(b) Model II - Without initial stress pattern

Figure 3-49 Whole model in the end of the analysis.

The equivalent von Mises stresses in the tube at the time of failure and at the end of the analysis are presented, respectively, in Figure 3-50 and Figure 3-51. The equivalent plastic strains are presented similarly in Figure 3-52 and Figure 3-53.

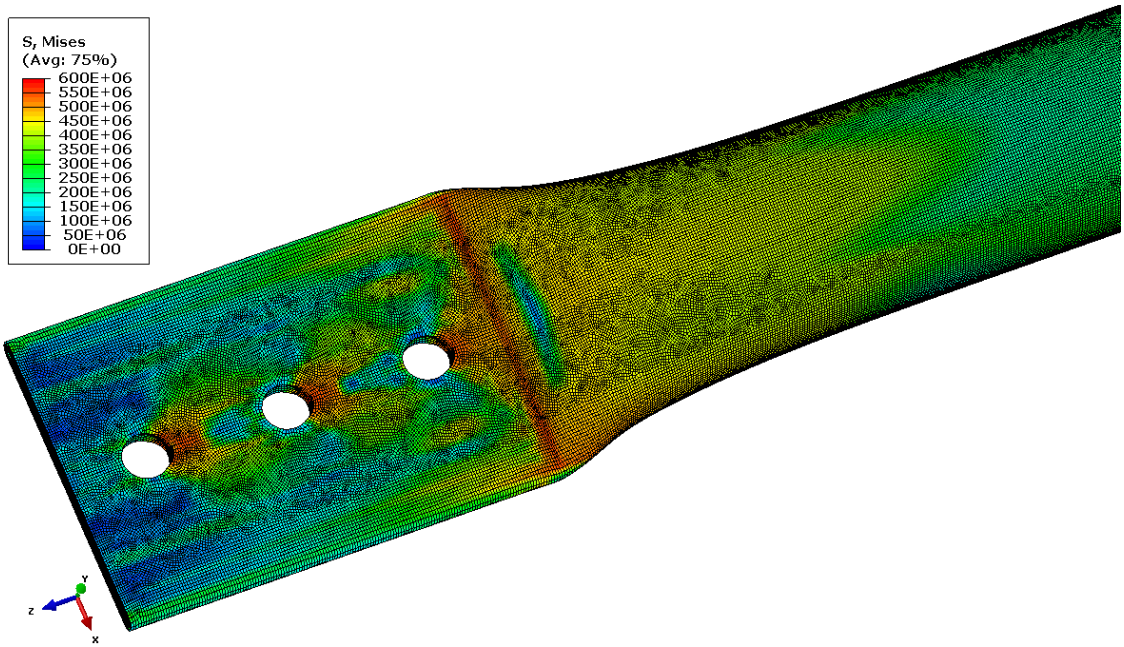

(a) Model I - With initial stress pattern

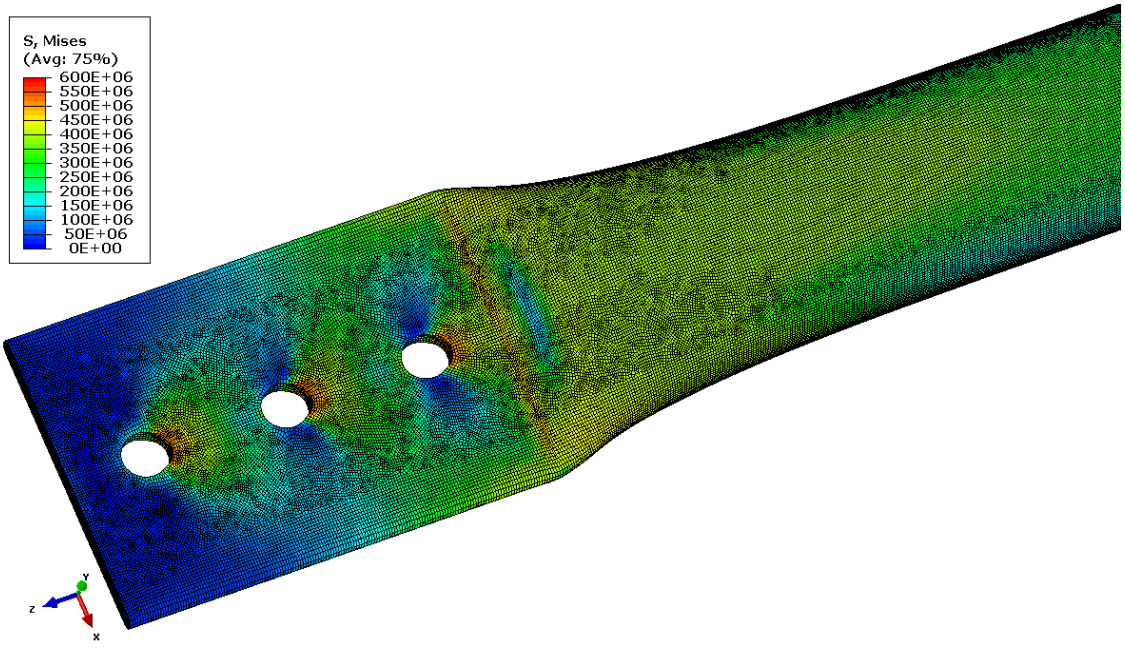

(b) Model II - Without initial stress pattern

Figure 3-50 The equivalent von Mises stresses prior to the failure.

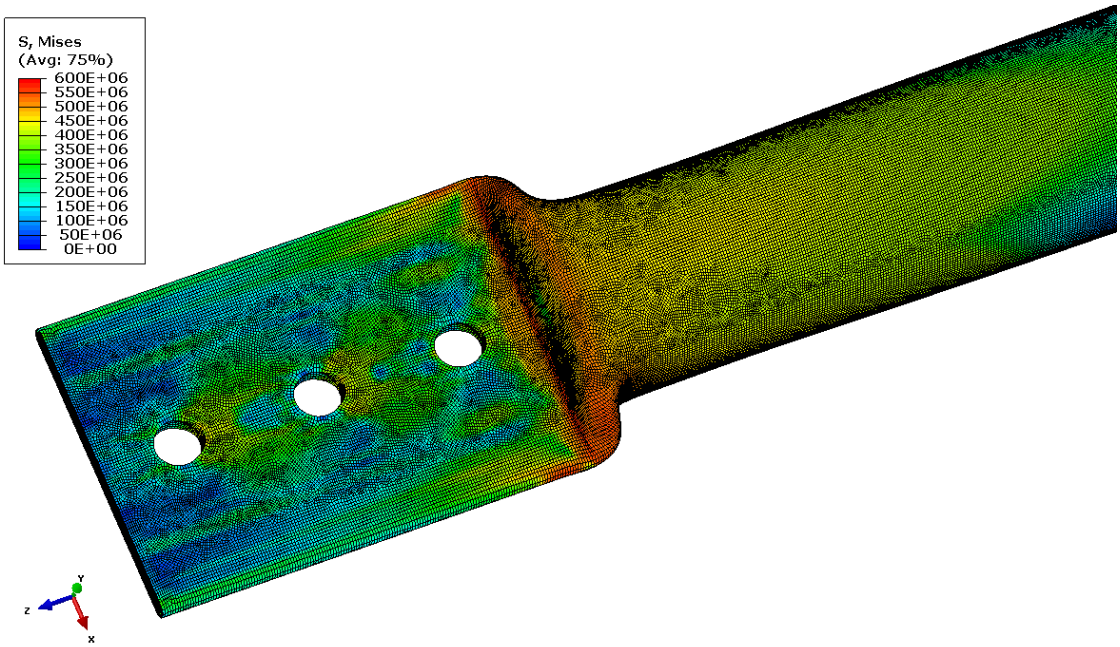

(a) Model I - With initial stress pattern

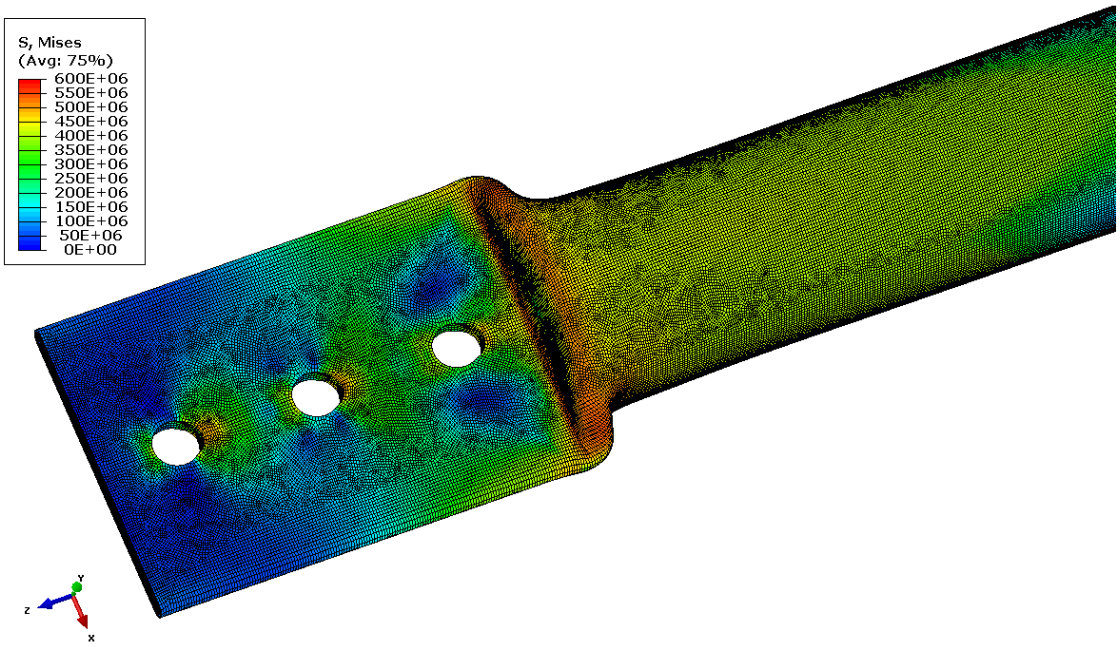

(b) Model II - Without initial stress pattern

Figure 3-51 The equivalent von Mises stresses at the end of the analysis.

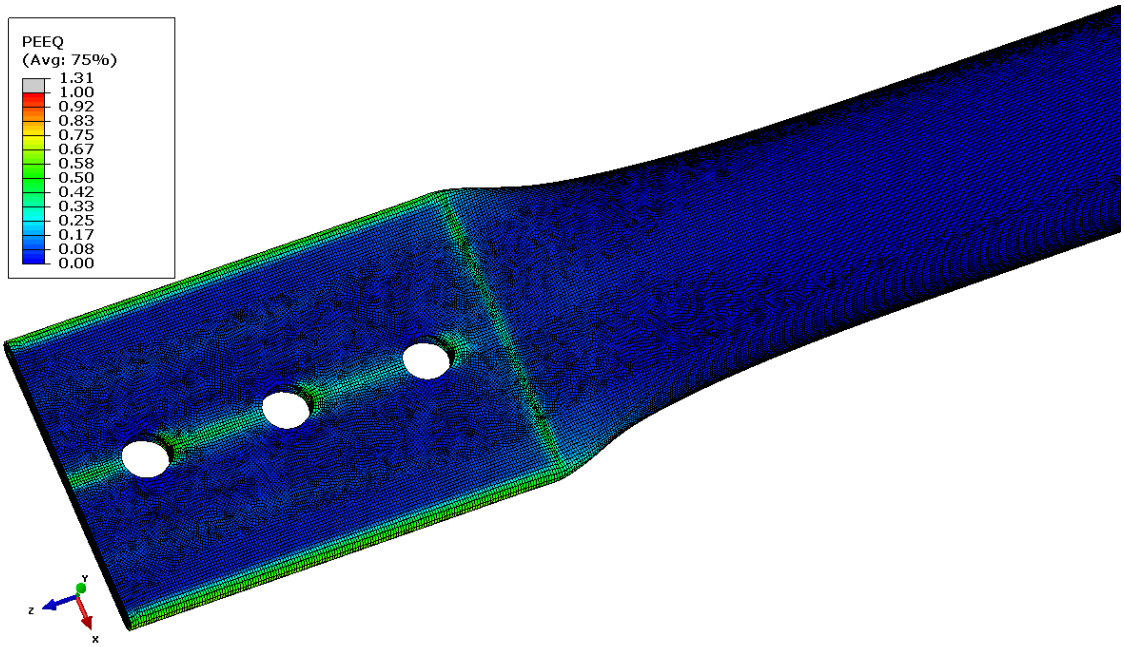

(a) Model I - With initial stress pattern

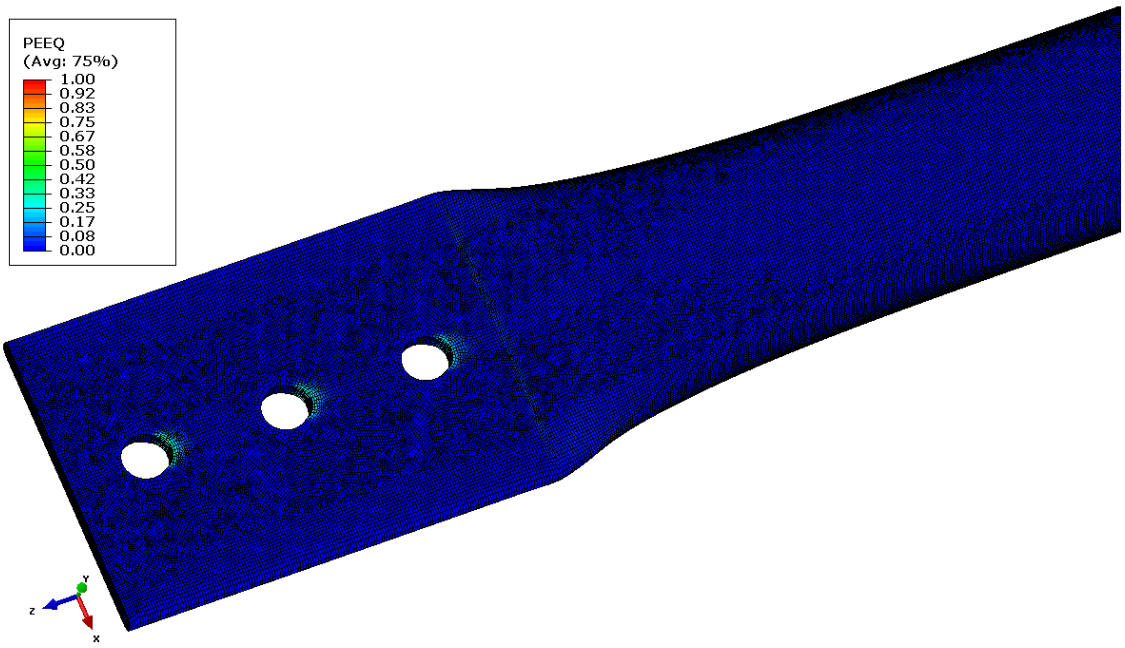

(b) Model II - Without initial stress pattern

Figure 3-52 The equivalent plastic strains prior to the failure.

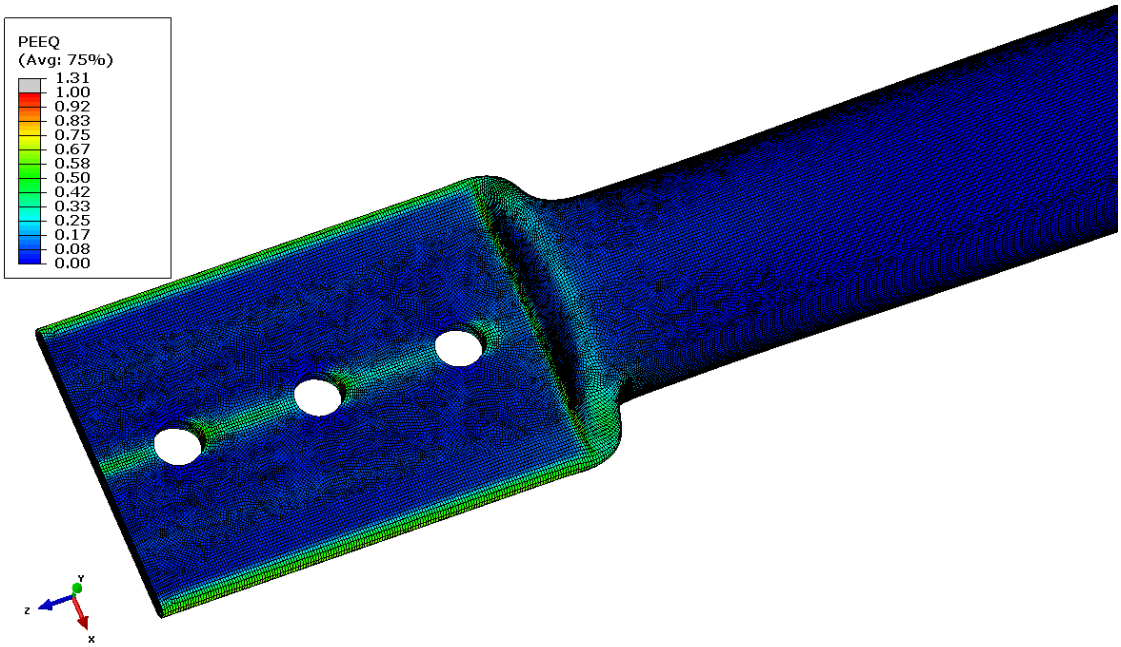

(a) Model I - With initial stress pattern

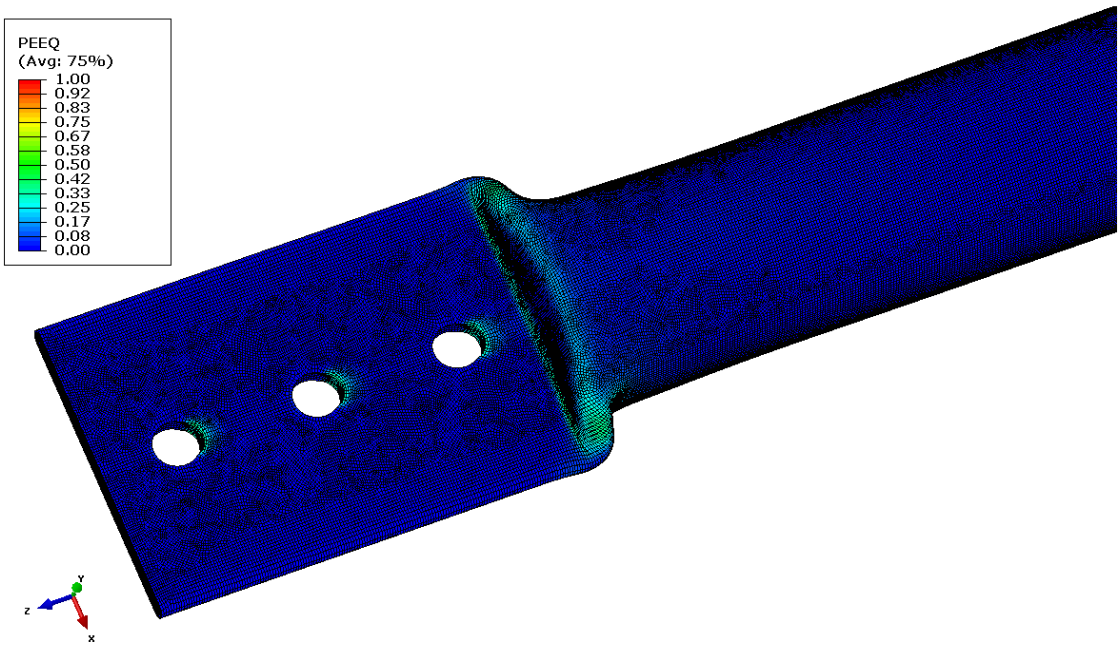

(b) Model II - Without initial stress pattern

Figure 3-53 The equivalent plastic strains at the end of the analysis.

A load-displacement curve is obtained from the field variables for evaluating the structural response and maximum compressive resistance. The average value of displacement is measured from the edge nodes of the flattened end. The load-displacement curves for the models are presented in Figure 3-54. Due to the initial adjustment of the assembly, only a small $0.5\ mm$ adjustment takes place before the structure starts to carry load. The maximum compressive force obtained from the curve

is 230.31 kN for Model I and 217.70 kN for Model II. After this point, the structure can no longer bear any extra load and gradually starts to fail.

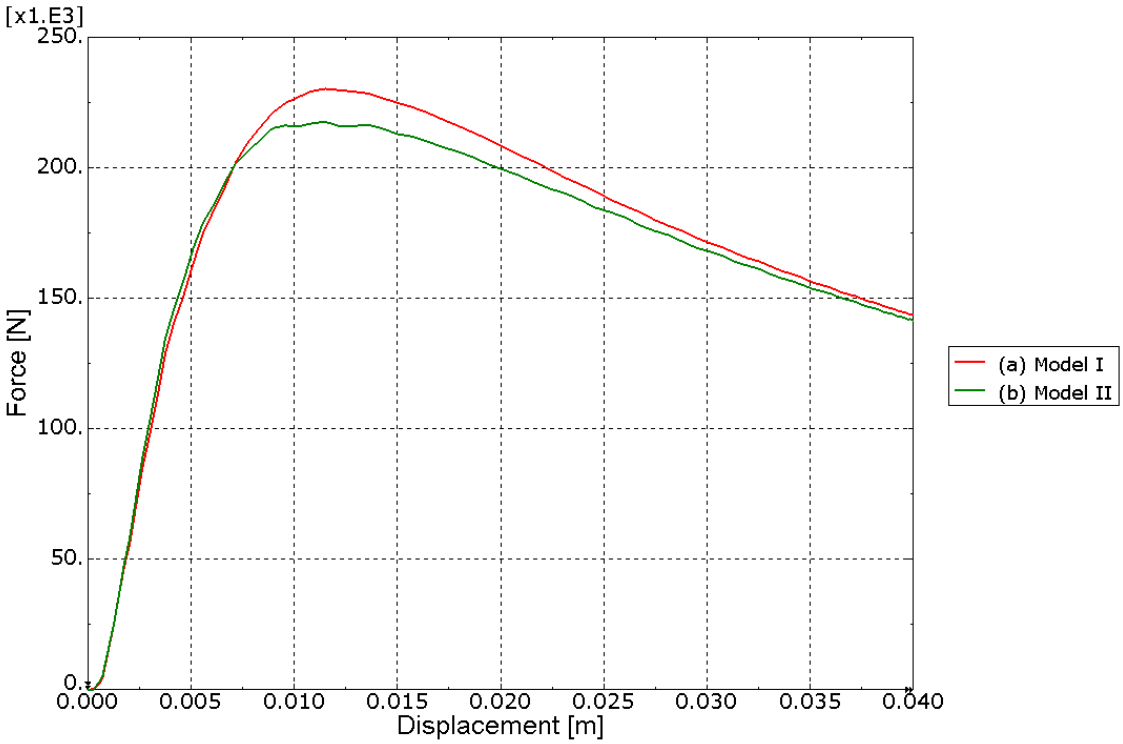

Figure 3-54 Load-displacement curves.

3.4.2.2 Comparison with experimental test data

The load-displacement curve of the experimental test is shown in Figure 3-55. The maximum compressive resistance for 1.6 m long member measured from the curve is 234.64 kN. An increasing compressive axial load was applied at a rate of 2 mm/min. The bolts were only hand tightened to eliminate any contributing friction. A spirit level was used to align the specimens vertically to minimize eccentricities. [13] The comparison between the numerical curves and the experimental curve is presented in Figure 3-56.

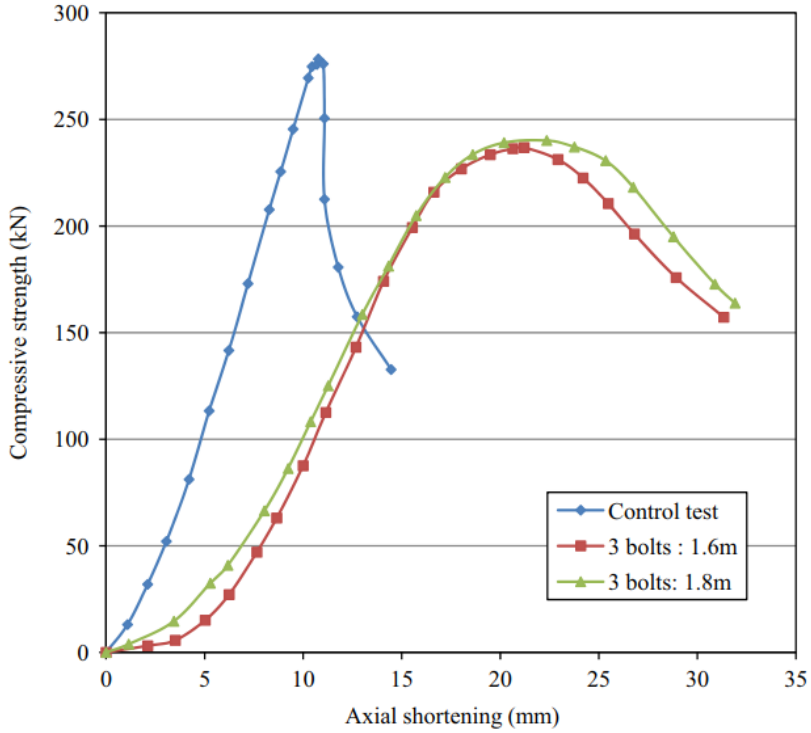

Figure 3-55 Load-displacement curve for 76.2 x 4.0 mm CHS. [13]

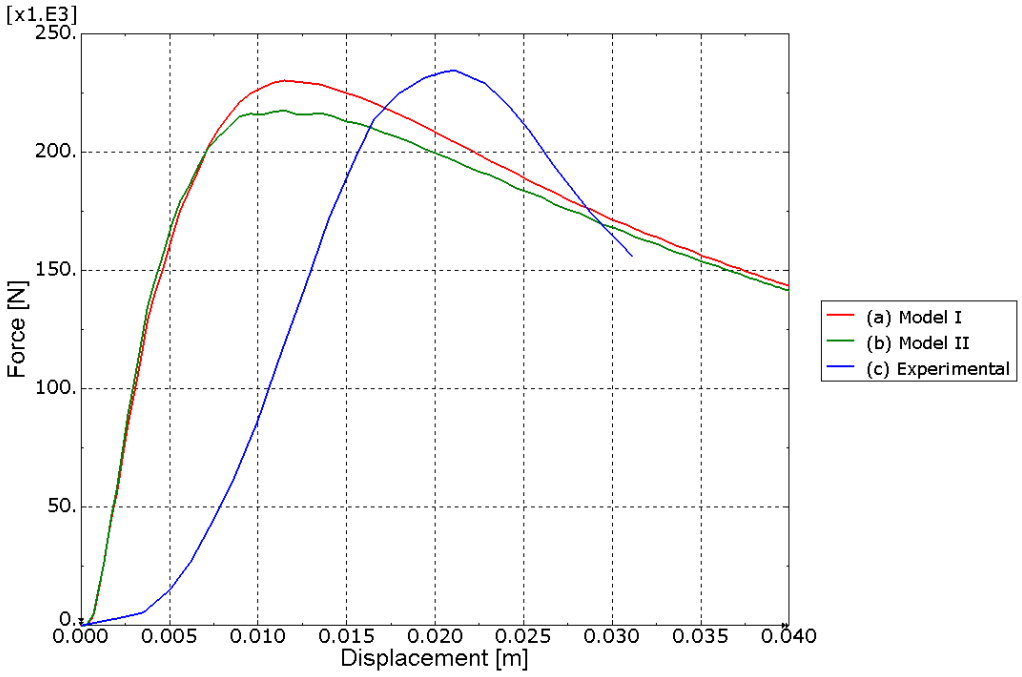

Figure 3-56 Comparison of the load-displacement curves.

The failure mode (excessive deformation of the transition zone) is shown in Figure 3-57. The failure occurs when plastic hinges begin to form in the edges of the transition zone and the member can no longer carry any extra compressive loading. For comparison, the failure modes of numerical studies are shown in Figure 3-58.

Figure 3-57 Excessive deformation of the transition zone in the experimental study. [13]

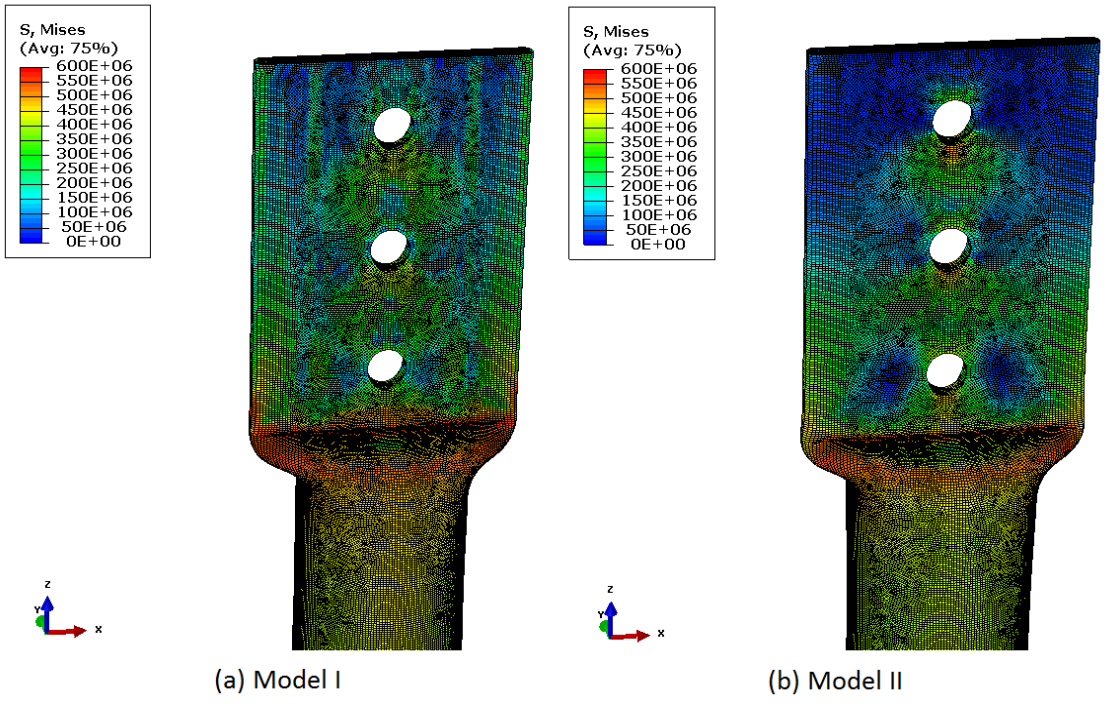

Figure 3-58 Excessive deformation of the transition zone in the numerical study.

3.4.3 Remarks on Part III

The following remarks on the compressive resistance and the structural response can be derived from the results of part III.

3.4.3.1 Compressive resistance

The deviation in maximum compressive resistance between Model I and the experimental test is 1.85 % which can be considered as an excellent result. The residual stresses improved the maximum compressive resistance by 5.79 %. This can be explained with high tensile stresses in the transition zone as seen in Figure 3-42.

3.4.3.2 Structural response

The axial stiffness of the numerical model is higher when compared to the experimental results. If the curves are shifted to overlap at the point of maximum load, a small dip in the experimental test curve is seen before the specimen starts to carry load. The overlapped curves are presented in Figure 3-59.

There are several possible reasons like bolts, axial shortening and imperfections causing this kind of nonlinear response. During the dip, any slack in the connection is being eliminated. As mentioned in chapter 3.4.2.2, the bolts were only hand tightened to eliminate any frictional contribution. Usually a tolerance of $2\,mm$ is used in the bolt holes for a better fitting. Therefore, the bolts can move into a skew position prior to actual loading leading to less stiff structural response. Some contributing effects can also arise from the bolt holes not being perfectly round but slightly elliptical. In addition, the use of spacers leads to longer bolts that can bend during loading and result in less stiff response.

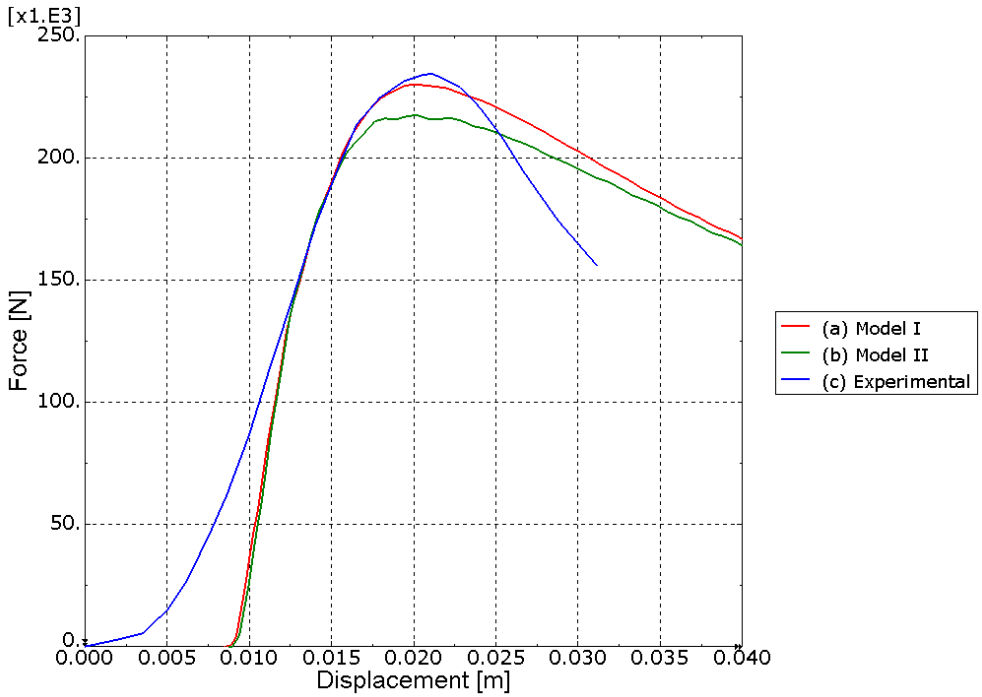

Figure 3-59 Overlapped load-displacement curves.

The tube specimen sligthly shortens during the flattening phase. As demonstrated in the experimental study (Figure 3-55), the length of the tube has some effects on the structural response. However, the shortening in the tube specimen was only 8 mm so these effects can be considered negligible.

The tube was assumed prismatic prior to the flattening and no global imperfections were introduced in the model. The global initial imperfection alters the buckling behavior of compressed members as the load-path until the bifurcation point changes. Depending on its amplitude, it may also have a detrimental effect on the critical load and stiffness. However, when the failure mode is local, the global imperfections play a less important role in the overall analysis.

In the experimental study, the structural bearing capacity drops quickly after the failure whereas the numerical models gradually lose their capacity. This indicated that actual damage i.e. cracking occurs in the test specimen. The residual stresses have no significant effect on the axial stiffness nor the post buckling behavior.

4 Numerical Studies of Stress and Strain Patterns in the Vicinity of Flattened End in Various Stages

This chapter introduces the field variable patterns for stresses and strains in the tube specimen. The numerical simulations conducted in the following chapter are formulated with the same analysis parameters as in chapter 4. To model accurately the field variable patterns chosen, the model is flattened without bolt holes since they affect the distributions as discussed earlier. The distribution patterns are presented both in the flattening and the final stage, or the condition after the springback. The field variable distributions are evaluated at two section cuts, one in the circumferential direction within the flattened region, and one in the longitudinal direction within the transition zone. The sections are defined in Figure 4-1. Only the top and bottom surfaces are included in the study.

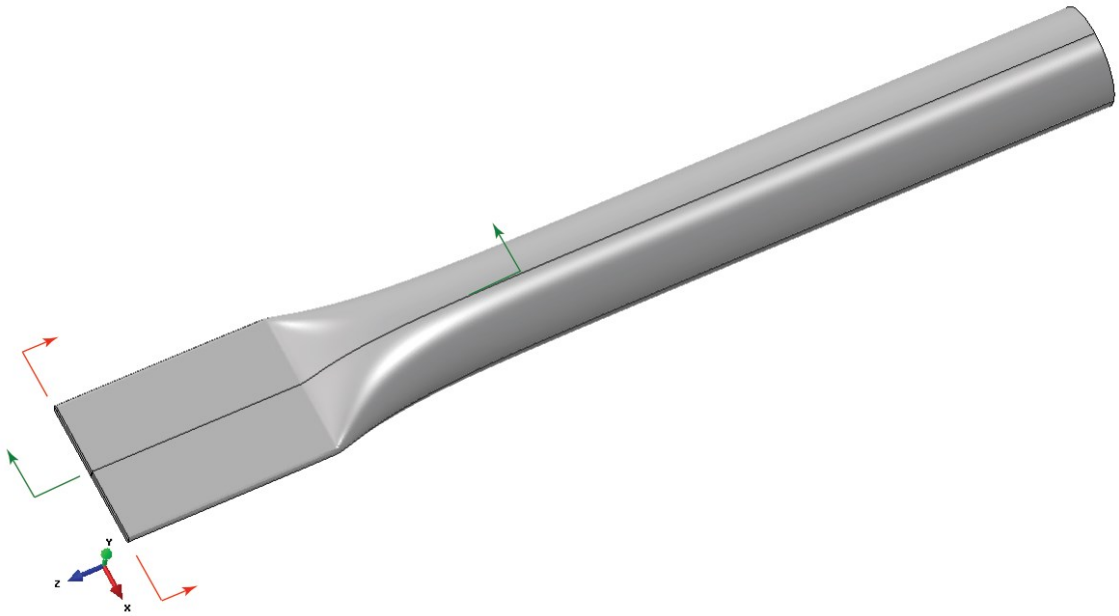

Figure 4-1 The transversal section (red) and the longitudinal section (green) where the field variables will be evaluated.

The material orientations must be considered when obtaining the field variables in the principal directions. The proposed elemental directions for a quarter model are presented in Figure 4-2. The first principal axis (cyan) represents the circumferential direction, the second principal axis (yellow) the radial direction and the third principal axis (red) the longitudinal direction. The field variables are obtained via paths intersecting the elements on the top and the bottom surface of the specimen. The element sequence ID shown in the following subchapters refers to the element sequence number starting from the zero position as shown in Figure 4-3 and Figure 4-4.

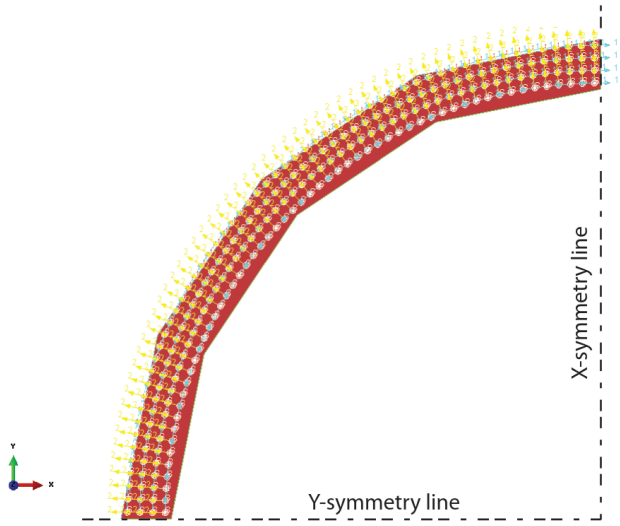

Figure 4-2 Elemental material orientations.

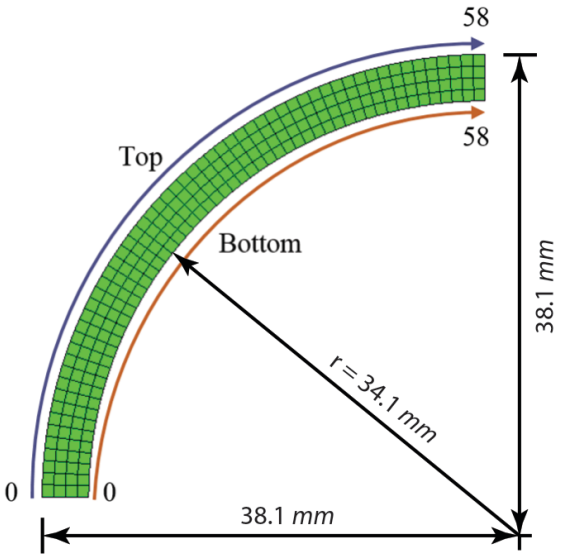

Figure 4-3 Predefined top and bottom surface paths for circumferential sections.

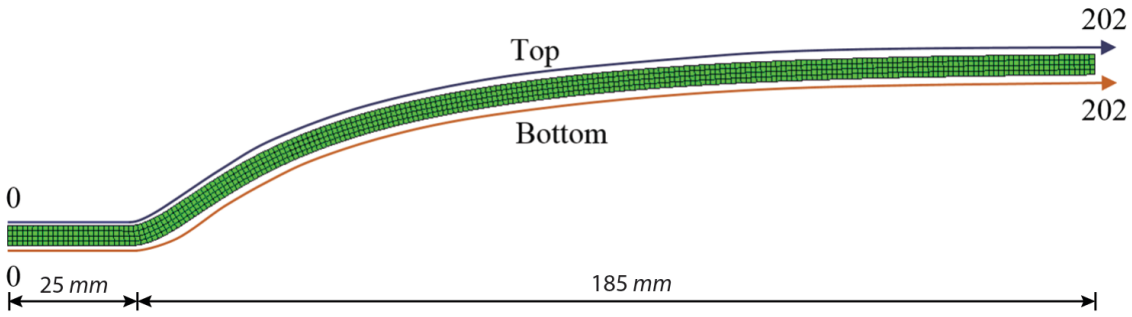

Figure 4-4 Predefined top and bottom surface paths for longitudinal sections.

4.1 Flattening Stage

The stresses and strains are evaluated at five different flattening stages as shown in Figure 4-5 and Figure 4-6. A flattening stage refers to the die displacement in y-direction (100 % equals the die displacement of 34.1 mm). Since there is only a small difference between the results within the sections, only results for one transverse and longitudinal section is presented in the subchapters.

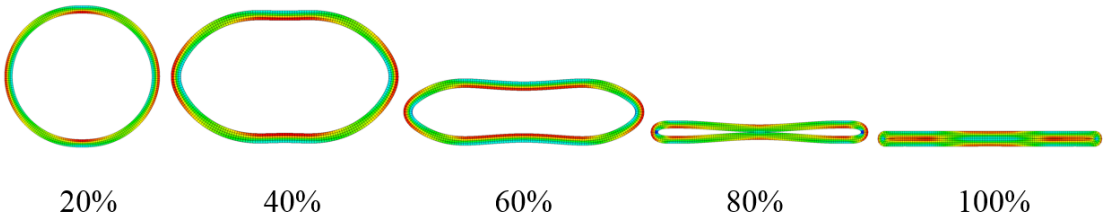

Figure 4-5 Five stages of flattening in the circumferential direction.

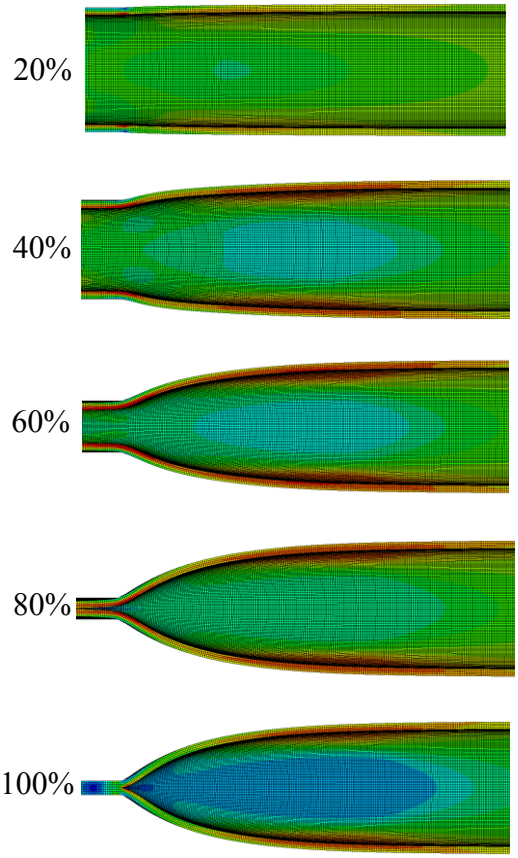

Figure 4-6 Five stages of flattening in the longitudinal direction.

4.1.1 Forming Stresses in the Circumferential Direction

The forming stresses in the circumferential direction at the top surface are presented in Figure 4-7 and at the bottom surface in Figure 4-8. At the top surface the compressive stresses starting from the last element on the stress path propagate steadily until 60 % flattening stage. Before 80 % flattening stage, the inner surfaces of the tube establish a contact between each other and a stress reversion takes place. After the plastic reversion, the stress path takes its final shape becoming more steep and expanding the length of fully plasticized regions. The stress pattern at the bottom surface behaves similarly; compressive and tensile regions being opposite in respect of the thickness of the tube wall.

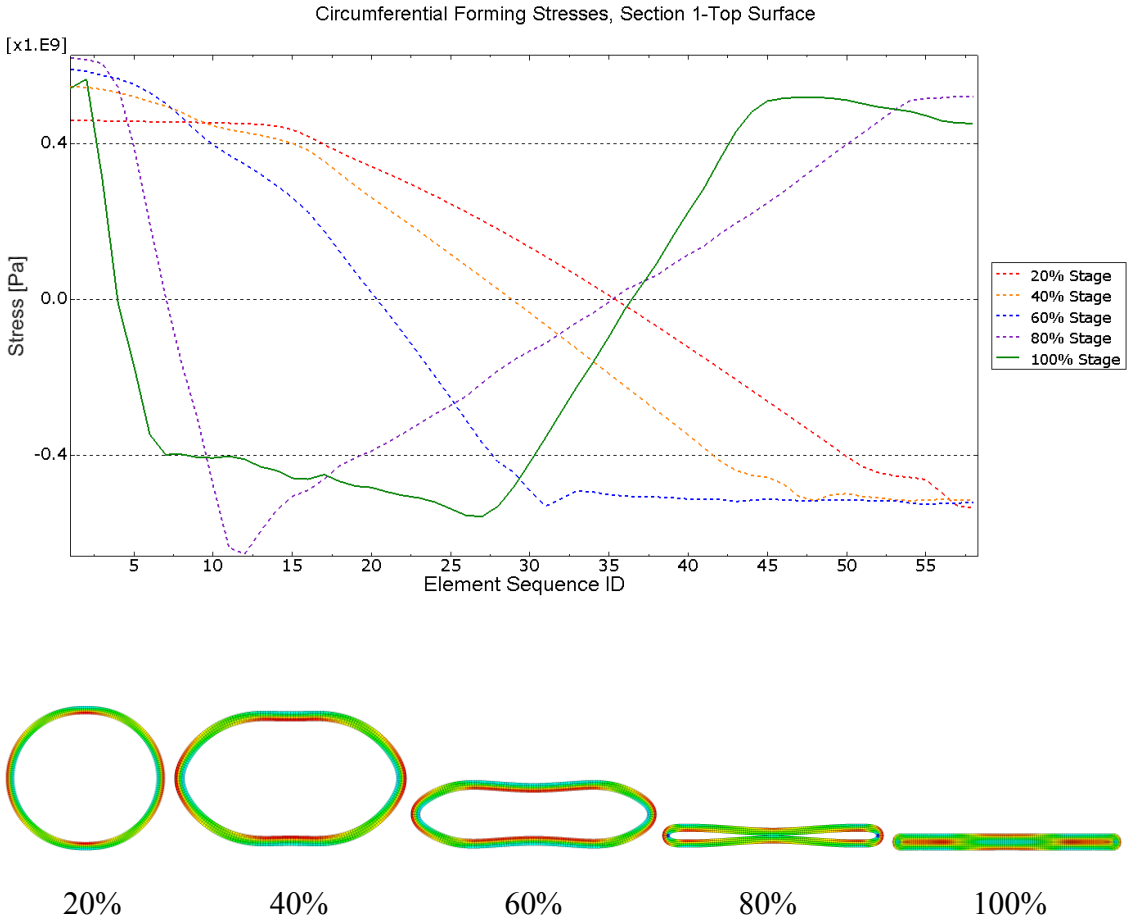

Figure 4-7 Circumferential forming stresses at the top surface.

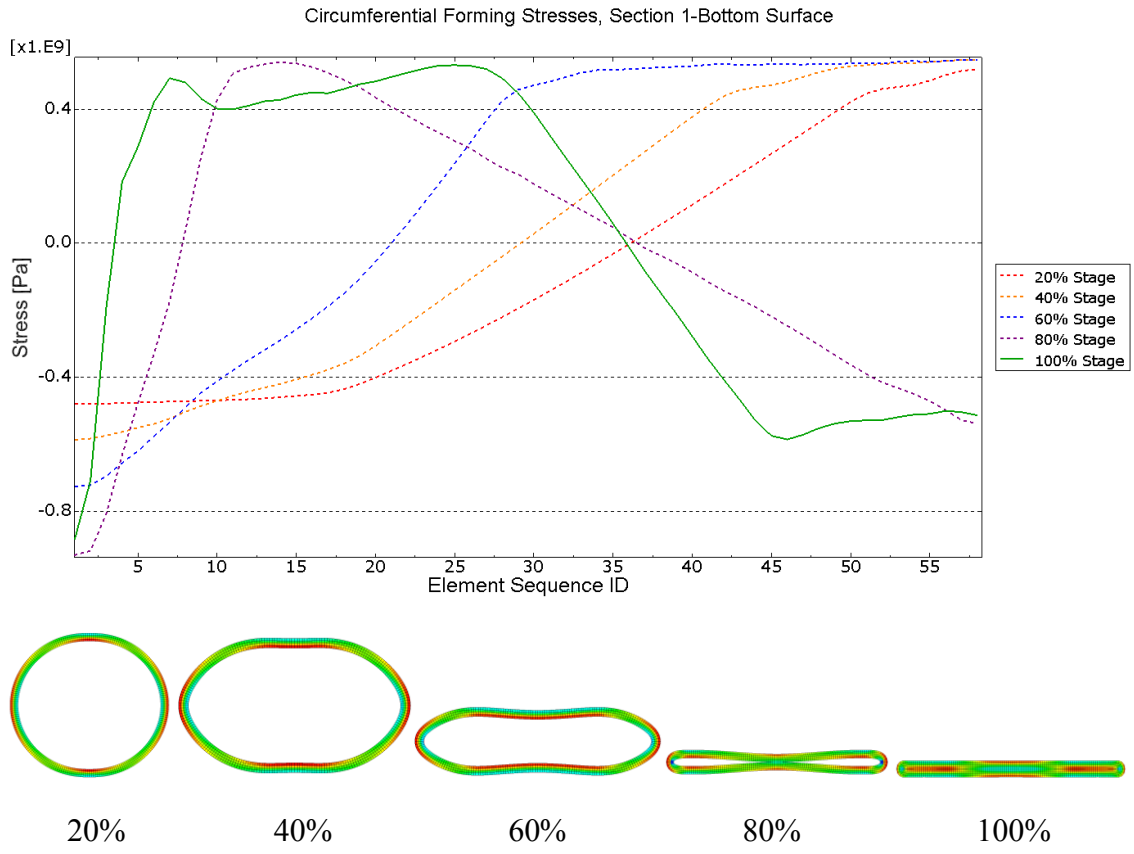

Figure 4-8 Circumferential forming stresses at the bottom surface.

4.1.2 Total Strains in the Circumferential Direction

The total logarithmic strains in the forming stage on the top surface are presented in Figure 4-9 and on the bottom surface in Figure 4-10. The logarithmic strain is defined as [15]:

$$\varepsilon_{log} = \ln\left(\frac{l}{l_0}\right) \tag{4.1}$$

where

l is the current length of the material line

l_0 is the original length of the material line

Moreover, the total logarithmic strain can be decomposed into elastic and plastic component as [15]:

$$\varepsilon_{log} = \varepsilon_{log}{}^{el} + \varepsilon_{log}{}^{pl} \tag{4.2}$$

As mentioned in 3.2.9.1, the first set of plastic hinges develops on the vertical symmetry axis and the second on the horizontal symmetry axis. From Figure 4-9 it can be observed that in the beginning of the flattening the strains at the end of the observation path are larger than those in the start. However, as the flattening progresses, the strains at the start of the path rapidly become much higher; being roughly tenfold in the end of the flattening. Even though there are tensile stresses at the end of the path, the strains in these areas remain compressive. This indicates that these areas became highly plasticized before the stress reversion took place and most of the top surface area is physically in a compressed state. On the other hand, a small decrease in total strain can be observed which refers to the elastic strain reversion. Again, similar observations can be made from the bottom surface results in the opposite direction.

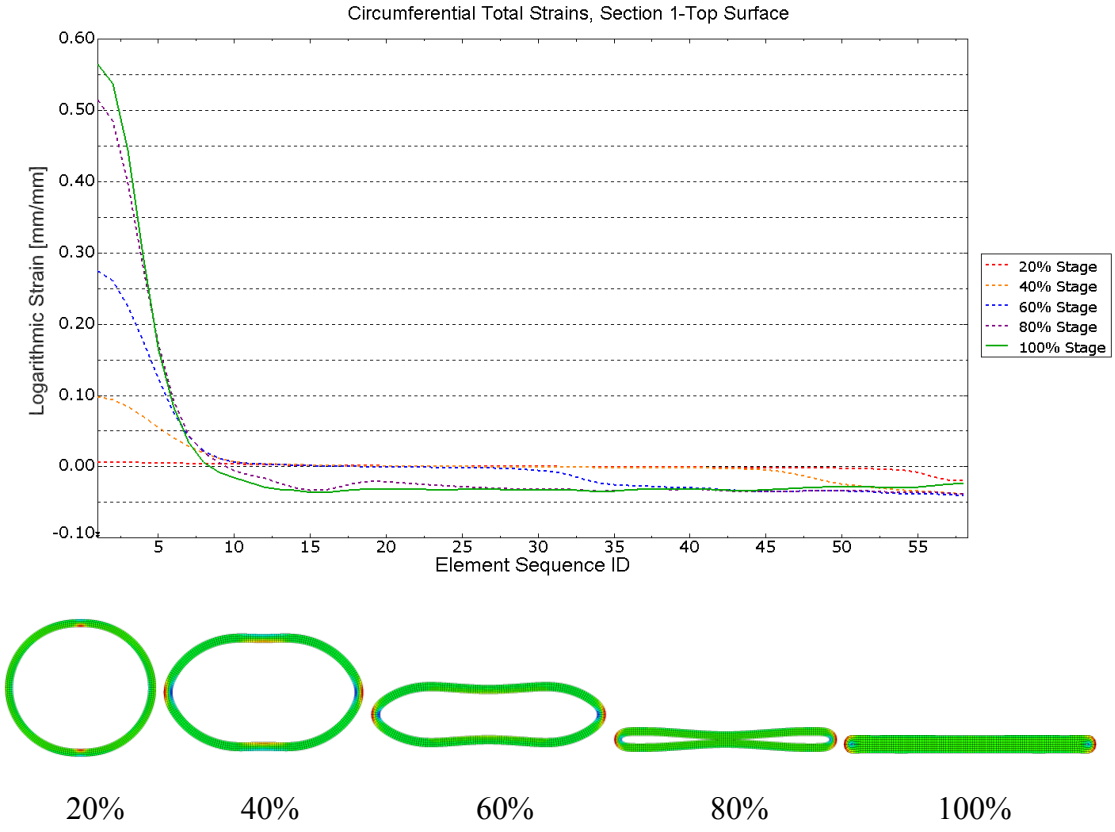

Figure 4-9 Total circumferential strains during the forming stage at the top surface.

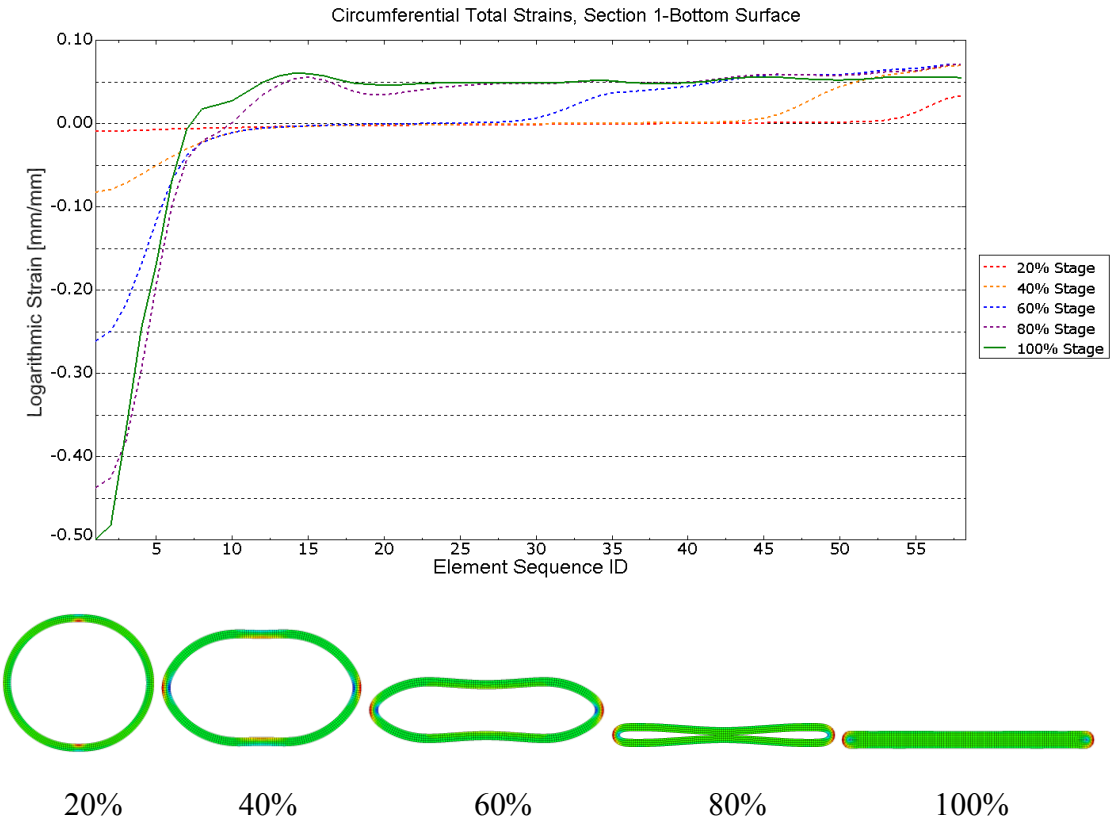

Figure 4-10 Total circumferential strains during the forming stage at the bottom surface.

4.1.3 Forming Stresses in the Longitudinal Direction

The forming stresses in the longitudinal direction at the top surface are presented in Figure 4-11 and at the bottom surface in Figure 4-12. When moving forward on the observation path, the stresses at the top surface are compressive until the end of the influence area of the punch die. After this point the stresses become tensile, increasing when moving further towards the end of the path. At the end of the forming, the final set of plastic hinges (as described earlier in Figure 3-28 in chapter 3.2.9.1) develop at the root of the transition zone and a plastic reversion takes place. There are some similarities in the stress pattern at the bottom surface since the compressive and tensile areas are more or less the same. This indicates that there is no bending at the transition zone but the cross section overall is in tension.

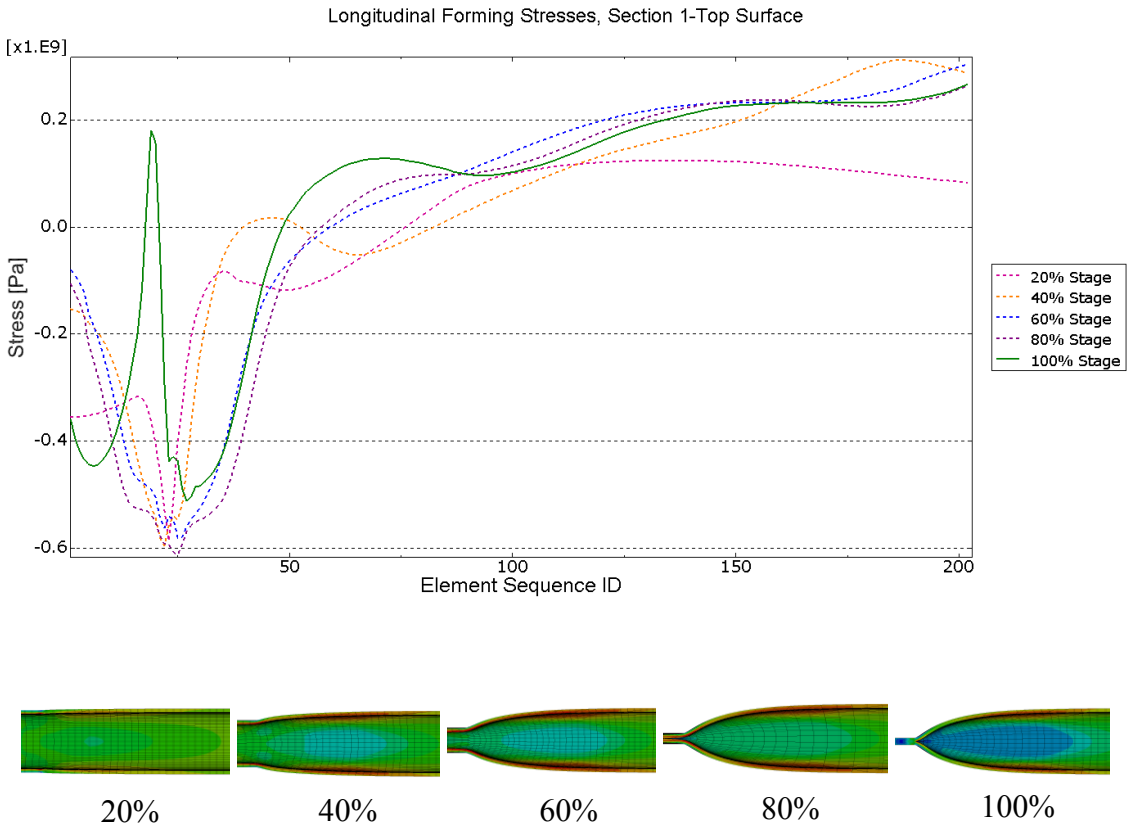

Figure 4-11 Longitudinal forming stresses at the top surface.

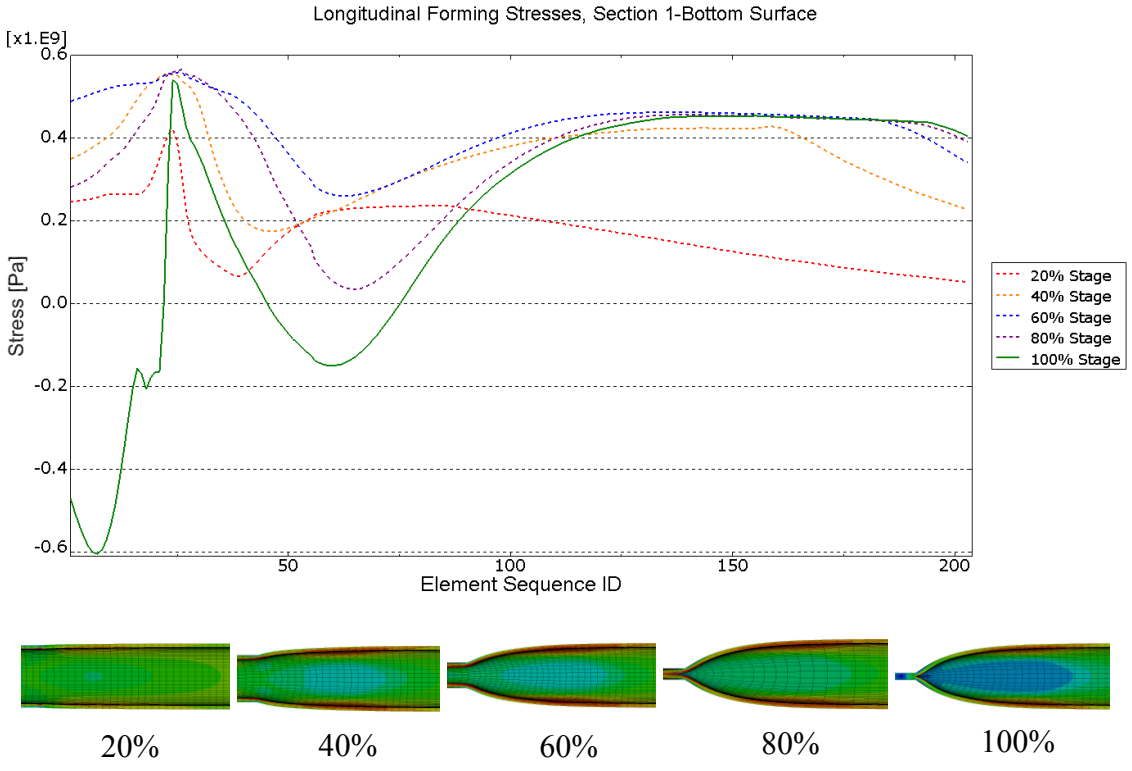

Figure 4-12 Longitudinal forming stresses at the bottom surface.

4.1.4 Total Strains in the Longitudinal Direction

The total logarithmic strains in the forming stage on the top surface are presented in Figure 4-13 and on the bottom surface in Figure 4-14. The strains develop smoothly as the forming proceeds and again the evolution of plastic hinges can be observed at the root of the transition zone as mentioned in chapter 3.2.9.1. The stress reversion occurring at the top surface in the final stage around element number 20 results in a small local increase in tensile strains before the dip in the plastic hinge region. In the end of the analysis, most of the elements on the sequence path are plasticized to varying magnitude. Similar observations can be made from the bottom surface results in the opposite direction.

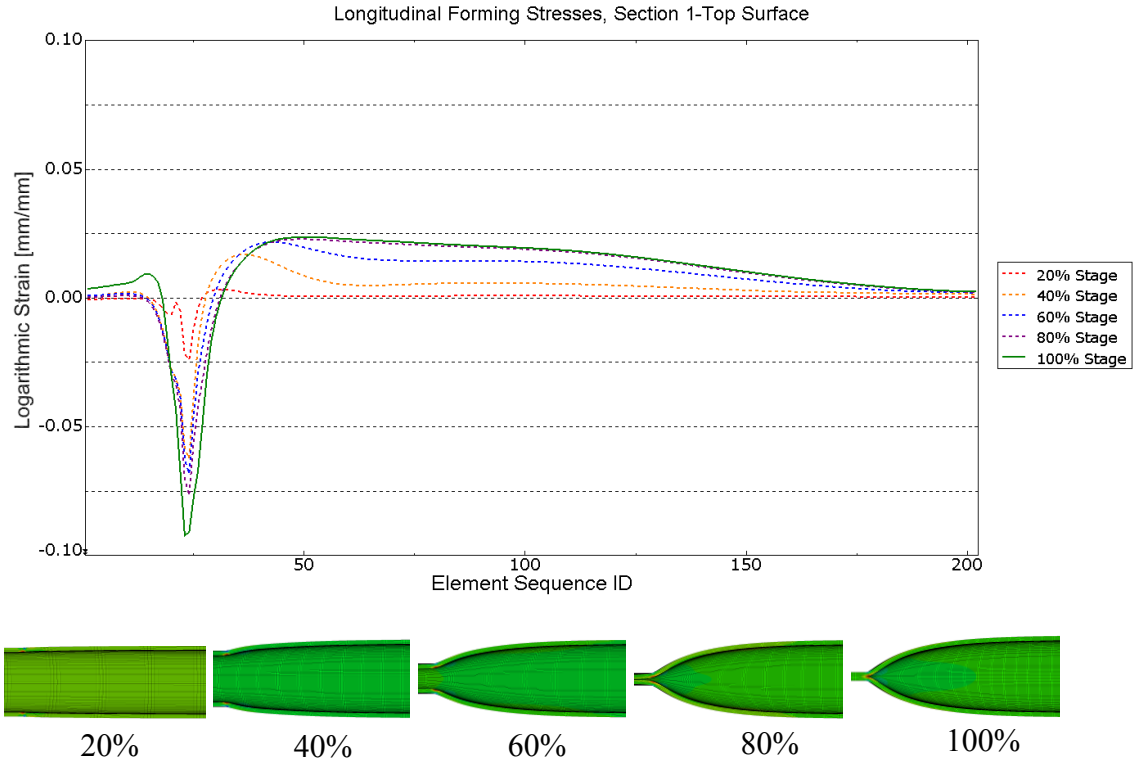

Figure 4-13 Total longitudinal strains during the forming stage at the top surface.

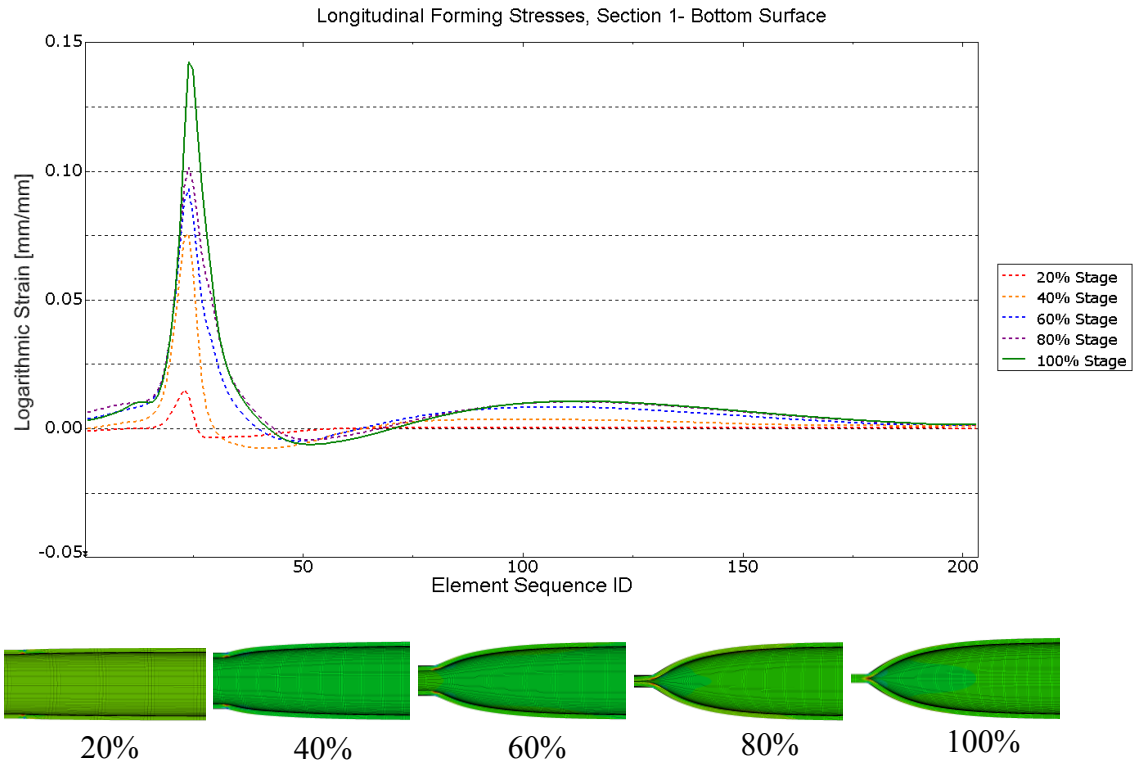

Figure 4-14 Total longitudinal strains during the forming stage at the bottom surface.

4.2 Springback Stage

The stresses and strains in the springback stage are obtained at the same sections as in the flattening stage. The field variable distributions are observed at the end of the forming stage ($t = 0$) and after the springback ($t = 1$). Result comparison between the stages is included.

During the springback stage, the elastic strains revert and relieve the stress state in the specimen. The occurred elastic strain reversion is presented in the circumferential and the longitudinal direction, respectively, in Figure 4-15 and Figure 4-16. The maximum magnitude of the strain reversion in the circumferential direction is around 2.3 % and in the longitudinal direction around 1.8 %.

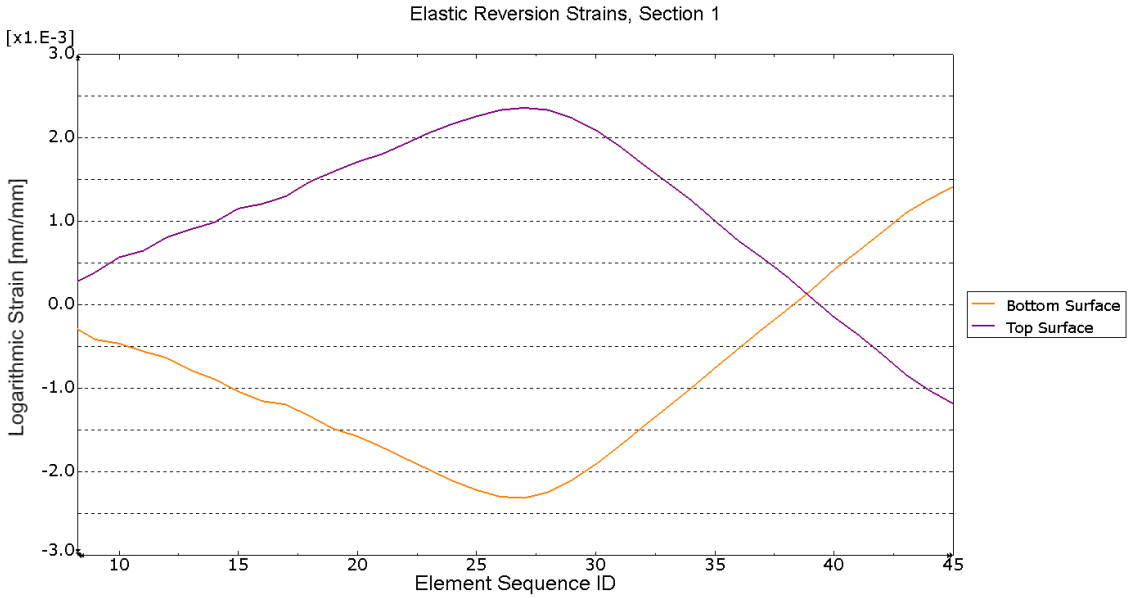

Figure 4-15 Elastic strain reversion in the circumferential direction.

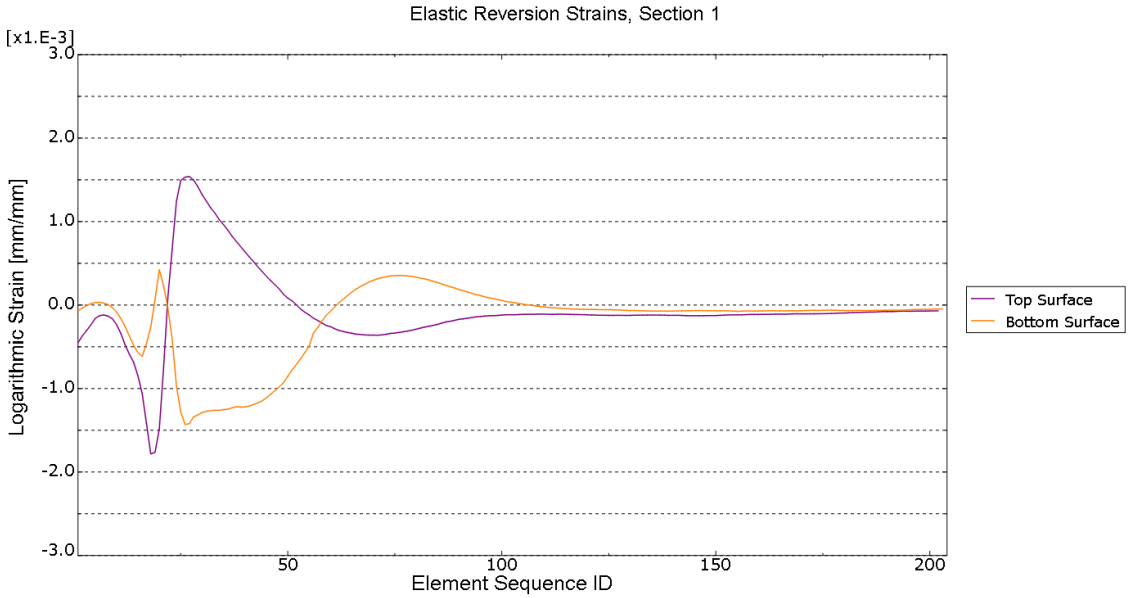

Figure 4-16 Elastic strain reversion in the longitudinal direction.

4.2.1 Stress States and Plastic Strains in the Circumferential Direction

The stress states before and after the springback in the circumferential direction are presented in Figure 4-17. It can be observed that the stresses in both top and bottom surface at the beginning of the path revert from compressive to tensile and vice versa. When moving forward on the sequence path, great reductions (up to 500 MPa) can be observed in the final distributions.

When observing the plastic strains in Figure 4-18, it is notable that the distributions are close to the ones at the end of the forming stage in Figure 4-9 and Figure 4-10. Even though the elastic strain is small compared to the total strains accumulated during the forming, it clearly plays an important role in the final residual stress distributions.

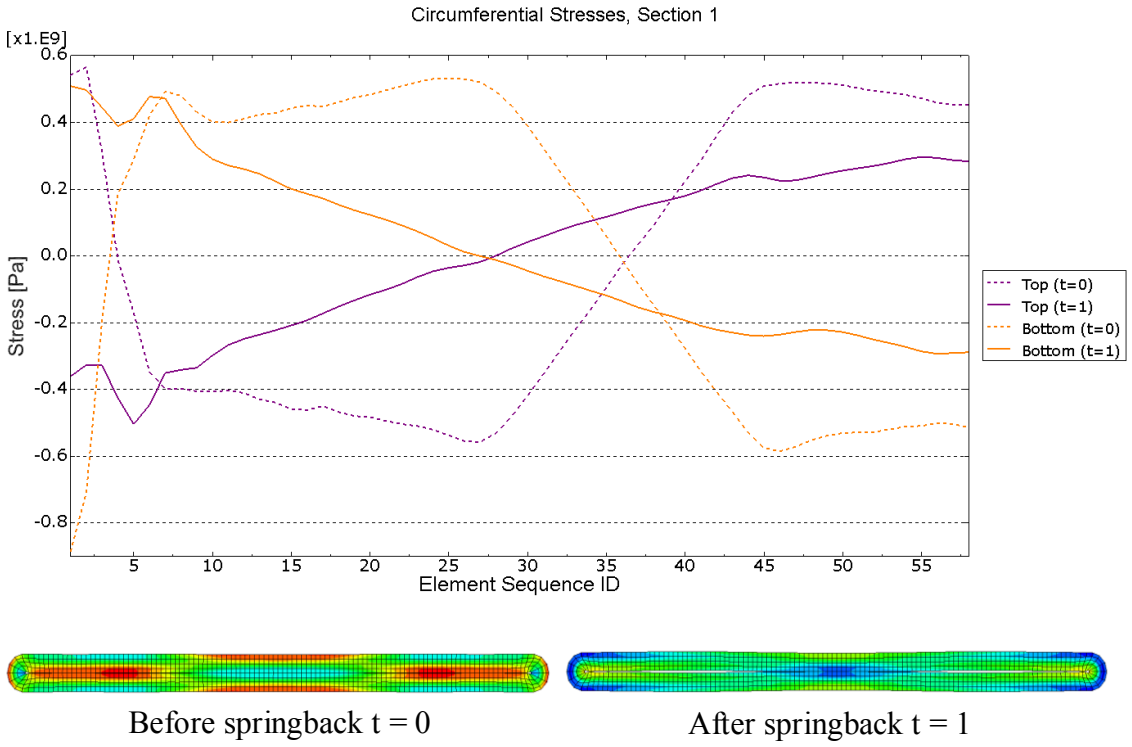

Figure 4-17 Stresses in the circumferential direction before and after the springback.

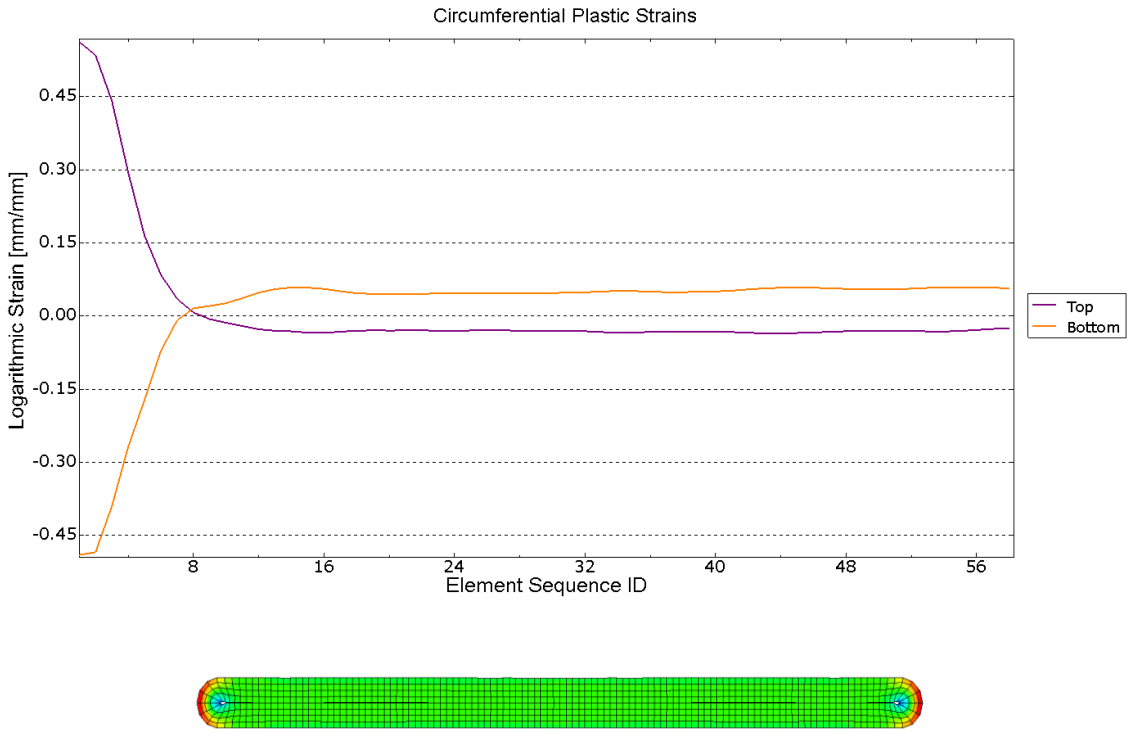

Figure 4-18 Plastic strains in the circumferential direction.

4.2.2 Stress States and Plastic Strains in the Longitudinal Direction

The stress states before and after the springback in the longitudinal direction are presented in Figure 4-19. The springback effect in the longitudinal direction can be seen most clearly in the root of the transition zone as the specimen bounces back towards the forming direction resulting in a small gap between the surfaces. Again, great reductions (up to 300 MPa) can be observed in the final distributions, although lower than in the circumferential direction. After the final set of plastic hinges is formed, the specimen remains fully tensile which is causing the improvement in the compressive bearing capacity.

The plastic strains are much lower in the longitudinal direction than in the circumferential direction as can be seen in Figure 4-20. The plastic strains are peaking at the plastic hinge line after dropping quickly, gradually lowering to zero. The transition zone has remained slightly at a stretched condition.

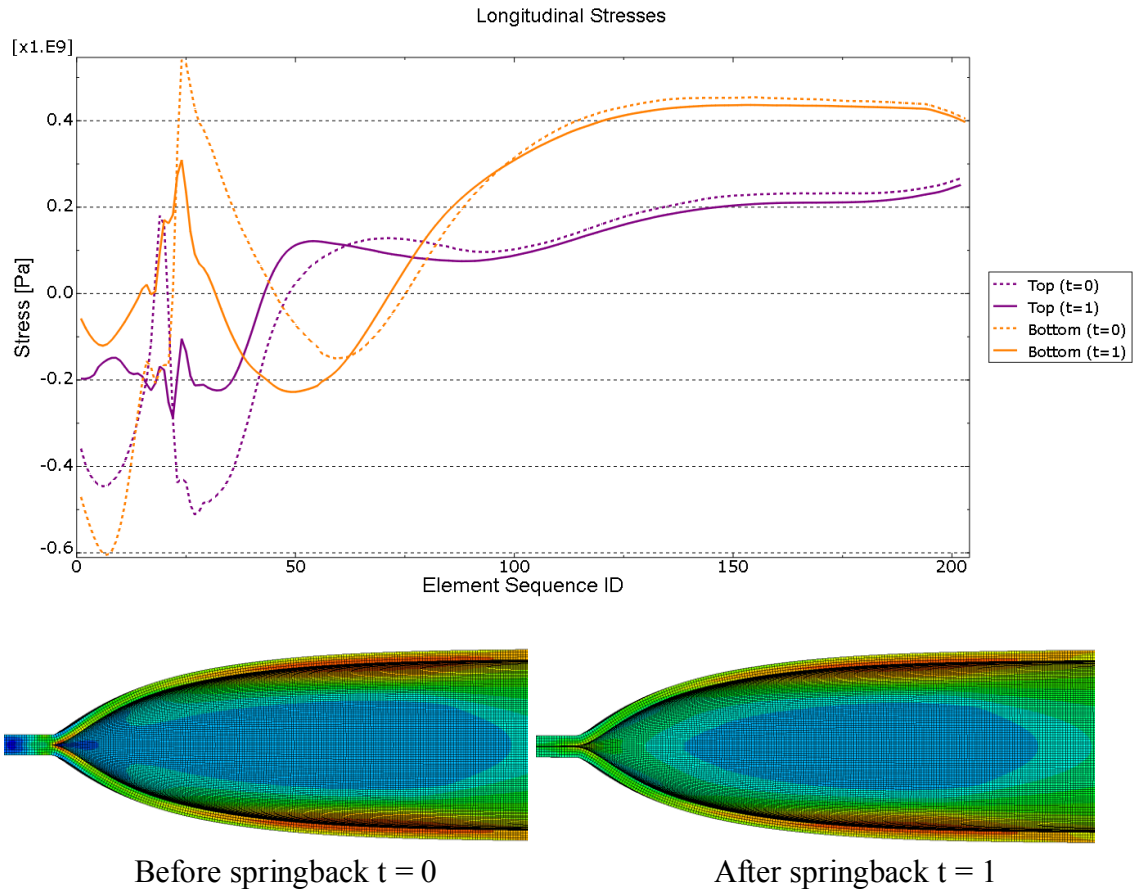

Figure 4-19 Stresses in the longitudinal direction before and after the springback.

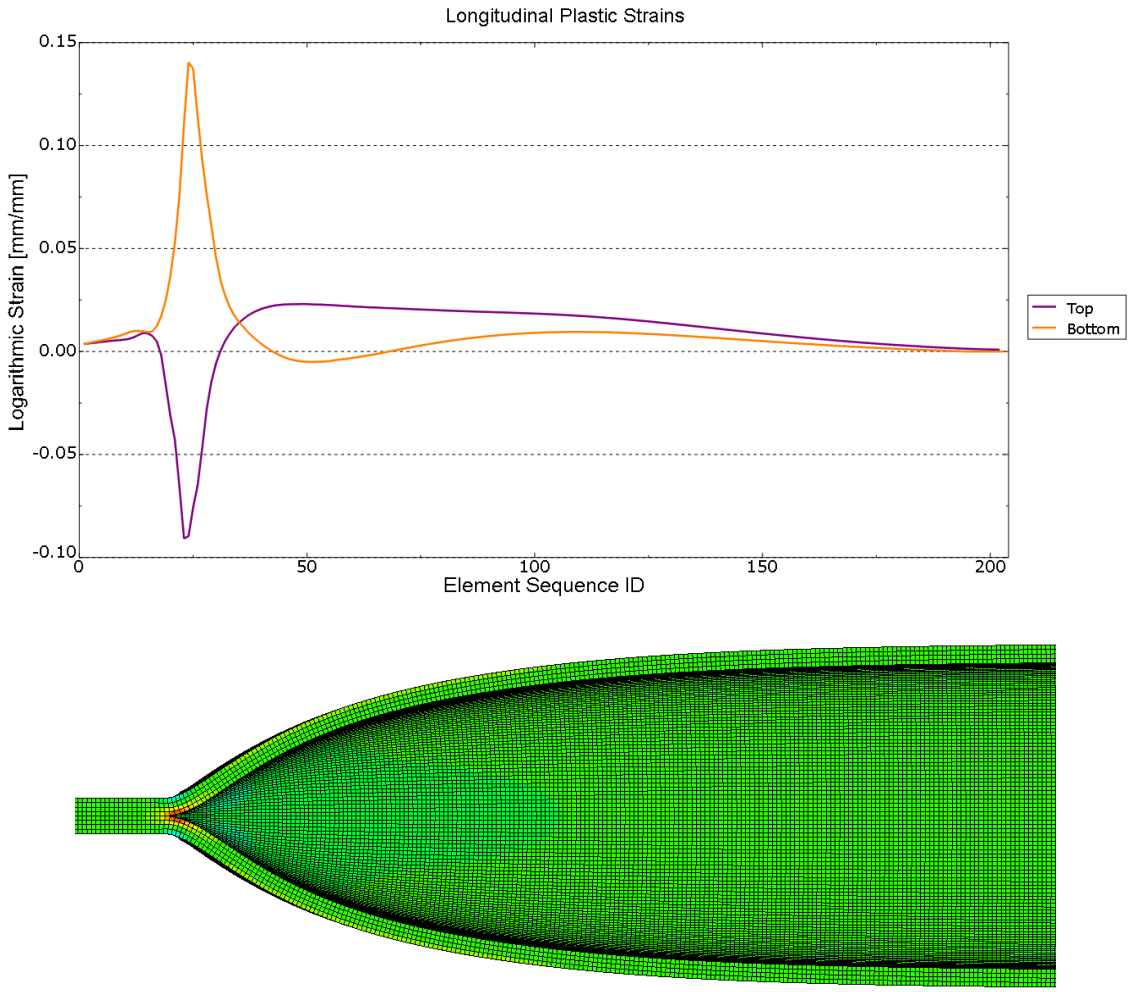

Figure 4-20 Plastic strains in the longitudinal direction.

5 Residual Stress Distributions and Their Effects on the Behavior of a Compressed Member

5.1 Circumferential Direction

The final residual stress distribution in the circumferential direction is presented in Figure 5-1 and the residual stress to yield strength ($f_y = 395{,}77\ MPa$) ratio in Figure 5-2. The compressive and tensile stresses are well in equilibrium even though only the elements on top and bottom surfaces were included when obtaining the elemental stress values. On the vertical axis where the first set of plastic hinges developed during the forming, the bottom surface is in compression; whereas the top surface is in tension. The absolute residual stress values on these areas are around $250\ MPa$. When moving towards the second set of plastic hinges on the horizontal axis, the tensile areas become compressed and vice versa. The reversion point indicates the location of the highest directional springback magnitude. The tensile stresses peak on the horizontal axis at the bottom surface around $500\ MPa$.

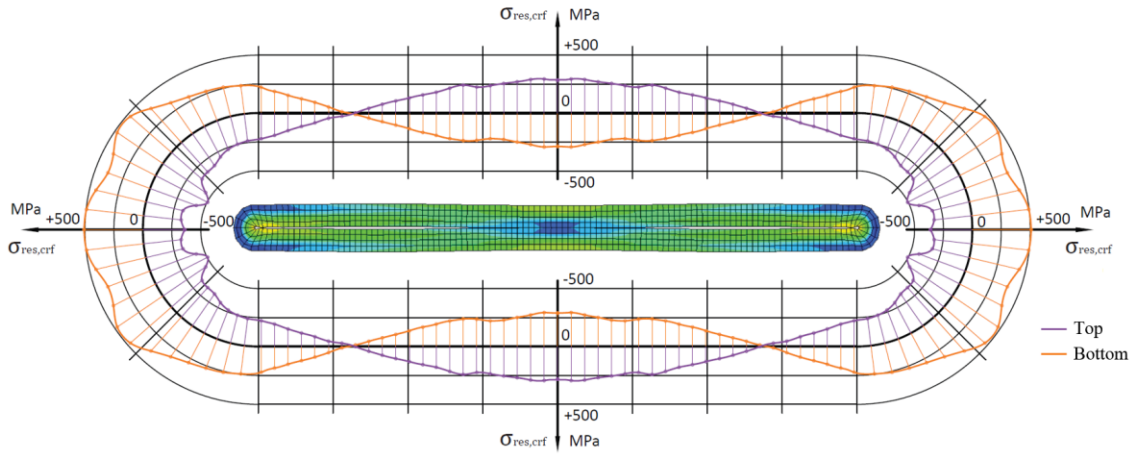

Figure 5-1 Residual stress distribution over the cross-section in circumferential direction.

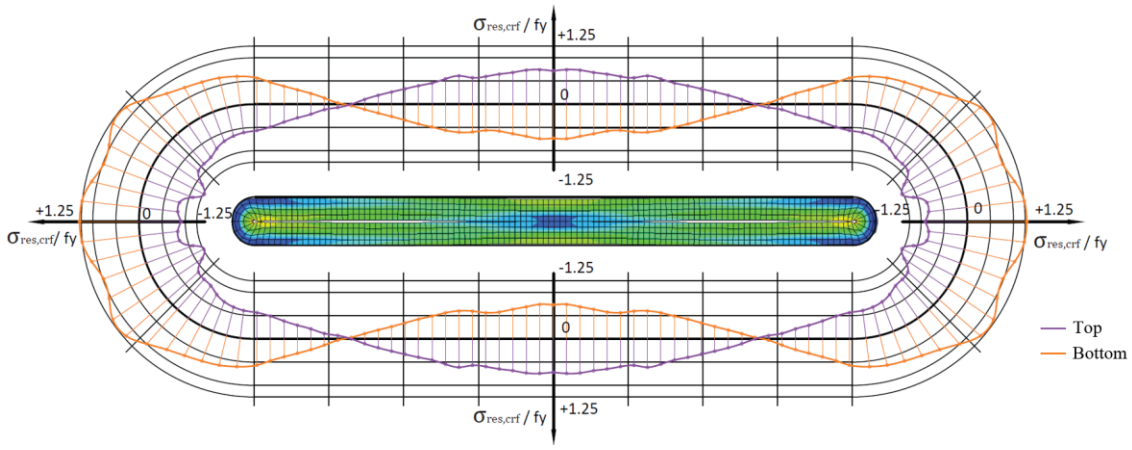

Figure 5-2 Residual stress to yield strength ratio in the circumferential direction.

5.2 Longitudinal Direction

The final residual stress distribution in the longitudinal direction is presented in Figure 5-3 and the residual stress to yield strength ratio in Figure 5-4. The distribution is a lot more complex than in the circumferential direction. However, some conclusions can be derived when observing the nature of the stresses. During the flattening, the tube specimen shortened at the circular end (due to the boundary conditions, the flattened end was constrained). The flattening stretched the transition zone generating high tensile stresses on vast areas. The tensile stresses may lead to strength enhancements. When the specimen was subjected to compressive loading, the tensile stresses are the main factor improving the compressive resistance.

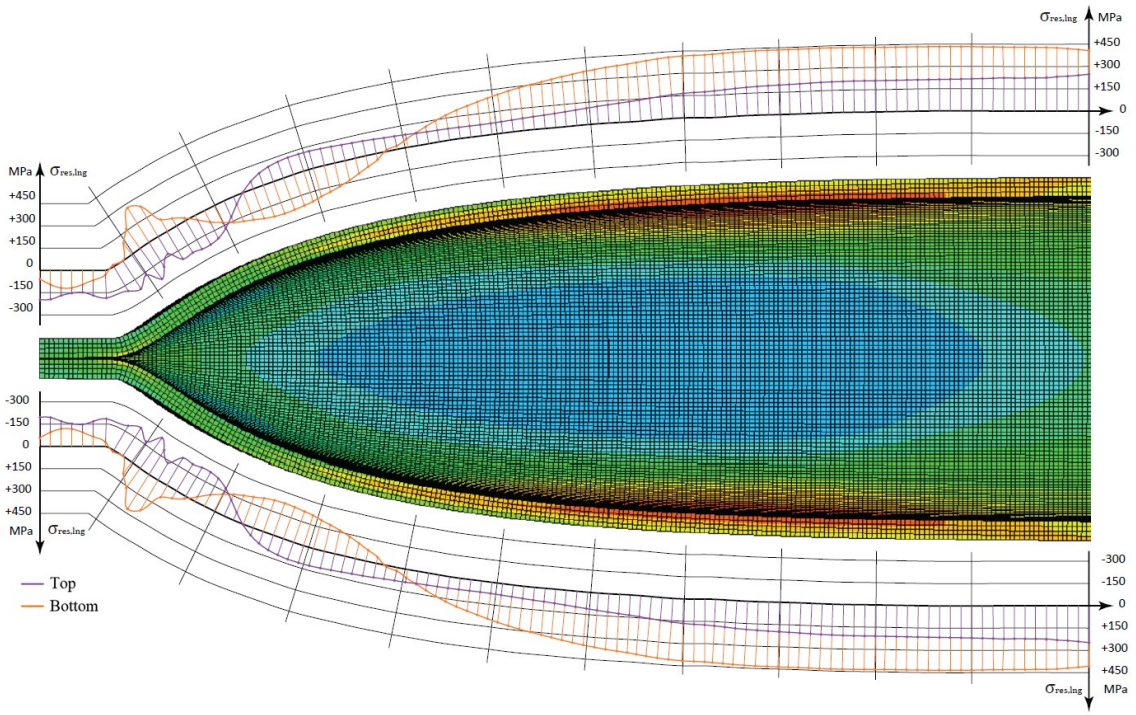

Figure 5-3 Residual stress distribution over the cross-section in the longitudinal direction.

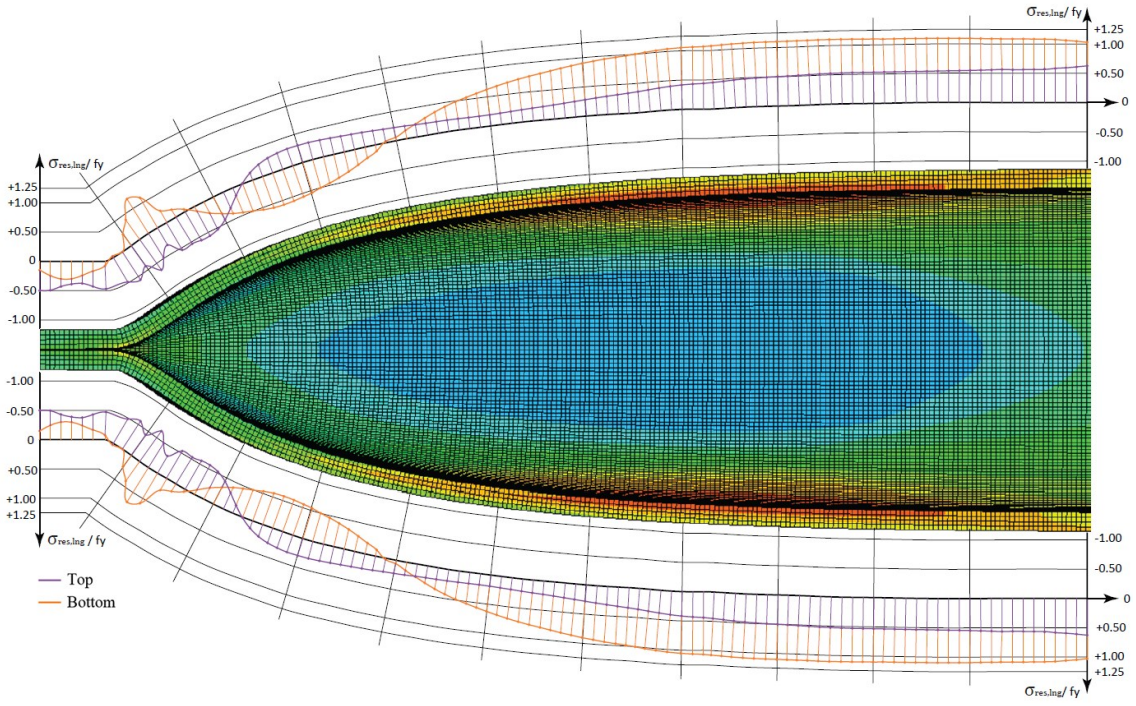

Figure 5-4 Residual stress to yield strength ratio in the longitudinal direction.

5.3 Further Evaluations on the Longitudinal Residual Stresses

As shown in Figure 5-3, there are high tensile stresses in the longitudinal direction within the transition zone. Additional cuts in the transverse direction are needed for understanding better the contributing effect of the longitudinal residual stresses. The residual stresses are observed in five sections as described in Figure 5-5.

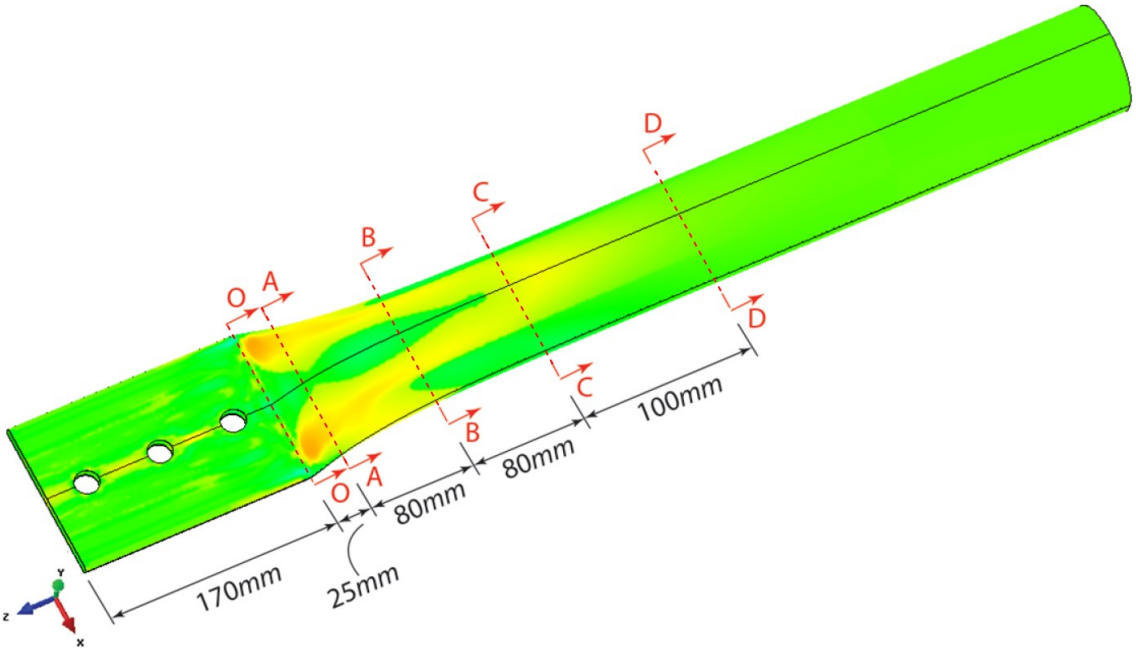

Figure 5-5 Additional sections for the longitudinal residual stresses.

5.3.1 Section O-O

The final residual stress distribution in the longitudinal direction at the section O-O is presented in Figure 5-6 and the residual stress to yield strength ratio in Figure 5-7. The scattered residual stress distribution promotes highly nonlinear behavior. The compressive and tensile stresses are fairly in equilibrium at the top surface whereas tensile stresses are dominant on the bottom surface; the highest absolute values being around 300 MPa. On the other hand, only the elements on top and bottom surfaces were included when obtaining the elemental stress values. The difference between the values at the top and at the bottom surfaces indicates that there is a bending state present in the cross section.

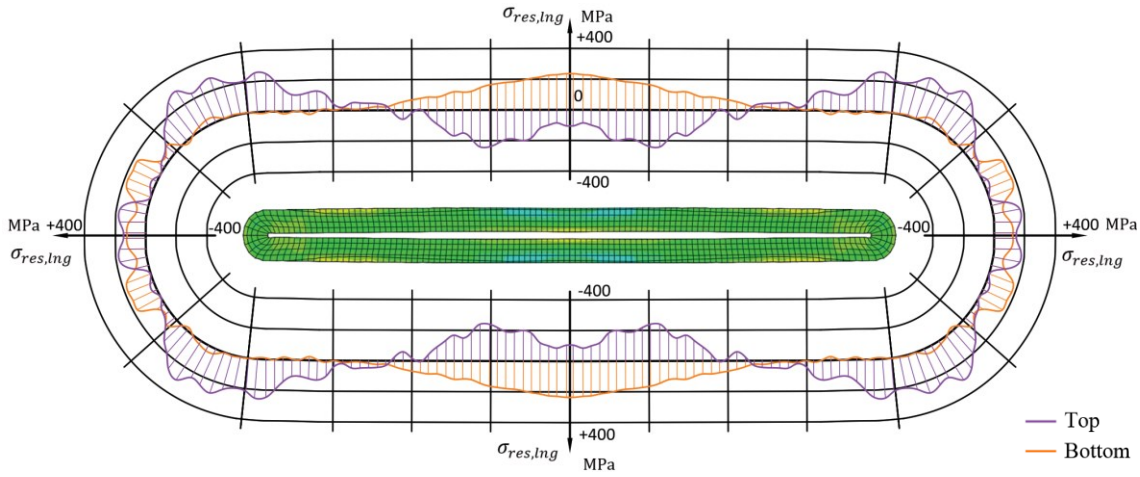

Figure 5-6 Longitudinal residual stresses at section O-O.

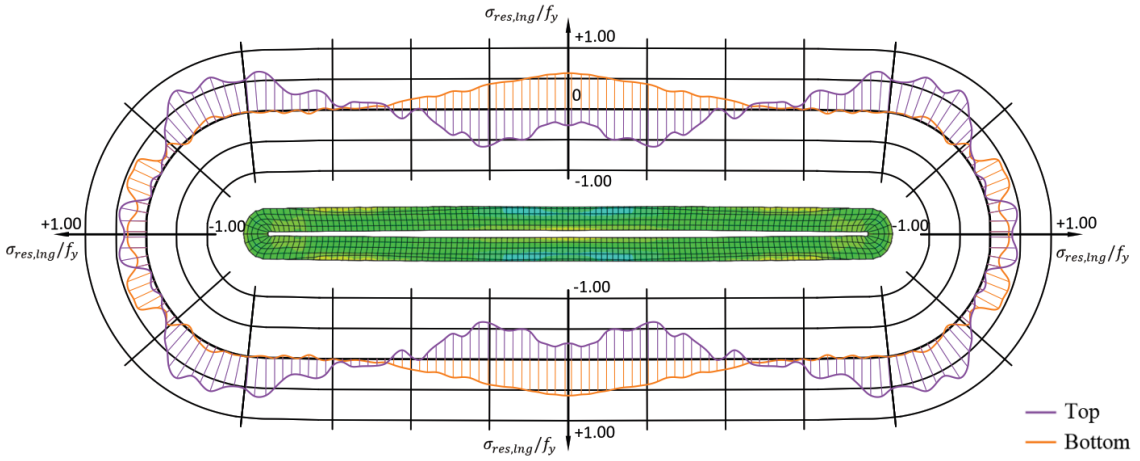

Figure 5-7 Residual stress to yield strength ratio at section O-O.

5.3.2 Section A-A

The final residual stress distribution in the longitudinal direction at the section A-A is presented in Figure 5-8 and the residual stress to yield strength ratio in Figure 5-9. The distribution is smoother compared to the section O-O. Again, the compressive and tensile stresses are fairly in equilibrium. When comparing the values at the top and at the bottom surface, it can be noted that the bending stresses are dominant within the section. The highest absolute stress values are around 410 MPa.

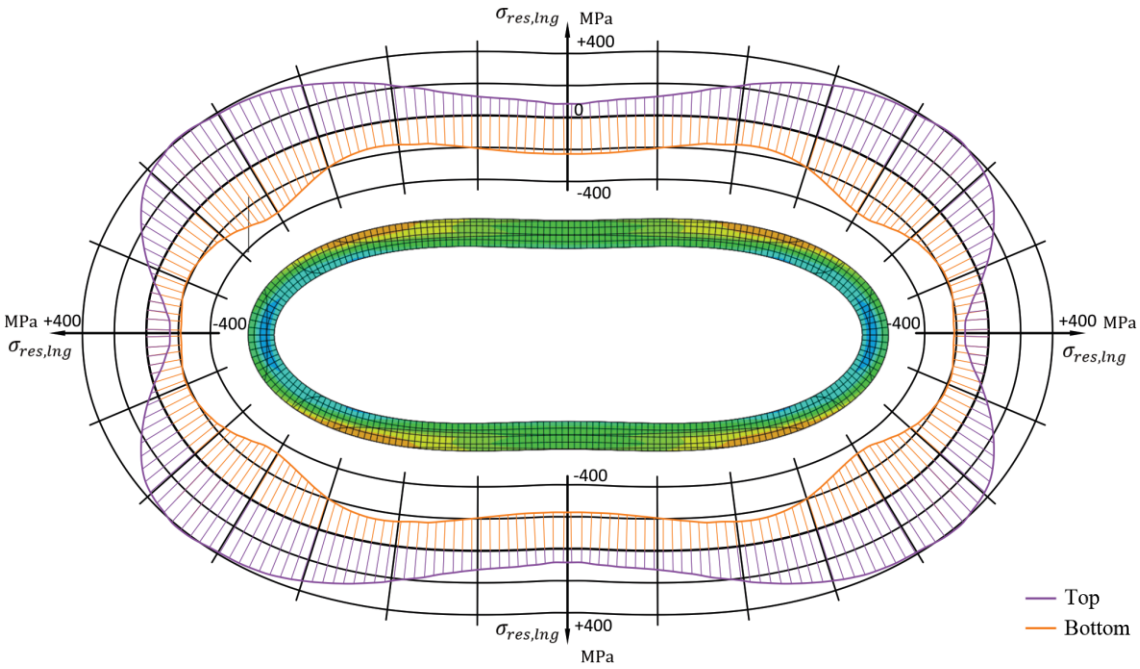

Figure 5-8 Longitudinal residual stresses at section A-A.

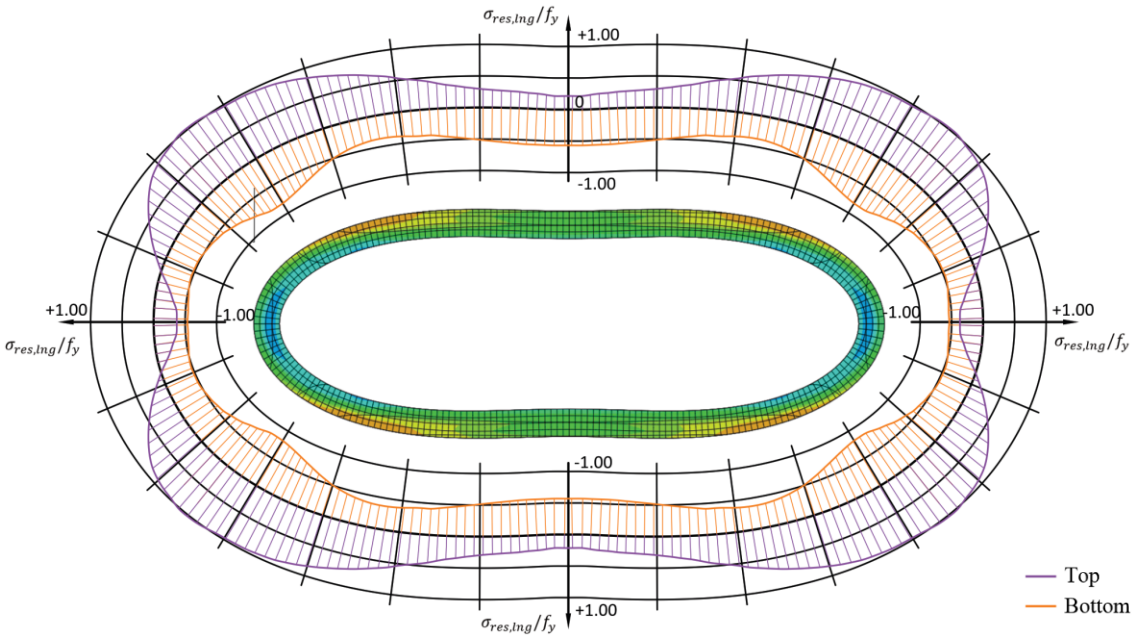

Figure 5-9 Residual stress to yield strength ratio at section A-A.

5.3.3 Section B-B

The final residual stress distribution in the longitudinal direction at the section B-B is presented in Figure 3-30 and the residual stress to yield strength ratio in Figure 3-31. A force equilibrium can be seen within the section. The compressive and tensile areas are

similar at the top and at the bottom surface, however there are some bending stresses present. The highest absolute stress values are around 430 MPa.

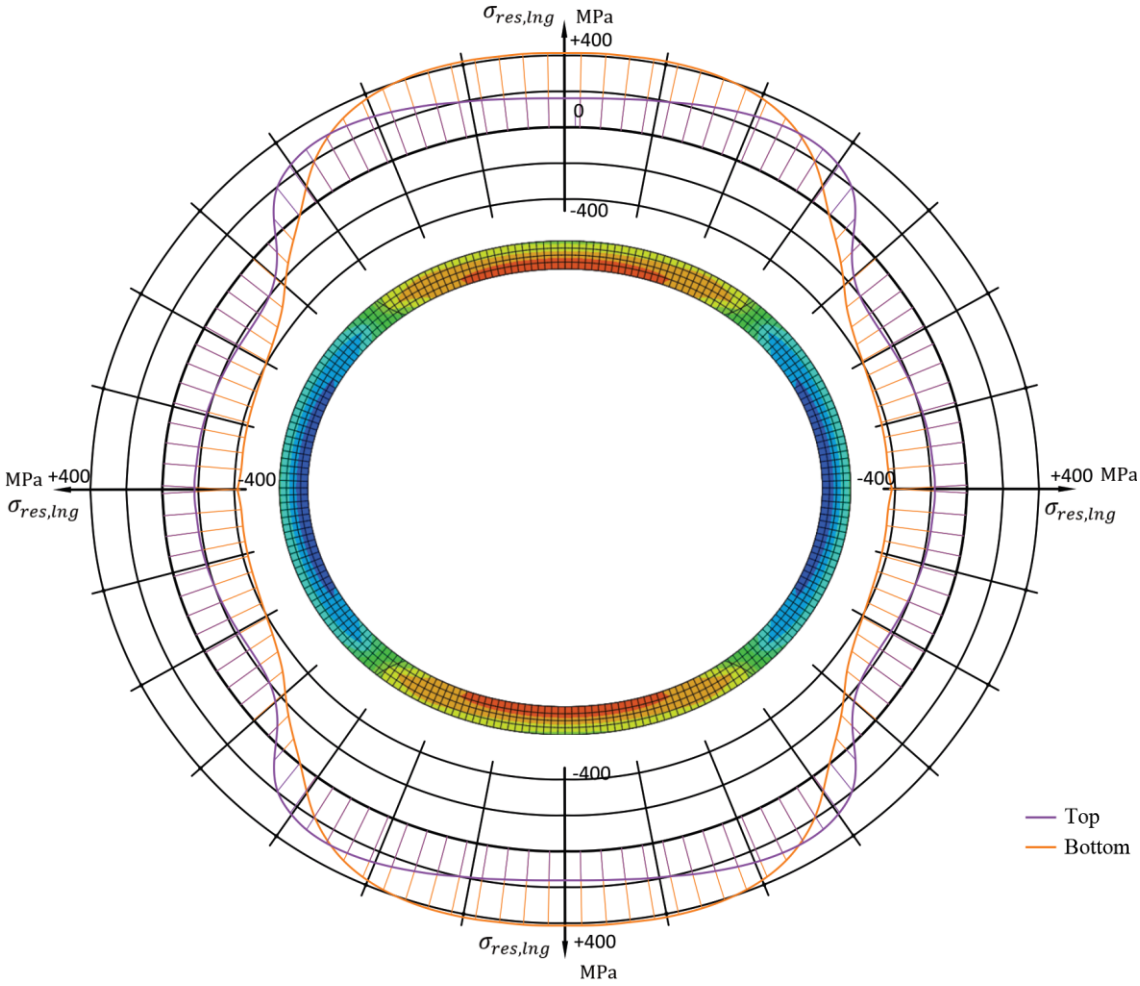

Figure 5-10 Longitudinal residual stresses at section B-B.

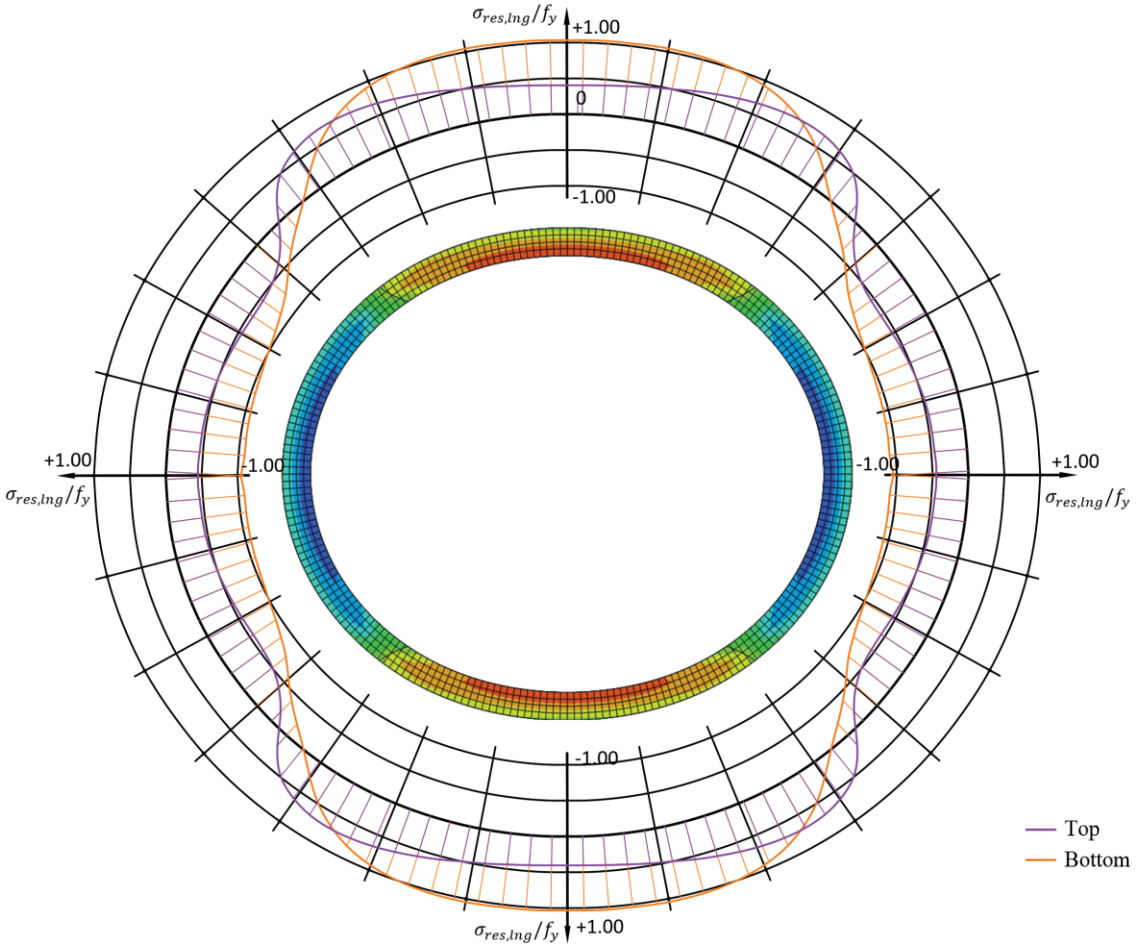

Figure 5-11 Residual stress to yield strength ratio at section B-B.

5.3.4 Section C-C

The final residual stress distribution in the longitudinal direction at the section C-C is presented in Figure 5-12 and the residual stress to yield strength ratio in Figure 5-13. A clear force equilibrium can be seen within the section. Again, the compressive and tensile areas are similar at the top and at the bottom surface with some bending stresses present. The highest absolute stress values are around 380 MPa.

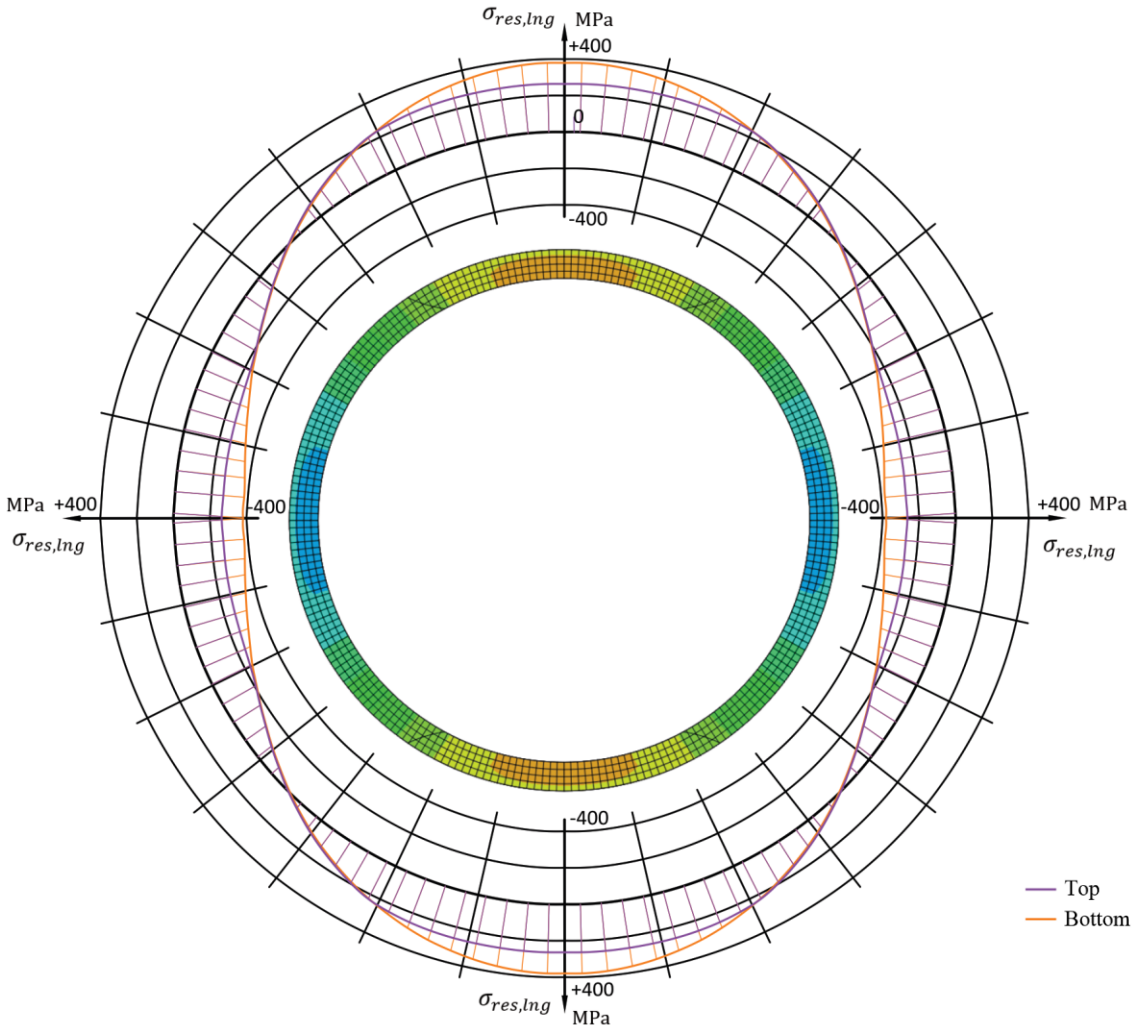

Figure 5-12 Longitudinal residual stresses at section C-C.

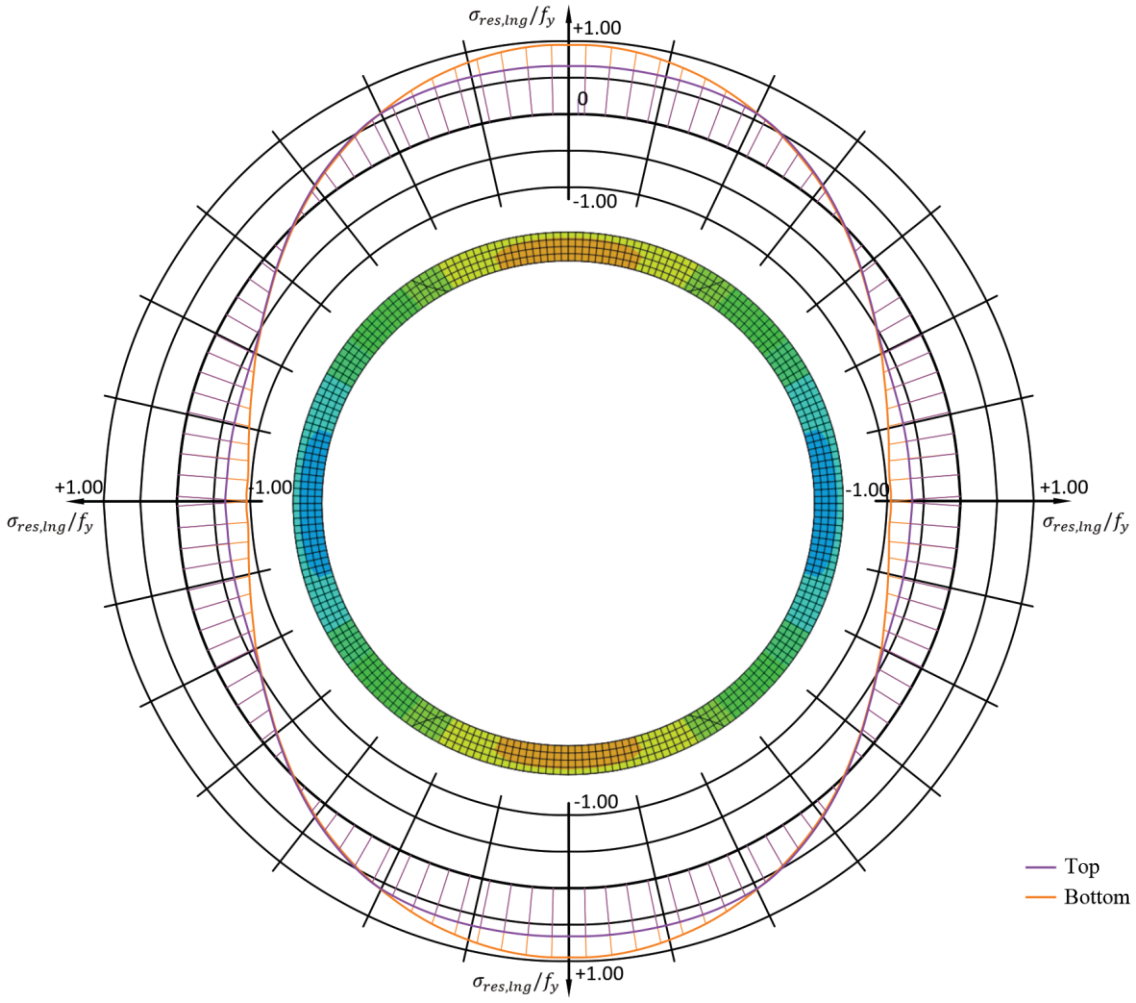

Figure 5-13 Residual stress to yield strength ratio at section C-C.

5.3.5 Section D-D

The final residual stress distribution in the longitudinal direction at the section D-D is presented in Figure 5-14 and the residual stress to yield strength ratio in Figure 5-15. The distribution is similar when compared to section C-C, however the residual bending stresses are affecting in the opposite direction. A significant reduction can be seen in the residual stress values; the highest absolute stress values only being around 120 MPa.

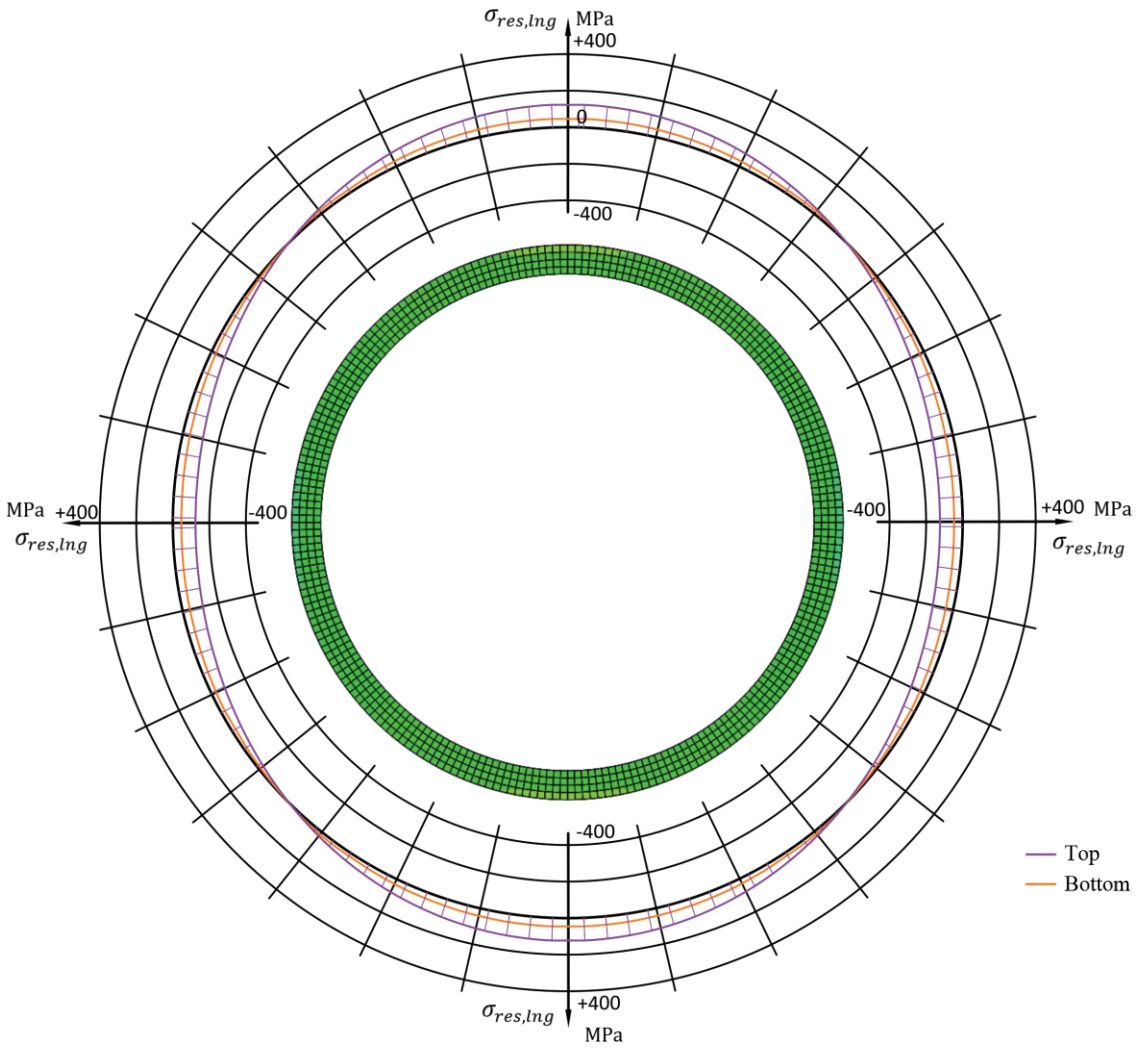

Figure 5-14 Longitudinal residual stresses at section D-D.

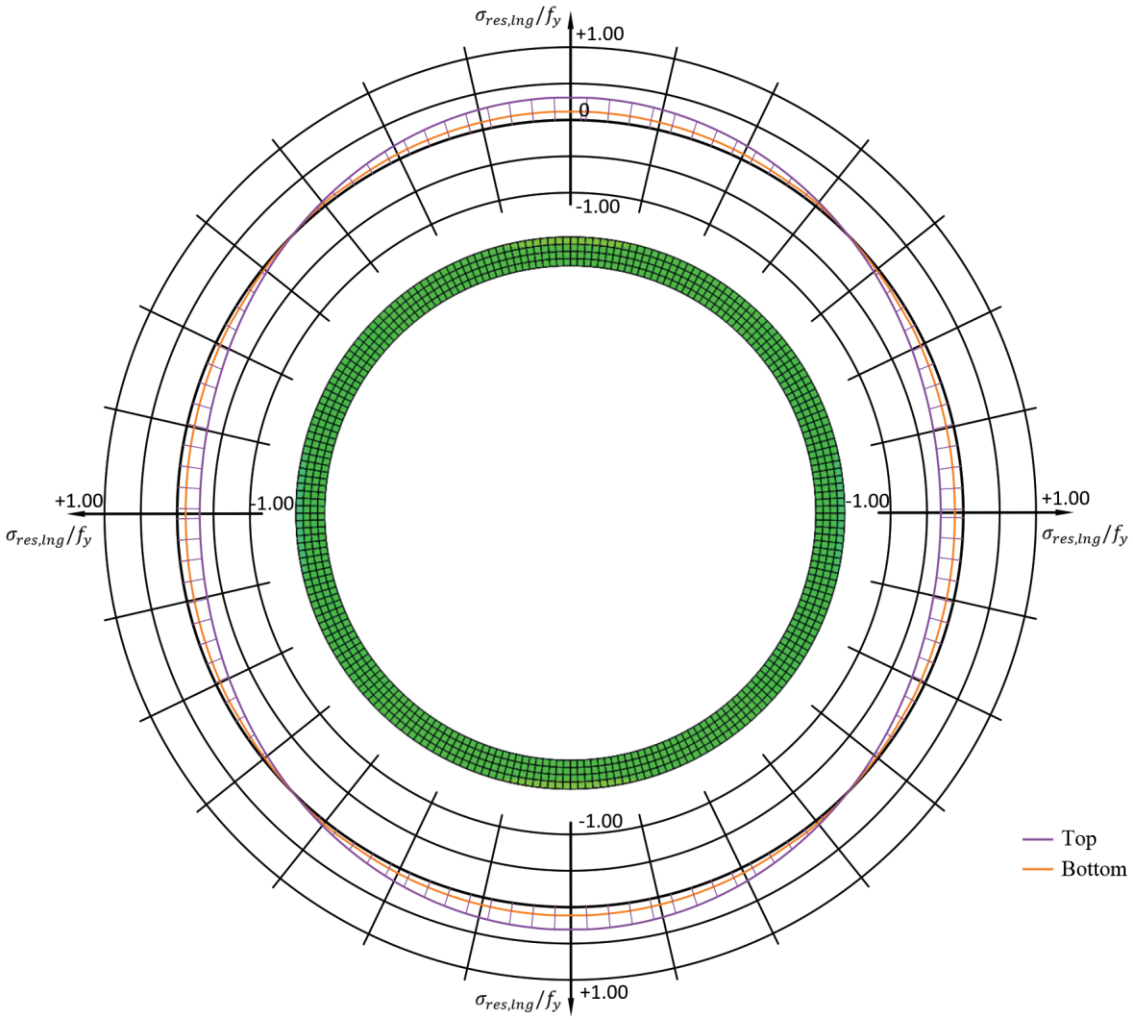

Figure 5-15 Residual stress to yield strength ratio at section D-D.

5.4 Effects on the Behavior of a Compressed Member

The following subchapter evaluated the influence of the residual stresses on the behavior of a compressed member. This is done by taking the load displacement curve shown in Figure 3-54 and evaluating the stress state at the points selected from the curve. The load displacement curve and the points are represented in Figure 5-16. The longitudinal stresses at the points are presented in Figures from 5-17 to 5-20.

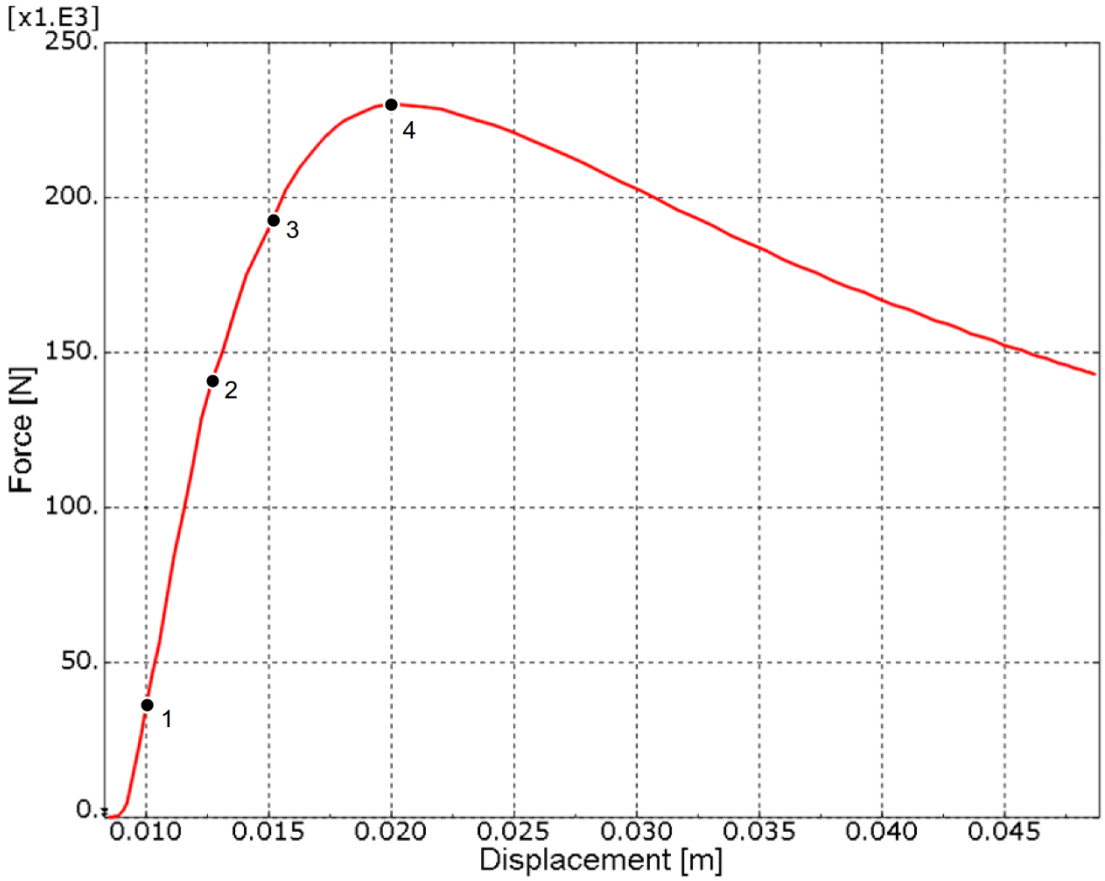

Figure 5-16 The load displacement curve with selected points.

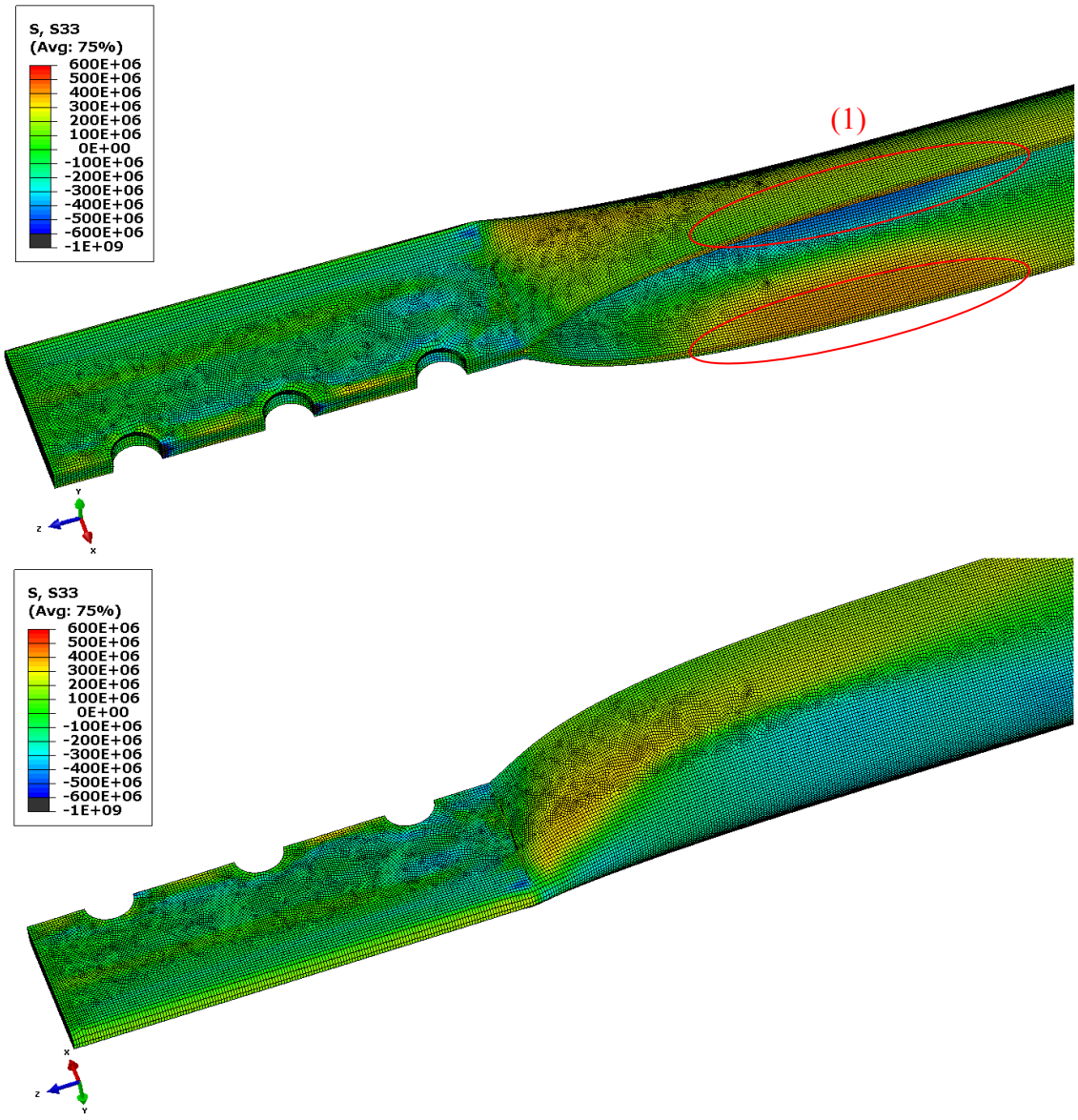

Figure 5-17 Longitudinal stress state at the point one in Figure 5-16.

It can be seen from Figure 5-17 (and also from section B-B, Figure 5-10) that the cross section is overall in tension inside the transition zone (1). There are also some bending stresses resulting from the non-uniform stress distribution over the tube wall thickness.

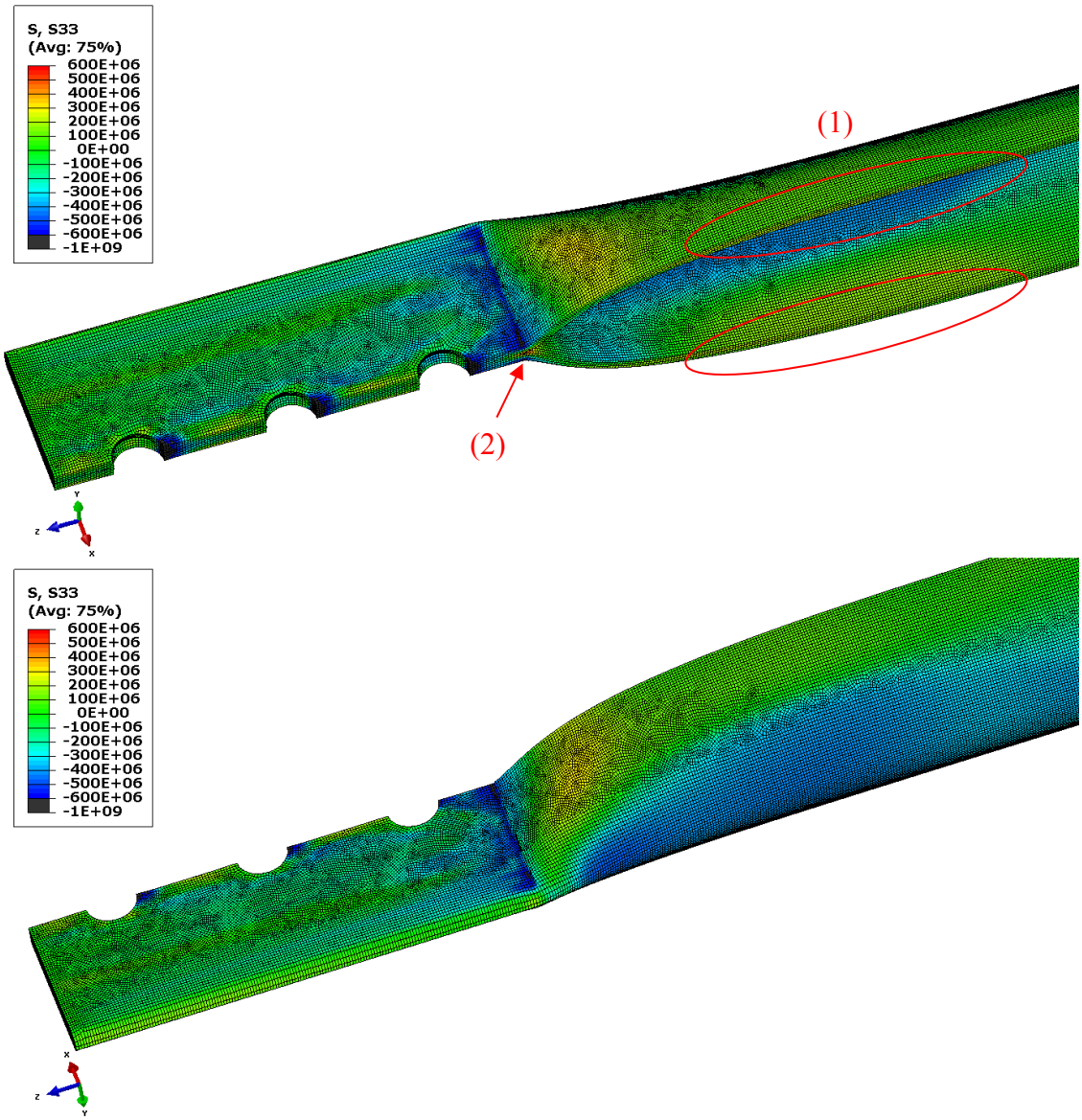

Figure 5-18 Longitudinal stresses at the point two in Figure 5-16.

When the compressive loading increases, the tensile areas begin to diminish as can be observed from Figure 5-18 (1). A fully developed set of plastic hinges can be seen at the root of the transition zone (2).

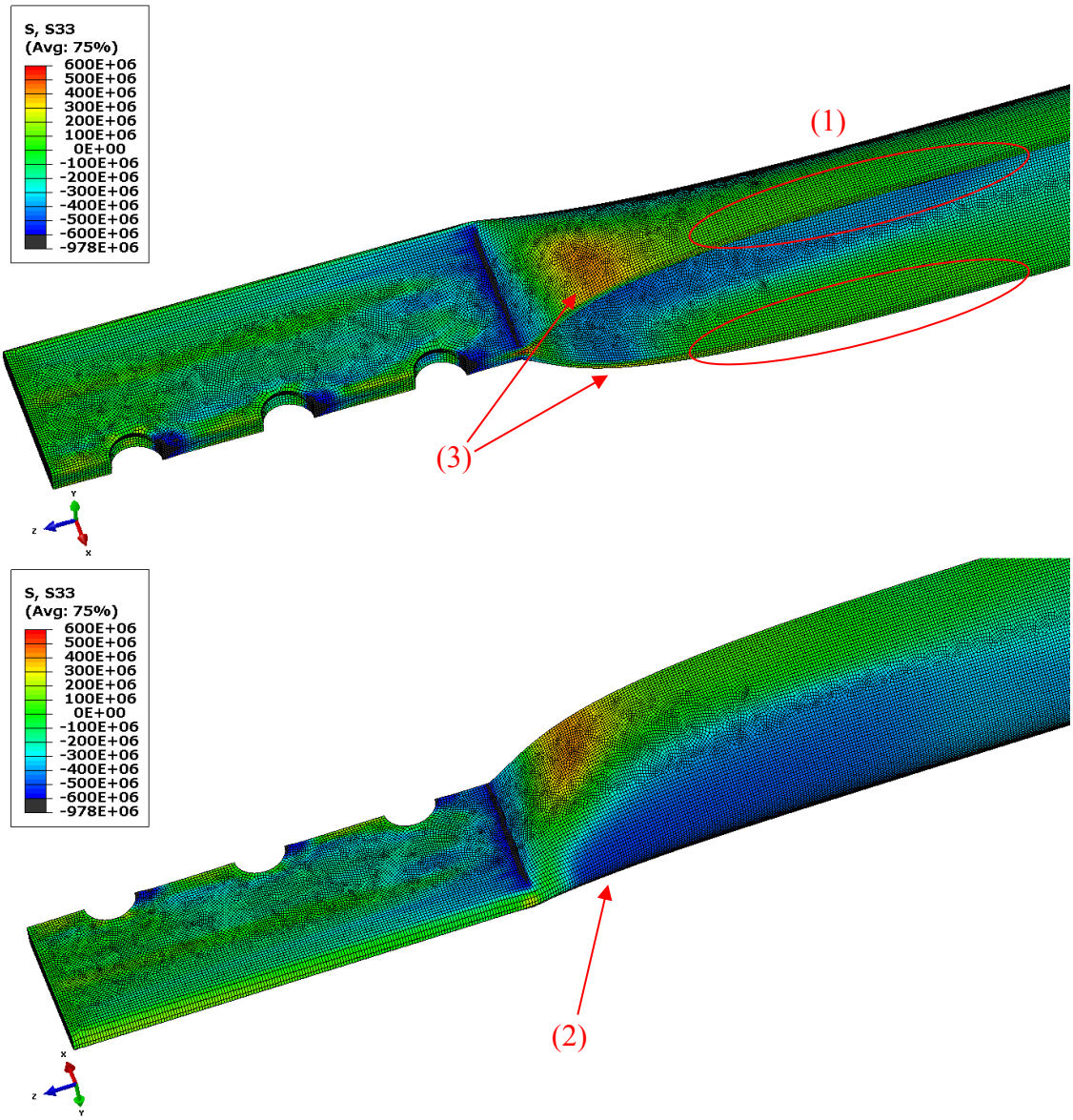

Figure 5-19 Longitudinal stresses at the point three in Figure 5-16.

At data point three the tensile areas on the transition zone have become fully compressed as can be observed from Figure 5-19 (1). The stiffer corner areas attract the compressive loading (2) balanced by the bolts. As the flattened portion moves towards the circular area, a fully plasticized region begins to form (3). It can noticed that the plasticized region forms due to the local bending as the top surface is in tension and the bottom surface is in compression.

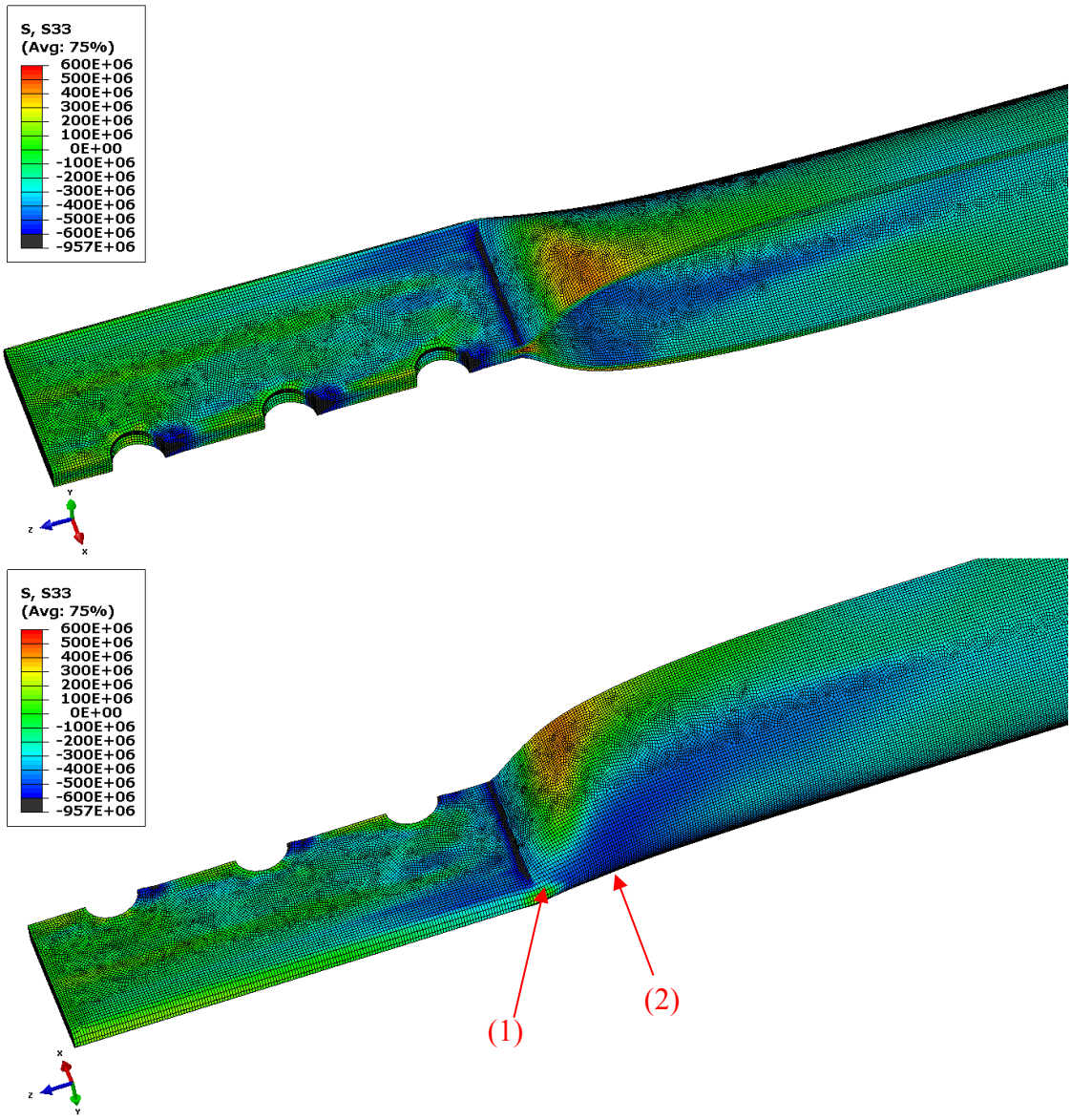

Figure 5-20 Longitudinal stresses at the point four in Figure 5-16.

It can be observed from Figure 5-20 (1) that after the first plasticized region has formed, an alternative load path structure is formed and the structure can still carry some extra loading. However, after this point more plasticized regions begins to form (2) and the structure loses its bearing capacity.

6 Conclusions

Advanced analysis techniques based on non-conservative approaches can be adopted to design steel structures that are not covered by any design code. In such analyses, the initial material stress state and the deformed geometry are modelled accurately for a realistic structural response under a certain set of events. In theory, any kind of manufacturing method can be reliably simulated with correct analysis parameters. In practice, this requires knowledge of nonlinear continuum mechanics, finite element discretization and metal forming simulations. A verification of the modeling by experimental results is necessary before case-specific analyses.

The numerical simulation conducted in this thesis provided an example of determination of structural capacity using advanced analysis techniques. Existing guidelines for finite element modelling and energy level monitoring provided a good starting point for a suitable search of parameters to be used in analyses. The results showed a good correlation with the experimental data. The performance of the explicit time integration algorithm combined with reduced integration elements was robust and the calculation times were reasonable (less than 15 hours per model) regardless of the large number of elements. However, there are still factors affecting the analysis results.

The selected Ramberg-Osgood material model with isotropic hardening provided a good estimation for evaluating the plastic behavior of the structure. However, due to the sensitive nature of metal forming processes, the stress-strain curve based on an actual tensile test would have improved the accuracy. A comparison study with kinematic hardening law is recommended since cyclic plasticity was observed during the forming. The material model also assumed strains to be able to increase unlimited, though the work hardening stops at 100 %. With a proper material damage model, the crack formation could have been monitored.

Since the fracture mechanical aspects were ignored, bolt holes had to be modelled prior to the flattening, which may give inaccurate results for residual stresses around the bolt holes. Instead of high stress peaks, the hole drilling would have relieved the residual stresses. In addition, the holes may have affected the plastic mechanism as the first set of plastic hinges appeared on the bolt line.

The absolute values of residual stresses in the circumferential direction peaked at $500\ MPa$, which is roughly 1.25 fold to the material yield strength. The peak values were located in the corner areas of the flattened region. The residual stress values hardly exceeded the material yield strength in the longitudinal direction and the distribution was more uniform within the section. A clear contribution of the tensile residual stresses in the longitudinal direction was seen when the behavior of the member was evaluated under compressive loading.

In compression, the structural capacity was found to be very close to the experimental data when residual stresses were included in the model. The residual stresses improved the capacity by 5.79 % due to the high tensile residual stress values in the longitudinal direction. The high longitudinal stresses can be explained by the stretching of the transition zone during the flattening process. The structural response was stiffer when compared to the experimental data. There are several possible reasons like behavior of the bolts, the axial shortening and imperfections causing this type of nonlinear response as discussed earlier. Neither have residual stresses significant effect on the axial stiffness nor the post buckling behavior. The final residual stress patterns can be considered as a good estimation of the initial material state and help to understand the local plastic behavior of the member with flattened ends. However, when performing a dynamic analysis, the stiffened response has a significant impact on the eigenvalues and the natural frequencies.

Before the flattening, the tube specimen was assumed completely stress free and prismatic, though there are some residual stresses and geometrical imperfections resulting from the cold forming of the tube. However, the failure mode of the selected tube size was an excessive deformation of the transition zone and therefore the initial state resulting from the cold forming of the tube does not play an important role. In case of overall flexural buckling, the cold forming may significantly affect results.

The Arbitrary Lagrangian-Eulerian discretization method was excluded from the analysis parameter studies due to the significant increase in calculation times. The method could have improved the numerical performance leading to even more accurate structural response. The stress peaks could also appear on smaller areas.

From an engineering point of view, in order to find the most suitable tube sizes for flattening, the best-performing materials and the optimal hole drilling locations on the flattened region; extensive parametric studies are required. However, the importance of experimental results for validating numerical simulations is always useful to recognize.

References

[1] Dutta, D.,Wardenier, J.,Yeomans, N.,Sakae, K.,Bucak, Ö.,Packer, J.A. *Design Guide For Fabrication, Assembly and Erection of Hollow Section Structures*. Köln: TÜV-Verlag. 1998.

[2] Schafer BW, Peköz T. *Computational modeling of cold-formed steel: characterizing geometric imperfections and residual stresses*. Journal of Constructional Steel Research, vol. 47, pp. 193-210. 1998.

[3] Withers, P.J., Bhadeshia, H.K.D.H. *Residual Stress : Part 2 - Nature and Origins*. Materials Science and Technology, vol. 17, pp-366-375. 2001.

[4] Hosford W. *Mechanical Behavior of Materials*. Cambridge: Cambridge University Press. 2005.

[5] Totten,G., Howes, M., Inoue, T. *Handbook of Residual Stress and Deformation of Steel*. Materials Park, OH: ASM International. 2002.

[6] Yu,W., LaBoube,R. *Cold-Formed Steel Design*. Hoboken, N.J: John Wiley & Sons. 2010.

[7] *SFS-EN 1993-1-1 Eurocode 3 : Design of Steel Structures. Part 1-1: General Rules and Rules for Buildings*. Helsinki: Suomen standardisoimisliitto SFS ry. 2005.

[8] *SFS-EN 1993-1-8 Eurocode 3 : Design of Steel Structures. Part 1-8 : Design of Joints*. Helsinki: Suomen standardisoimisliitto SFS ry. 2005.

[9] *SFS-EN 1993-1-5 Eurocode 3 : Design of Steel Structures. Part 1-5: Plated Structural Elements*. Helsinki: Suomen standardisoimisliitto SFS ry. 2006.

[10] El-Sheikh A. *Development of a New Space Truss System*. Journal of Constructional Steel Research, vol. 37, pp. 205-227. 1996.

[11] Mistakidis, E.S.,Tsiogas, S.V. *Failure Modes of Circular Hollow Members with Flattened Edges*. Journal of Constructional Steel Research, vol. 59, pp. 1573-1592. 2003.

[12] De Andrade, S.A.L., Vellasco, P.C.G.d.S., De Silva, J.G.S., De Lima, L.R.O., D'Este, A.V. *Tubular Space Trusses with Simple and Reinforced End-flattened Nodes : An Overview and Experiments*. Journal of Constructional Steel Research, vol. 61, pp. 1025-1050. 2005.

[13] Dundu M. *Effect of Flattening Circular Hollow Sections in Truss and Dome Structures*. Thin-Walled Structures, vol. 80, pp. 57-65. 2014.

[14] Klocke F. *Manufacturing Processes 4 : Forming*. Berlin: Springer. 2013.

[15] Abaqus Documentation. [Online]. Available: http://50.16.225.63/v6.14/.

[16] Nie, D.F., Chen, X.D., Fan,Z.C., Wu, Q.G. *ALE-Based Finite Element Simulation of Large Deformation in Bending and Flattening Tests*. Procedia Engineering, vol. 130, pp. 775-783. 2015.

[17] *Metal Forming with Abaqus : Training Course Lecture Notes*. [Online]. Available: https://academy.3ds.com/en/learn/metal-forming-abaqus.

[18] Wriggers P. *Nonlinear Finite Element Methods*. Berlin: Springer. 2008.

[19] Cook,R.D., Malkus, D.S., Plesha, M.E. *Concepts and Applications of Finite Element Analysis*. New York: John Wiley & Sons. 1989.

[20] Det Norske Veritas AS. *Recommended Practice DNV-RP-C208 : Determination of Structural Capacity by Non-linear FE analysis Methods*. Det Norske Veritas AS. 2013.

[21] Kojic, K., Bathe, K-J. *Inelastic Analysis of Solids and Structures*. Berlin: Springer. 2005.

[22] Marciniak,Z., Duncan,J.L., Hu, S.J. *Mechanics of Sheet Metal Forming*. Oxford: Butterworth-Heinemann. 2002.

[23] Davis JR. *Tensile Testing*. Materials Park, Ohio: ASM International. 2004.

[24] Bathe K. *Finite Element Procedures*. Englewood Cliffs (NJ): Prentice Hall. 1996.

[25] *LS-DYNA Support : Time Integration Tutorial*. [Online]. Available: http://www.dynasupport.com/tutorial/ls-dyna-users-guide/time-integration.

[26] Lee, H-H. *Finite Element Simulations with ANSYS Workbench 16*. Mission (KS): SDC Publications. 2015.

[27] Qi, Y., Zhao, F., Zhou, J. *Applications of Explicit FEA in Structural Static and Dynamic Analyses*. Applied Mechanics and Materials, vol. 438-439, pp. 1498-1501. 2013.

[28] Bursi, O.S., Jaspart, J.P. *Basic Issues in the Finite Element Simulation of Extended End Plate Connections*. Computers and Structures, vol. 69, pp. 361-382. 1998.